

Influence of Strain Hardening on the Water Droplet Erosion Performance of 17-4 PH Stainless Steel

Rizwan Ahmed Shaik

A Thesis
in
the Department of
Mechanical, Industrial and Aerospace Engineering

Presented in Partial Fulfilment of Requirements
for the Degree of the Master of Applied Science (Mechanical Engineering) at
Concordia University
Montreal, Quebec, Canada

April 2021

© Rizwan Ahmed Shaik, 2021

CONCORDIA UNIVERSITY
School of Graduate Studies

This is to certify that the thesis is prepared

By: Rizwan Ahmed Shaik

Entitled: Influence of Strain Hardening on the Water Droplet Erosion Performance
of 17-4 PH Stainless Steel

and submitted in partial fulfilment of the requirements for the degree of
Master of Applied Science (Mechanical Engineering)

Complies with the regulations of the University and meets the accepted standards with respect to originality and quality.

Signed by the final Examining Committee:

Chair

Dr. Mojtaba Kheiri

Examiner

Dr. Ali Dolatabadi

Examiner

Dr. Mojtaba Kheiri

Supervisor

Dr. Mamoun Medraj

Supervisor

Dr. Martin Pugh

Approved by _____ *Graduate Program Director*
Dr. Sivakumar Narayanswamy

Date

Dr. Mourad Debbabi
Dean, Gina Cody School of Engineering and Computer Science

Abstract

Influence of Strain Hardening on the Water Droplet Erosion Performance of 17-4 PH Stainless Steel

Rizwan Ahmed Shaik

Water Droplet Erosion (WDE) is a wear erosion phenomenon that is predominantly observed in gas, steam and wind turbines due to repetitive droplet impacts. In this work, various damage mechanisms pertaining to this phenomenon, described in the literature, are reviewed in detail. It was found that various surface treatments have been applied to delay the start of erosion in the material. However, in doing so the role of strain hardening was not well understood.

In this work, a suitable material is identified to study the effect of strain hardening on the WDE performance. The material was characterized for various mechanical properties and for water droplet erosion. The material was also tested for WDE by performing a Deep Rolling (DR) treatment before testing. The erosion incubation time is analyzed by considering the yield strength, elastic resilience and strain hardening exponent. It was found that the erosion incubation time is dependent on the yield strength, elastic resilience and strain hardening exponent of the material.

The role of strain hardening on WDE performance was also studied by intermittent strain relieving of the samples exposed to WDE. The frequency of strain relieving was found to influence the erosion behavior. It was observed that frequent strain relieving during WDE influences the erosion incubation time and the maximum erosion rate.

Acknowledgements

I would like to express my sincere gratitude to Professor Mamoun Medraj and Professor Martin Pugh for giving me this opportunity to work on this research. I am very thankful for their supervision and valuable guidance throughout my M.A.Sc program. Their intellectual and financial support in carrying out this research is much appreciated. I wish to express my thanks to Dr. Abdullahi K. Gujba for his valuable advice and moral support in accomplishing this research.

The logistical and technical support provided by Mazen Samara and Robert Oliver is acknowledged and highly appreciated. Their willingness to always help has been a blessing.

I would like to thank my colleagues at the Thermodynamics of Materials Group (TMG), Concordia University, who have been a constant source of encouragement to me and for their help and suggestions. It would not have been possible without your support Elhadi Ibrahim, Ming Jing, Eslam Fayed, Fatile Babajide Oluwagbenga, Mostafa Elyoussef and Xinzha Mu. I would also like to thank my friends who have supported me during my Masters.

The help received from Alain Belso in proofreading this thesis is commendable.

Special thanks to my parents, grandparents and little sister for their unconditional love, motivation and patience. Their prayers and words of encouragement have kept me going through thick and thin. This achievement would not have been possible without them.

Table of Contents

List of Figures	viii
List of Tables	xiv
1. Introduction	1
2. Literature Review	3
2.1. Water Droplet Erosion phenomenon	3
2.1.1. Time dependence of erosion	3
2.1.2. Droplet impact mechanism	5
2.1.3. Erosion mechanisms	10
2.2. Erosion test parameters	14
2.2.1. Impact speed	14
2.2.2. Droplet size	16
2.2.3. Surface roughness	17
2.2.4. Impact angle	18
2.2.5. Target mechanical properties	19
2.3. Mechanical surface treatments for WDE resistance	20
2.4. Deep rolling surface treatment.....	23
2.5. Suitable material	25
2.6. Objectives	29

3. Experimental methodology	30
3.1. Material selection.....	30
3.2. Sample preparation	32
3.2.1. T-samples.....	32
3.2.2. Test coupons	41
3.3. Characterization	43
3.3.1. Erosion testing	43
3.3.2. Tensile testing	47
3.3.3. Hardness testing.....	50
3.3.4. Laser scanning confocal microscopy	51
3.3.5. Scanning electron microscopy	51
4. Results and Discussions	52
4.1. Microstructure of 17-4 PH stainless steel	52
4.2. Tensile properties of 17-4 PH stainless steel	55
4.3. Micro-hardness	58
4.4. Surface roughness	61
4.5. Erosion performance.....	63
4.5.1. Demonstration of repeatability	64
4.5.2. Strain hardening results.....	67

4.5.2.1. Erosion behavior without DR treatment	67
4.5.2.2. Erosion behavior after DR treatment	78
4.5.2.3. Effect of the DR treatment.....	91
4.5.3. Stress relieving results	102
4.5.3.1. Damage mechanism in the SR-2 samples.....	106
5. Conclusions, contributions and Suggestions for future work.....	111
5.1. Conclusions.....	111
5.2. Contributions.....	112
5.3. Suggestions for future work.....	113
6. References	114
Appendix A	126

List of Figures

Figure 1.1 Typical fog cooling system of a gas turbine [3].....	2
Figure 2.1 (a) Cumulative erosion versus cumulative exposure duration curve (b) Instantaneous erosion rate versus cumulative exposure duration curve [4].	4
Figure 2.2 Three-line representation method [25].	5
Figure 2.3 (a) Shock envelope in the initial compression stage of droplet impact (b) Start of lateral jetting from the periphery after the critical point [30].	7
Figure 2.4 Radial jetting velocity as a function of Impact velocity. Based on [37] (1960).....	9
Figure 2.5 (a) Dilatational waves interfering with Rayleigh waves, (b) Dilatational waves transforming to transverse wave or vice-versa and interfering with Rayleigh waves [36].	10
Figure 2.6 Engel-Fyall mechanism of surface deformation seen in polymers [38].....	11
Figure 2.7 Ring crater from jet impact on patterned PMMA surface [14].	12
Figure 2.8 (a) Asperity breaks away by jetting from nearby droplet strike, (b) Micro-jet from successive impact enlarging the existing pit [44].	13
Figure 2.9 Erosion curves for Ti-6Al-4V tested at different impact speeds [58].	15
Figure 2.10 Erosion curves of Ti-6Al-4V tested with different initial surface roughness [46]....	18
Figure 2.11 Effect of droplet impact angle on erosion [5].....	19
Figure 2.12 Work hardened regions due to surface treatment and droplet impacts.	22
Figure 2.13 Deep rolling tool Ecoroll HG6-9R00-SL25.	23
Figure 2.14 Residual stresses due to DR and LSP treatments [78].	24

Figure 2.15 Change in hardness with aging of solution treated 17-4 PH stainless steel [96].....	28
Figure 3.1 CAD models of raw T-shape and the finished T-sample.	33
Figure 3.2 Flowchart of 17-4 PH stainless steel T-sample preparation.	33
Figure 3.3 CAD model of a disc and two raw T-shapes after waterjet cutting.....	35
Figure 3.4 Tensile dog-bone specimen.	36
Figure 3.5 CAD model top-view of raw T-shapes assembled in a disc.....	36
Figure 3.6 A resin casted mounting disc.....	37
Figure 3.7 Deep rolling setup.....	38
Figure 3.8 Deep rolling a mounting disc on lathe machine.	39
Figure 3.9 Deep rolled mounting disc.....	40
Figure 3.10 A finished T-sample.	41
Figure 3.11 CAD model of sample holder assembly.....	42
Figure 3.12 Schematic of water droplet erosion rig.....	43
Figure 3.13 Schematic of water droplet generation system.	45
Figure 3.14 Droplet size distribution of a 400 μm nozzle.	46
Figure 3.15 Tensile testing of dog-bone sample on Instron-3382 machine.....	48
Figure 3.16 Illustration of resilience and critical points on tensile stress-strain curve.....	49
Figure 3.17 Mitutoyo MVK-H1 micro-hardness testing machine.....	50
Figure 4.1 Microstructure of 17-4 P.H. steel in Condition-A.....	53

Figure 4.2 Microstructure of 17-4 PH steel in H925 condition.....	53
Figure 4.3 Microstructure of 17-4 PH steel in H1025 condition.....	54
Figure 4.4 δ-ferrite in the microstructure of 17-4 PH stainless steel.....	54
Figure 4.5 Engineering stress-strain curves of samples in H1025 condition.....	56
Figure 4.6 Engineering stress-strain curves of 17-4 PH stainless steel.....	56
Figure 4.7 Average micro-Vickers hardness of 17-4 PH stainless steel before and after deep rolling.....	60
Figure 4.8 Surface appearance of Condition-A samples with DR treatment and 1200grit ground finish.....	63
Figure 4.9 Repeatability WDE test of 17-4 PH stainless steel in As-Received condition at impact speed of 300 m/s.....	64
Figure 4.10 Instantaneous erosion rate curve of 17-4 PH stainless steel in As-Received condition at impact speed of 300m/s.....	65
Figure 4.11 Erosion curves of Condition-A vs H925 without the DR treatment at impact speed of 250m/s.....	68
Figure 4.12 Erosion curves of Condition-A vs H1025 without DR treatment at impact speed of 250 m/s.....	69
Figure 4.13 Evolution of craters in Condition-A ground versus H925 ground tested at 250 m/s. These macrographs correspond to Figure 4.11.....	69
Figure 4.14 Evolution of craters in Condition-A ground versus H1025 ground tested at 250 m/s. These macrographs correspond to Figure 4.12.....	70

Figure 4.15 Erosion curves of Condition-A vs H925 without the DR treatment at impact speed of 300m/s.....	71
Figure 4.16 Erosion curves of Condition-A vs H1025 without the DR treatment at impact speed of 300m/s.	71
Figure 4.17 Evolution of craters in Condition-A ground versus H925 ground tested at 300 m/s. 72	
Figure 4.18 Evolution of craters in Condition-A ground versus H1025 ground tested at 300 m/s.	72
Figure 4.19 Erosion curves of ground samples at impact speed of 250 m/s.....	73
Figure 4.20 Erosion curves of ground samples at impact speed of 300 m/s.....	74
Figure 4.21 Radar chart showing erosion incubation time of ground samples tested at 250m/s and mechanical properties of each condition.....	75
Figure 4.22 Radar chart showing erosion incubation time of ground samples tested at 300m/s and mechanical properties of each condition.....	75
Figure 4.23 Schematic showing progression of yield point due to strain in ground samples.	77
Figure 4.24 Erosion curves of Condition-A vs H925 with DR treatment at impact speed of 250m/s.....	80
Figure 4.25 Erosion curves of Condition-A vs H1025 with DR treatment at impact speed of 250m/s.....	80
Figure 4.26 Evolution of craters in Condition-A DR versus H925 DR tested at 250 m/s.....	81
Figure 4.27 Evolution of craters in Condition-A DR versus H1025 DR tested at 250 m/s.....	82

Figure 4.28 Erosion curves of Condition-A vs H925 with DR treatment at impact speed of 300 m/s.....	83
Figure 4.29 Erosion curves of Condition-A vs H1025 with DR treatment at impact speed of 300m/s.....	84
Figure 4.30 Evolution of crater in Condition-A DR versus H925 DR tested at 300 m/s.	84
Figure 4.31 Evolution of crater in Condition-A DR versus H1025 DR tested at 300 m/s.	85
Figure 4.32 Erosion curves of DR samples at impact speed of 250 m/s.	86
Figure 4.33 Erosion curves of DR samples at impact speed of 300 m/s.	86
Figure 4.34 Radar chart showing erosion incubation time of DR samples tested at 250m/s and mechanical properties of each condition.....	88
Figure 4.35 Radar chart showing erosion incubation time of DR samples tested at 300m/s and mechanical properties of each condition.....	88
Figure 4.36 Schematic showing progression of yield point due to strain in DR samples.	90
Figure 4.37 Superimposed erosion curves of ground and DR samples in Condition-A at 250m/s impact speed.....	93
Figure 4.38 Superimposed erosion curves of ground and DR samples in H925 at 250m/s impact speed.	94
Figure 4.39 Superimposed erosion curves of ground and DR samples in H1025 at 250m/s impact speed.	94
Figure 4.40 Preferential micro-pit formation on the deep rolled surface at the end of incubation period.	95

Figure 4.41 Transgranular fracture in micro-pits.....	96
Figure 4.42 Pit growth by intergranular fracture and material folding.....	97
Figure 4.43 Material upheaval and subsurface cracks during crater expansion from erosion.....	98
Figure 4.44 Deformed surface in the deep pockets with grain boundary cracks.....	99
Figure 4.45 Section showing internal crack in the overhanging material above deep pocket....	100
Figure 4.46 Section showing subsurface expansion of erosion crater by tunneling.....	101
Figure 4.47 Erosion curves of SR-1 test at impact speed of 300 m/s.	103
Figure 4.48 Erosion curve of SR-2 test at impact speed of 300 m/s.....	104
Figure 4.49 Macrographs showing pit progression in SR-2 test samples.....	105
Figure 4.50 Pit growth comparison during SR-2 test.	107
Figure 4.51 Difference in growth mechanism in samples of SR-2 test.	108
Figure 4.52 Severe plastic deformation on fractured surface in the relieved test sample of SR-2 test.	109
Figure 4.53 Schematic of intermittent stress relieving in the relieved test sample during erosion test.	110
Figure A.1 Spouting hole in polished X22CrMoV12-1 stainless steel sample.	126
Figure A.2 Spouting holes in deep rolled 17-4 PH stainless steel samples.	126
Figure A.3 Schematic showing the formation of a spouting hole by an erosion crater.....	127

List of Tables

Table 3-1 Composition of 17-4 PH stainless steel.....	31
Table 3-2 Typical composition of X22CrMoV12-1 stainless steel	32
Table 3-3 Deep rolling process parameters.	40
Table 3-4 Erosion test parameters and conditions used.....	47
Table 4-1 Tensile properties summary of 17-4 PH stainless steel.....	57
Table 4-2 Micro-Vickers hardness of polished and DR treated surface of 17-4 PH samples.	59
Table 4-3 Micro-Vickers hardness in X22CrMoV12-1 stainless steel.....	61
Table 4-4 Average surface roughness of erosion samples.....	62
Table 4-5 Acceptable difference in mass loss and erosion rate during maximum erosion rate stage.	66
Table 4-6 Summary of relative properties and erosion performance of ground samples for each condition.	76
Table 4-7 Summary of relative properties and erosion performance of DR samples for each condition.	89
Table 4-8 Summary of incubation times and maximum erosion rate in DR and ground samples.	92

1. Introduction

Gas turbine efficiency and performance are dependent on the ambient air conditions of the turbine: the efficiency deteriorates at higher ambient temperatures [1], [2]. Since the power generated by a turbine and work done by the compressor are directly proportional to the density of the inlet air, it is essential to have a higher density of inlet air by lowering its temperature to obtain a higher output power of the turbine or lower work done by the compressor at the same speeds. This is made possible by cooling the inlet air. Inlet fog cooling, as shown in Figure 1.1 [3], has been found to be one of the most effective ways of intake air cooling in gas turbines used in the power generation industry [1], [2]. This method of cooling has however been proven to cause erosion damage of the compressor blades, especially at their leading edge due to impacting droplets, resulting in reduced performance and reduced service life of blades [4]–[6]. Erosion is also seen in fan and compressor blades of aircraft engines due to rain and hail [7], [8]. This phenomenon of erosion damage from repeated impact of water droplets is called Water Droplet Erosion (WDE).

The WDE phenomenon is also observed in the low pressure sections of steam turbines where some of the steam condenses to form droplets which hit the turbine blades that are rotating at high speeds causing them to erode, especially at their leading edge, and thereby losing some of the power generated [4], [9]–[13]. Erosion of aircrafts and rockets passing through rain at high speeds is also a problem which has garnered attention along with turbine and compressor blade erosion [7], [8], [14]–[16]. More recently, erosion of wind turbine blades has become an important topic of research. Wind turbine blades also experience severe erosion at the leading edge due to rain, hail and sand particles [17]–[19]. This leads to a reduction in efficiency and loss of annual energy production [19], [20].

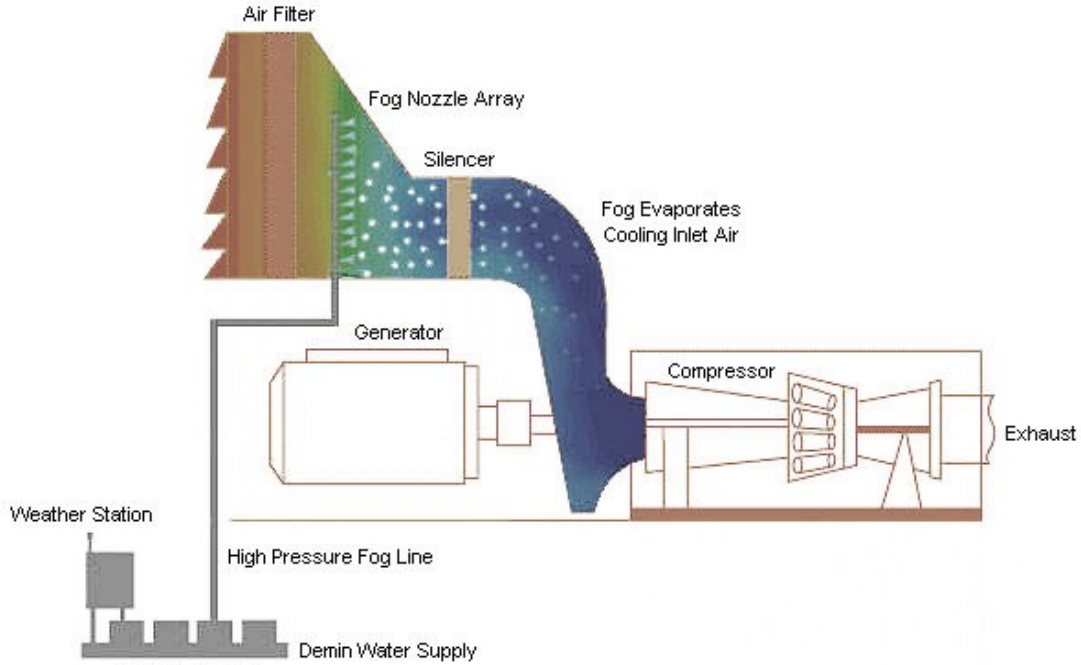


Figure 1.1 Typical fog cooling system of a gas turbine [3].

Erosion by cavitation, which is seen in applications ranging from impellers of ships to water pipelines in power plants, is found to be similar to WDE in its behavior [21]–[23]. WDE and cavitation erosion are therefore referred to as allied phenomena [4]. However, their degree of similarity in erosion mechanism is yet to be ascertained [4].

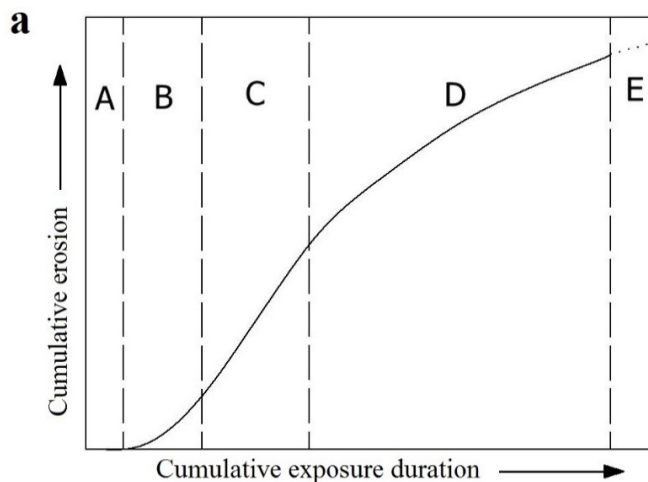
2. Literature Review

2.1. Water Droplet Erosion phenomenon

Water Droplet Erosion (WDE) has been defined as the progressive loss of original material from a solid surface due to continuous exposure to impacts by liquid droplets or jets [24]. WDE is a complex phenomenon which is time dependent and is significantly influenced by a number of parameters such as impact speed, droplet size, impact angle, liquid properties, target surface properties and the properties of the solid material [4].

2.1.1. Time dependence of erosion

The time dependence of the WDE phenomenon is well summarized in the ASM handbook [4] and is typically characterized by the cumulative mass loss versus the exposure duration or the number of impingements. The erosion rate curve gives the instantaneous rate of mass loss with respect to the exposure duration or the number of impingements. Characteristic erosion curves as shown in the Figure 2.1, are commonly divided into five stages: Incubation, Acceleration, Maximum erosion rate, Deceleration, and Terminal steady erosion rate.



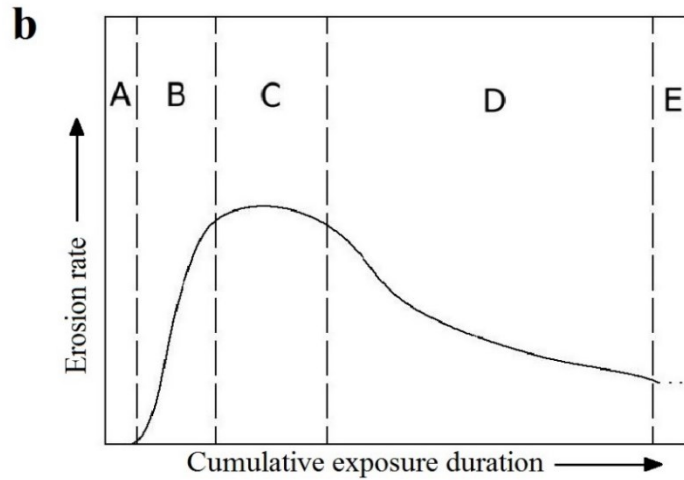


Figure 2.1 (a) Cumulative erosion versus cumulative exposure duration curve (b) Instantaneous erosion rate versus cumulative exposure duration [4].

Each of these five stages is described as follows:

Incubation stage (A): No measurable material loss with some surface metallurgical changes.

Acceleration stage (B): Erosion rate increases along the duration to reach a maximum.

Maximum erosion rate stage (C): Erosion rate is steady with little to no variation.

Deceleration stage (D): Erosion rate declines to a fraction of maximum erosion rate.

Terminal stage (E): Erosion rate remains constant once again indefinitely. This stage is also referred to as ‘catastrophic stage’ for some brittle materials and coatings which contrarily show an increased rate of erosion.

ASTM G73 standard [25] proposes a simplified method called the ‘Three-line representation’ method to be able to easily differentiate between the stages of erosion curves. Figure 2.2 shows the Three-line representation method. In this method, each line essentially indicates three stages: Incubation, Maximum erosion rate and the Terminal erosion rate.

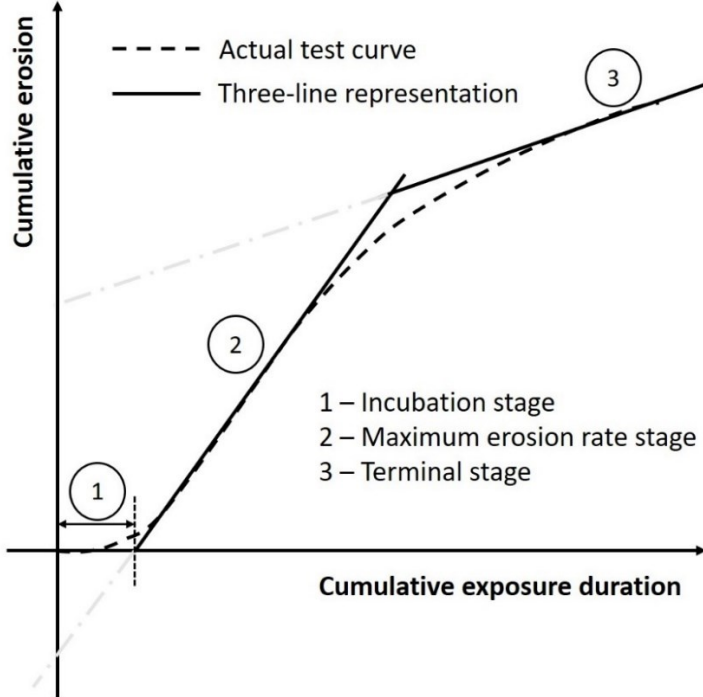


Figure 2.2 Three-line representation method [25].

In this method of representation, the acceleration stage is neglected as a transition between the incubation and the maximum erosion rate regions of the curve. However, few materials atypically show a distinct acceleration stage which is reflected in their instantaneous erosion rate curve as a small peak or a step before actually rising to the maximum erosion rate [4]. This atypical behavior is reportedly seen in some Titanium alloys [4]. Incubation, acceleration and maximum erosion rate stage are considered in this work.

2.1.2. Droplet impact mechanism

Extensive research was done in the past to understand the droplet impingement mechanics, which could possibly provide insights into the stresses generated during the impacts. At the first instance of a liquid droplet touching the solid target, compression waves are sent into the liquid and as the droplet contact periphery expands over the target surface from the center of impact, new wavelets are generated at each instance from the contact edge [26],

[27]. These wavelets constructively interfere and form a shock envelope attached to the contact edge as shown in Figure 2.3 (a). Due to the droplet curvature, the contact edge speed is initially greater than the speed of sound in liquid and it eventually falls down to zero as the center of the spherical droplet reaches the target surface. Theoretically, the liquid encompassed by the shock envelope within the droplet remains compressed and exerts high pressures over the target before the jetting starts to happen at a ‘critical point’ where the shock front detaches from the contact periphery of the droplet over the target surface [26], [28]. Alternatively, it can also be said that the jetting starts to happen when the contact edge speed falls below the shockwave speed of the liquid and relieves the pressure developed from the compressed liquid. At the critical point, contact edge angle ‘ β ’ is given by $\sin^{-1}(V/C)$ where ‘V’ is the impact velocity and ‘C’ is the speed of sound in a liquid medium [12], [26], [28], [29]. Experimentally observed β values for the start of lateral outflow jetting have always been found to be greater than the theoretically calculated ones [28], [30]. The small β values at the critical point suggests that the impact pressures are experienced over a region much smaller than the droplet size.

In 1928, Cook [31] first used the water hammer pressure as an average of the high pressures experienced by a rigid target during the initial stages of impact. The magnitude of “water-hammer” pressure ‘P’ is given by equation-(1) in which ‘ ρ ’ is the density of the liquid, ‘C’ is the speed of sound in the liquid and ‘V’ is the impact velocity. This does not take into account the elasticity of the target material.

$$P = \rho CV \quad \dots\dots\dots (1)$$

As cited in the literature [14], [32], in 1933, De Haller estimated the pressure considering the acoustic properties of the target material as shown in equation-(2).

$$P = \frac{V\rho_1 C_1}{\left(1 + \frac{\rho_1 C_1}{\rho_2 C_2}\right)} \quad \dots\dots\dots (2)$$

Where, ‘ ρ_1 ’ and ‘ ρ_2 ’ are the density of liquid and target material respectively; ‘ C_1 ’ and ‘ C_2 ’ are the speed of sound in liquid and in the target material respectively; and ‘ V ’ is the relative speed between liquid and target. These equations do not include the shockwave effects arising from the droplet curvature [32].

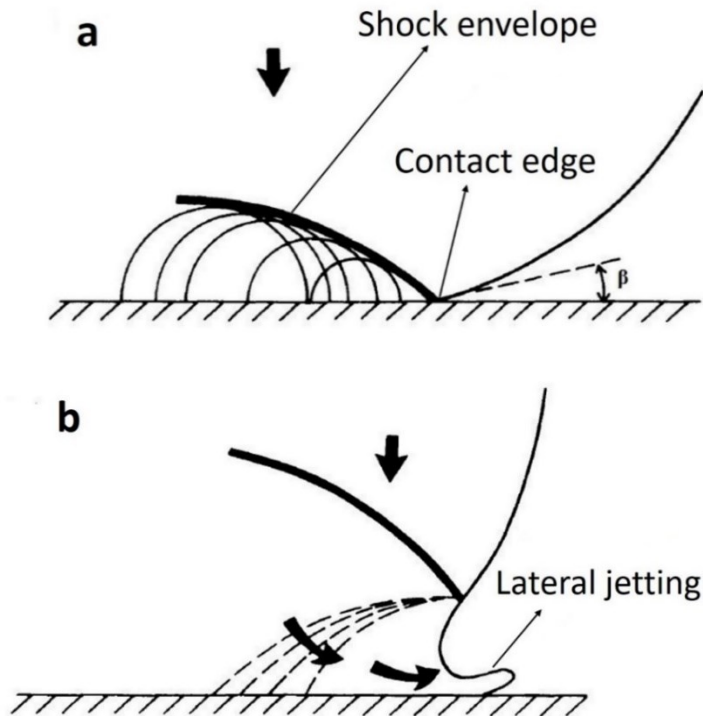


Figure 2.3 (a) Shock envelope in the initial compression stage of droplet impact (b) Start of lateral jetting from the periphery after the critical point [30].

But as it turns out that the shock wave velocity is higher than the acoustic velocity ‘C’ due to different properties of the liquid in the compressed region, in 1967 Heymann [10] suggested equation-(3) as a modified form of the water hammer equation after defining the shock wave velocity as a function of impact speed ‘V’.

$$P = \rho CV \left(1 + \frac{KV}{c}\right) \quad \dots\dots\dots (3)$$

where ‘P’ is the pressure generated at impact, ‘ ρ ’ is the density of liquid and ‘K’ is a non-dimensional constant. The use of K=2 for water was justified by Heymann [10] through plotting the non-dimensional shock front velocity factor versus the particle velocity Mach number, which had a slope of 2 at Mach number <1 for water. Later in 1969, Heymann [26] from his analytical model concluded that the peak pressures could be as high as three times the magnitude of water hammer pressure occurring at the critical point for a very brief period. Peak pressure at the critical point is given by Equation-(4).

$$P = \rho CV [2 + (2K - 1) M_0] \quad \dots\dots\dots (4)$$

Where ‘M₀’ is the Mach number of the water droplet given by the ratio V/C.

In 1979, Rosenblatt et al. [33] used the finite difference method to study the pressure characteristics to obtain the magnitude and time of peak pressure during the initial stages of droplet impact on a rigid target. The peak pressure occurred when the shock wave leaves the wall at about 30 ns. In his analytical model, Lesser [27] is in agreement with the magnitude of pressure generated in Rosenblatt’s numerical model, however, the exact solution of Lesser shows the time delay in the numerical model thereby rendering the model questionable [34]. These numerical and analytical models provide an approximate magnitude of the high pressures generated at impact.

Initial attempts were made to experimentally measure the average pressures experienced over the impact area during each droplet impact, but the pressures obtained were significantly less than the theoretically calculated values [14], [28]. Later, Brunton and Rochester [35] were able to measure the pressure distribution over a droplet impact area of a 5mm droplet that impacted at 100 m/s and found peak pressures away from the central axis reaching as high as $2.5\rho CV$, which is in agreement with Heymann’s [26] initial estimate of about $3\rho CV$. As the

lateral jetting starts, the pressure on the central axis of droplet decreases to Bernoulli's stagnation pressure which is much lower than the peak impact pressure [36]. High magnitudes of pressure over small regions are expected to induce strain in the material. The effect of the strain, induced from droplet impacts, on the incubation time is studied in this work.

High speeds of lateral jetting during the collapse of a droplet were observed by researchers. Engel [32] studied the free falling water droplets amounting to impact velocities of less than 10m/s. She reported a hyperbolic reduction in the velocity of jets with respect to time once the jetting starts, although uncertain about its exact starting time. Jenkins and Booker [37] were able to measure the very high lateral jet velocity at the start of jetting for impact velocities ranging from 100 to 1140m/s. Figure 2.4 shows the lateral jetting velocity as a function of impact velocity [37]. Bowden and Brunton's [14] findings of initial lateral jetting speed to be 2.3 times that of an impact velocity of 680m/s over a PMMA substrate are in line with the graph shown below in Figure 2.4. These high speeds of jetting liquid have a potential to cause damage in the material.

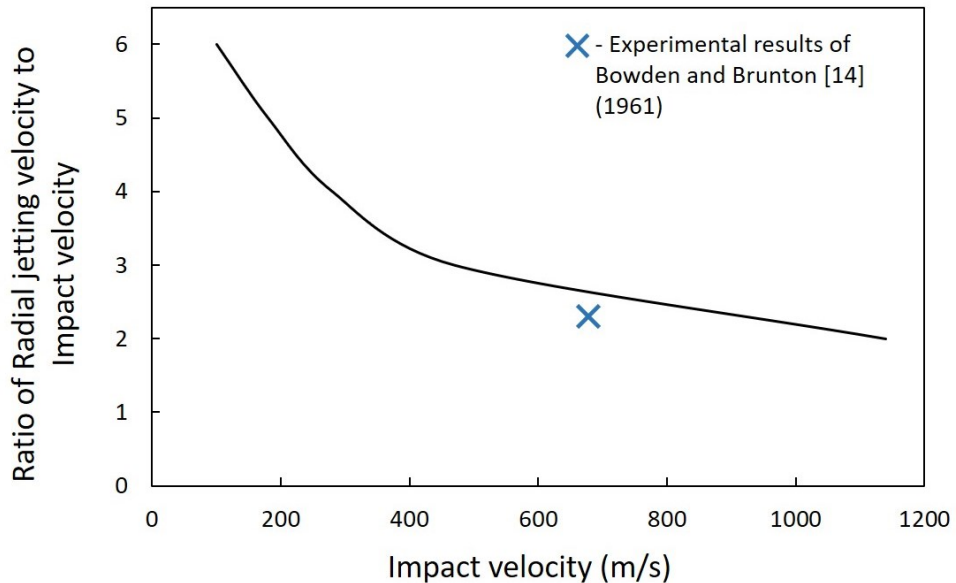


Figure 2.4 Radial jetting velocity as a function of Impact velocity. Based on [37] (1960).

2.1.3. Erosion mechanisms

Throughout the literature, single impact [14], [29], [38] and multiple impact studies [28], [35], [39]–[41] were conducted to understand the erosion mechanisms at different stages. In the initial stages of erosion, the damage is believed to be initiated mainly due to the high pressures generated at impact and also due to high velocity lateral jetting [11], [34], [35], [39]. The magnitude of the pressures generated during the impacts is discussed in section 2.1.2.

Longitudinal stress waves, transverse shear waves and surface Rayleigh waves are generated at the site of impact and are expanded into the material with speeds C_1 , C_2 and C_R respectively as shown in Figure 2.5. These stress waves and their constructive interference in various ways, as shown by Figure 2.5, are suspected to cause damage around the impact zone [14], [29], [36]. This damage mechanism becomes predominant when the surface is either non-homogenous like in a coating, when the target material is thin, or when it has irregularities beneath the surface which potentially act as sites of reflection of these waves [14], [34], [36], [41], [42].

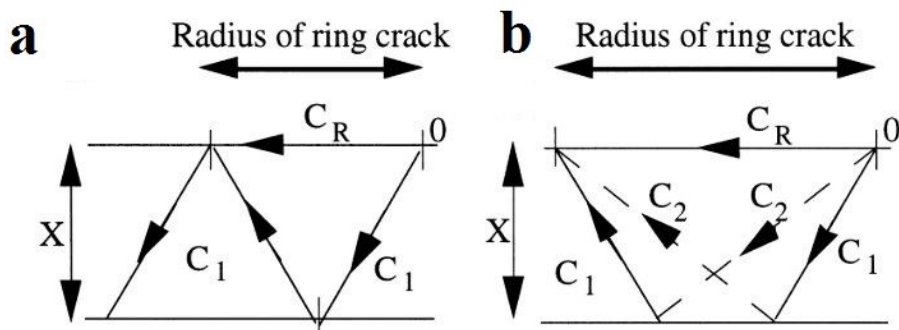


Figure 2.5 (a) Dilatational waves interfering with Rayleigh waves, (b) Dilatational waves transforming to transverse wave or vice-versa and interfering with Rayleigh waves [36].

Engel and Fyall conducted a series of single impact studies from 1955 to 1970 on various polymers, metals and ceramics. In highly deformable materials like Poly Methyl-

Methacrylate (PMMA) polymer, initial deformation of the surface occurring under a single impact is explained by the Engel-Fyall mechanism which is shown in Figure 2.6 [38]. According to the mechanism, initially the flat surface XAB^IY under the pressure developed during the droplet impact deforms to XA^IB^IY and as the pressure is reduced to zero with the onset of jetting, the surface takes the form XLABMY as can be seen in Figure 2.6. The surface profiles XLA and BMY are a result of the stretched material on the surface. For an impact velocity of about 300m/s and droplet size of 2mm, XY was 1.1mm [38]. This indicates the area of influence being much smaller than the droplet size for PMMA and is expected to be even smaller in case of metals.

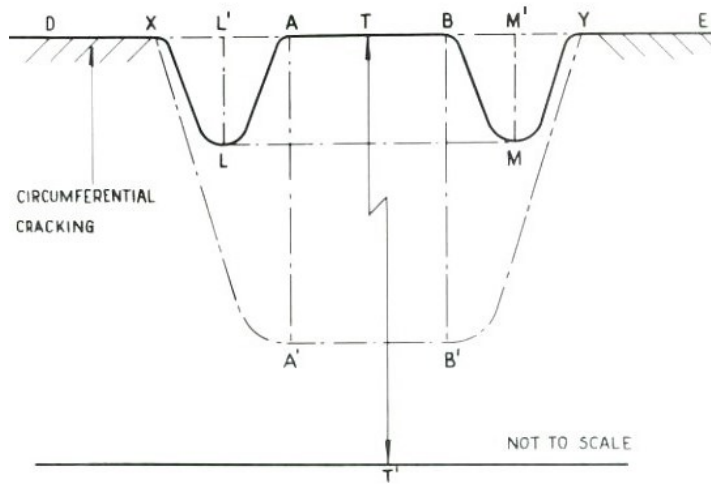


Figure 2.6 Engel-Fyall mechanism of surface deformation seen in polymers [38].

Bowden and Brunton [14] studied single impacts using high velocity jets, which behave like a spherical droplet in the initial stages of impact, on a patterned PMMA substrate and found circumferential damage with a central undamaged region (Figure 2.7), as described by the above described Engel-Fyall mechanism. Figure 2.7 also shows shear deformation in the periphery of the circumferential damaged region of the patterned PMMA substrate [14].

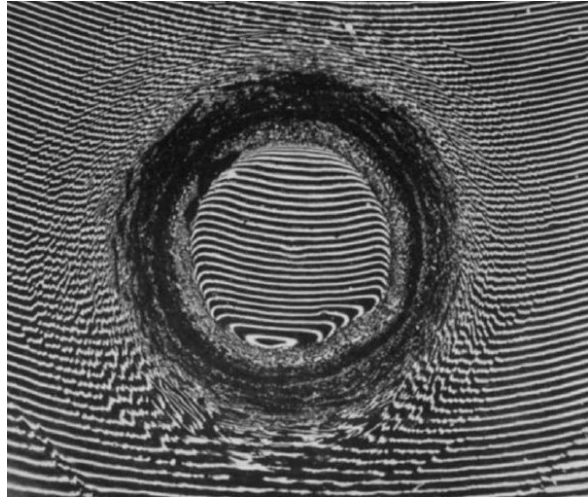


Figure 2.7 Ring crater from jet impact on patterned PMMA surface [14].

In metals, the central part of the impacted region deformed to form a depression and was surrounded by a peripheral shear deformation (similar to that seen in polymers), preferentially near the grain boundaries, slip lines and at the interface of secondary phases in multiphase alloys [14]. In most of the applications, erosion occurs due to repeated impacts and the damage mechanism is believed to be fairly complex and largely depends on the plastic properties of metals in the initial stages of erosion [11], [28], [34], [39], [43]. Therefore, studying the effect of plastic deformation behavior of the target material is important. This work will help reveal the effect of strain hardening on the WDE performance.

It is a common understanding that the continual droplet strikes plastically deform the initial plain surface creating depressions and asperities [14], [28], [30], [44]. When these asperities are sufficiently large and weak, radial jetting from a nearby impacting droplet breaks them thereby creating pits [11], [28], [44], [45] as shown in Figure 2.8 (a). Therefore, initial surface roughness also plays a crucial role in the start of erosion due to the interaction between surface irregularities and the jetting [46]. Surface roughness has also been found to influence the jetting behavior itself [47]. Newly created shallow pits are believed to expand in size by

plastic deformation under successive droplet impacts and when they are sufficiently large, the impacting droplet first touches a pit at its edges and shoots down a microjet which further deepens the existing pit [30], [44], [45] as shown by Figure 2.8 (b).

Hydraulic penetration is also a widely discussed damage mechanism, especially observed during the advanced stages of erosion [34], [41], [48]–[52]. As a water droplet strikes over the surface of an existing crater with cracks and cavities, water penetrates into those spaces expanding the subsurface cracks and causes tunneling [51], [53]. When these expanded subsurface cracks coalesce, they can remove chunks of material from above them and is hereby found to be one of the most deteriorative mechanisms in advanced stages of erosion [41], [50]. Fujisawa et al. [54] tried to study erosion on rough surfaces by making grooves, to replicate developed erosion craters, and found that groove depth relative to droplet size (called ratio D/d) plays a crucial role in the development of craters. It was observed that a large D/d ratio causes the groove to expand in depth while a small D/d ratio causes the groove to expand laterally [54]. The importance of droplet impact and jetting location was also discussed with respect to crater development [54].

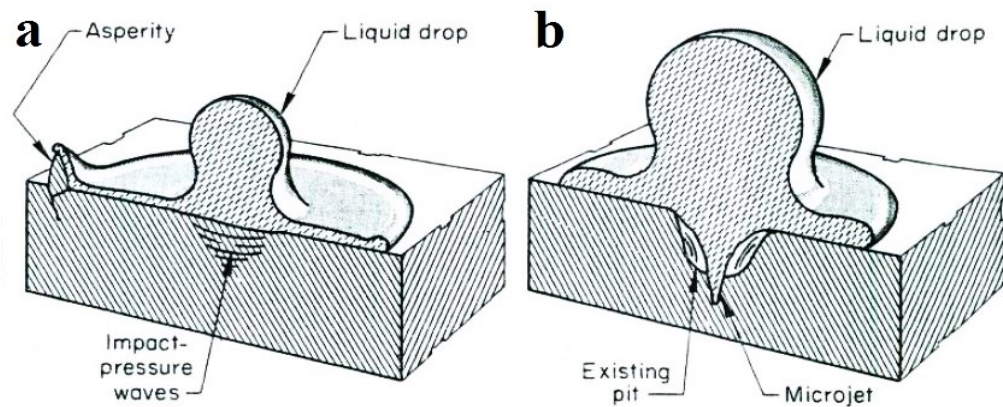


Figure 2.8 (a) Asperity breaks away by jetting from nearby droplet strike, (b) Micro-jet from successive impact enlarging the existing pit [44].

Researchers [41], [55], [56] have in recent times studied erosion behavior by applying various mechanical surface treatments to delay erosion. Erosion mechanisms in surface treated metals are further discussed in section 2.3. The effect of strain induced from surface treatment is studied in this work.

2.2. Erosion test parameters

Erosion is dependent on impact conditions as well as target properties. Some of the parameters that are found to significantly affect erosion behavior in the literature are discussed here.

2.2.1. Impact speed

Impact speed has been found to be one of the most influential impact parameters and is widely discussed in the literature. While it has always been observed throughout the literature [4], [10], [12], [13], [42], [50], [57]–[59] that erosion is increased and accelerated with the increase in impact speed, as shown in Figure 2.9, no definitive analytical relation has ever been established between erosion rate and impact speed. Heymann [10] summarized various empirical relations between the impact speed ‘V’ and the erosion rate ‘E’ in equations-(5) to (7) where ‘ V_C ’ is the threshold speed below which no erosion was seen even after long exposures, ‘a’ is a constant.

$$E = aV^n \quad \dots\dots\dots (5)$$

$$E = a(V - V_C)^n \quad \dots\dots\dots (6)$$

$$E = ae^{nV} \quad \dots\dots\dots (7)$$

These relations are unique for each material and are largely dependent on the droplet size and other test conditions. Hoff et al. [57] observed different threshold speeds and different

slopes of erosion depth versus impact speed curves for different ceramic and polymer materials. It is not a well-established concept partly because different threshold speeds have been reported for the same target material used in different experimental set-ups and partly because materials erode after impractically long exposure to low speed impacts [10]. However, the power law relation shown in equation-(5) is independent of the threshold speed and has been widely used to show velocity dependence of erosion rate. For instance, Gujba et al. [50] reported accelerated damage as impact speed was increased and the value of exponent ‘n’ for Ti-6Al-4V to be 9.9 using 463 μ m droplets. Under similar test conditions, Mahdipoor et al. [58] used a rationalized erosion rate and found the value of ‘n’ to be 8.9 and 12.5 for Ti-6Al-4V and TiAl alloys respectively. As summarized by Gujba et al. [50] the values of ‘n’ were found to be varying from 3 to 14 in the literature for different materials. Van der Zwag et al. [60] showed an increase in failure probability and greater residual stress in brittle materials with an increase in impact velocity. Ma et al. [51] found an increase in damage within the same turbofan blade in the regions that experienced greater impact velocities.

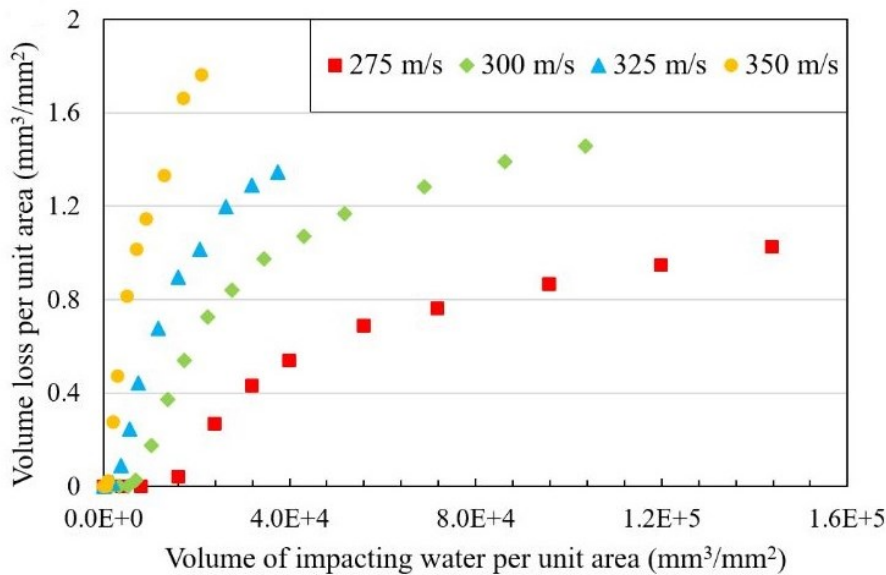


Figure 2.9 Erosion curves for Ti-6Al-4V tested at different impact speeds [58].

The acceleration in erosion, i.e. the shortening of incubation time and increase in rate of acceleration, with an increase in impact speed is attributed to an increase in impact pressure [10], [32], [61], an increase in the time duration of impact pressure pulse [29], [62] and an increase in kinetic energy [4], [63]. In the WDE tests, the shortening of incubation time with greater impact velocities makes the identification of the differences in incubation times difficult. Therefore, the lower impact speeds are used in this study to better discern the differences.

2.2.2. Droplet size

An increase in the droplet size has shown an increase in erosion rate [4], [13], [59], [64]. The primary reason for greater damage with larger droplet size is believed to be due to a longer duration and the area over which the target experiences peak pressures [36]. According to Field [36], equation-(8) gives the time taken (τ) from initial contact to the release of pressure built during impact, with the start of jetting.

$$\tau = \left(\frac{3rV}{C^2} \right) \quad \dots\dots\dots (8)$$

Here ‘r’ is the radius of curvature of the droplet; ‘V’ and ‘C’ are the impact speed and the speed of sound in the impacting liquid respectively. Unlike water hammer pressure equations, which are independent of droplet size, jetting commencement time is directly proportional to the contact radius of curvature of the droplet. It is also for this reason that flattened droplets are thought to cause more damage due to their larger radius of curvature during the compressive stage of impact, developing greater stress distribution [36], [65]. While it is imperative that an increase in droplet size means increase in kinetic energy transferred, the amount of kinetic energy transferred remains uncertain. Kirols et al. [63] analyzed the normalized volumetric erosion with respect to input kinetic energy from droplets and concluded

that the energy absorbed is indeed dependent on impacting conditions including droplet size. The droplet size is therefore kept constant in this work.

2.2.3. Surface roughness

Surface roughness in the form of depressions and asperities is known to drastically influence various aspects of WDE [14], [28], [45]–[47]. Greater surface roughness ensures a greater number of potential sites for cracking and furthers the formation of more asperities and pits [45]. The interaction of asperities with the high speed lateral jetting is a deciding factor in delaying the incubation period [46]. Kirols et al. [46] varied the surface roughness of Ti-6Al-4V and found that the incubation period can be greatly elongated by improving the surface finish as can be seen in Figure 2.10. A similar trend was observed by Fujisawa et al. [54]. In addition, they [54] reported on the dependence of erosion on relative roughness with respect to droplet size. It is therefore crucial to have similar starting surface roughness to be able to properly compare the erosion properties of the test samples. The effect of surface roughness was duly acknowledged by Gujba et al. [55] and was vastly minimized, if not eliminated, by polishing the untreated reference samples to nearly the same surface finish as the Ultrasonic Nano-crystalline Surface Modification (UNSM) treated samples. O’Carroll et al. [66] tested various polymeric materials and found a strong correlation between the rate of change in surface roughness and the rate of mass loss in different periods of erosion and concluded that the mechanism which induces resistance to roughening during incubation period also results in improved resistance to the mass loss. Considering the influence of surface roughness on erosion incubation time in multiple ways, only the samples with similar surface preparation were tested together in this work. This effectively eliminates the influence of surface roughness on erosion incubation time.

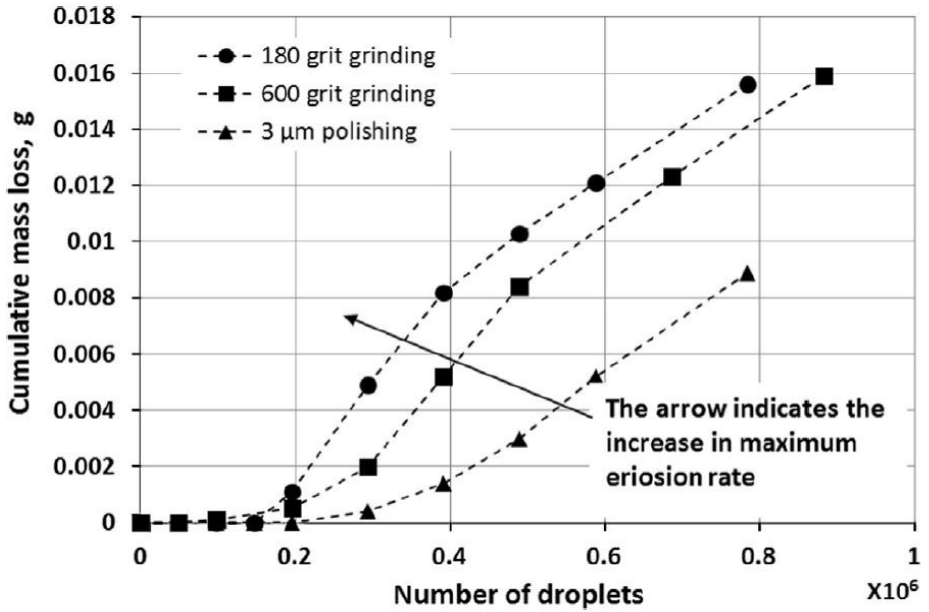


Figure 2.10 Erosion curves of Ti-6Al-4V tested with different initial surface roughness [46].

2.2.4. Impact angle

Baker et al. [67] stated that the erosion rate is primarily dependent on the component of impact velocity which is normal to the surface in the initial stages. However, in the advanced stages of erosion, the tangential component of velocity also becomes important due to the surface roughening achieved by erosion [4]. Ahmad [5] studied the effect of impact angle on erosion damage and presented a graph as shown in Figure 2.11 which shows that the maximum damage is at an impact angle of 90° . This is the reason why it is recommended to maintain the incident angle at the leading edges of aircraft's surfaces as low as possible to minimize the erosion damage [8], [15]. In this work, an impact angle of 90° is used as the most adverse effects can be expected at this impact angle.

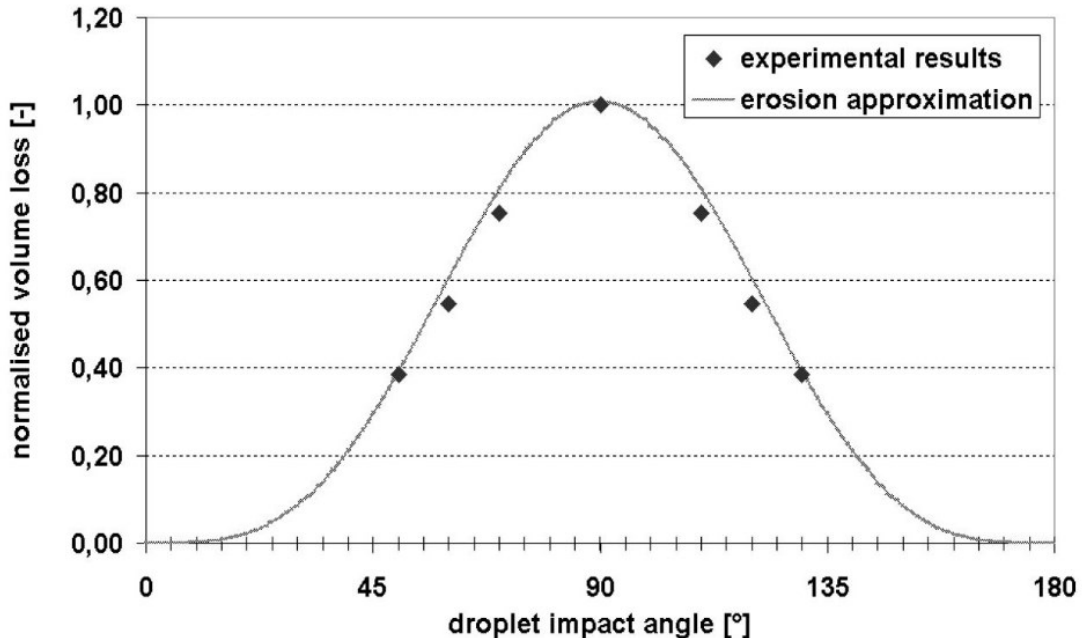


Figure 2.11 Effect of droplet impact angle on erosion [5].

2.2.5. Target mechanical properties

Though no single mechanical property is found to be directly related to erosion, several attempts were made in the past to relate a mechanical property of a target to its erosion behavior. Greater hardness has generally shown relatively better erosion resistance in metals [13], [68]–[70]. Hoff et al. [57] described maximum erosion rate as a function of ultimate tensile strength raised to a power of 1.8. Rieger [43] reported a correlation between erosion loss and ultimate strength of aged hardened conditions of a copper-beryllium alloy but did not report the effect of other properties such as hardness and strain hardening exponent. Correlating strength, microhardness and strain hardening exponent to the erosion incubation will be attempted in this current work. An attempt was made to relate elastic resilience, defined as $(\sigma_y^2/2E)$, to erosion resistance [71], but yet again, other properties which have shown strong correlation in some other works were ignored. Nevertheless a strong dependence of elastic resilience on the erosion resistance of the material was observed [9], [71]. Therefore, the

erosion behavior will also be evaluated with respect to elastic resilience along with other properties in this work.

2.3. Mechanical surface treatments for WDE resistance

The repetitive nature of impacts in the erosion problem has led some researchers to believe that fatigue is a probable erosion mechanism in metals [39], [42], [69]. However, to verify these claims, mechanical surface treatments which are proven inhibitors of fatigue crack growth were performed on samples and were then tested for erosion damage [41], [55], [56]. Those treatments, even though some have induced Compressive Residual Stresses (CRS), showed little to no enhancement in the erosion performance. This lack of improvement is attributable to embrittlement from strain hardening, due to plastic deformation from those surface treatments, which supposedly negated the beneficial CRS during the initial stages and hence, showed no improvement [41]. In the advanced stages of erosion, when the treated top layer with beneficial CRS eroded away, few fatigue striation marks were observed in both the treated and the non-treated samples alongside plastic deformation [41], [55], [56]. The fact that little to no improvement was seen in various mechanically surface treated samples shows that fatigue is a non-dominant erosion mechanism, at least in the tested metals.

Heymann [45] predicted that some prior work hardening could improve erosion performance while excessive hardening could be detrimental. Among erosion studies, which employed cold working to induce surface hardening, Thomas and Brunton [39] found that erosion resistance of cold worked copper is reduced and attributed it to lower number of impacts needed to achieve full hardening in the case of cold worked specimens. Also, increased cold working showed greater loss of erosion resistance in polycrystalline copper [39]. On the contrary, Ma et al. [41] have seen negligible change in erosion resistance of Ti-6Al-4V alloy

even with Deep Rolling (DR) treatment. This indifference was attributed to the beneficial effect of CRS from DR treatment being negated by the embrittlement caused by the work hardening of the DR treatment [41]. Similar indifference in erosion performance was observed by Gujba et al. [56] when Laser Shock Peening (LSP) treatment, which is known for inducing CRS without significantly hardening the surface, was used instead of DR treatment on Ti-6Al-4V. The Ultrasonic Nanocrystalline Surface Modification (UNSM) treatment showed improvement in erosion performance especially at lower impact speeds in Ti-6Al-4V, and it was concluded that surface hardening along with grain refinement and CRS are required to improve erosion performance by mechanical treatments [55]. Similar conclusions were made by Herbert [72] who studied the effects of hardening in steels on erosion performance without surface treatments.

It is important to note that the surface work hardening of metals can essentially be from both the mechanical surface treatments and the droplet impacts. A work hardened layer created by a surface treatment is expected to further work harden when subjected to droplet impacts, as illustrated in Figure 2.12, until its failure due to impact pressures [39], [44], [56]. As discussed above, the work hardening created by a surface treatment is a potential contributor to erosion failure by embrittlement and needs further investigation. However, untreated metals will experience surface hardening due to repeated droplet impacts [28], [39]. This hardening, due to repeated impacts during erosion, remains controversial whether it is aiding or resisting the erosion damage.

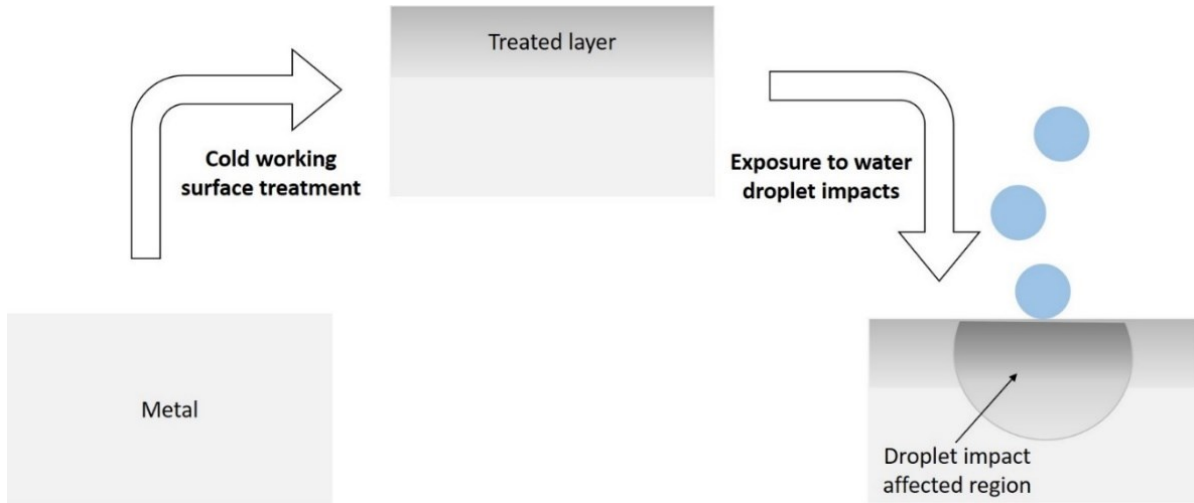


Figure 2.12 Work hardened regions due to surface treatment and droplet impacts.

Work hardening due to strain accumulation from droplet impacts is also considered beneficial for prolonging the incubation period to some extent [4]. Earlier, Rieger [43] intermittently relieved the hardening accumulated during impacts by annealing aluminum samples at 510°C and found the annealed samples eroding much quicker than the ones which were not annealed. Heyman [4] attributed this reduction in performance of annealed samples to the loss of additional hardness gained by the strain hardening from impacts. The reduction in incubation time could however be a result of loss of strength or change in grain structure due to higher annealing temperature used for aluminum instead of just relieving accumulated strain.

In this work, a precipitation hardenable stainless steel, which has very low strain hardening exponent values in its various aged conditions, is used to study the erosion behavior under the influence of DR surface treatment. The low strain hardening of this stainless steel shall help in minimizing the hardening due to DR treatment, which is known for greater cold work. A different martensitic stainless steel is also used to study the effects of intermittent stress relieving during erosion without any mechanical surface treatments. In this case, the influence of hardening exclusively from the droplet impacts is studied.

2.4. Deep rolling surface treatment

Deep Rolling (DR) is a mechanical surface treatment for metals which improves its mechanical properties by cold working such as compressive stress generation and smoothing the surface [73]. This process is sometimes also called ball burnishing because they are only different in their application. Low Plasticity Burnishing (LPB) is a similar process, which is relatively new, and serves the same purpose as DR but with a lower level of cold working [74]. The DR tool has a tungsten-carbide ball which is allowed to rotate freely in all directions within the insert upon which hydrostatic pressure is applied [75]. Hydrostatic pressure is applied by means of hydraulic fluid, which also acts as a lubricant. The tool is held in place like any other tool on a lathe machine or CNC and the pressure is applied onto the target surface only through the ball; as the feed motion is applied, it covers the entire surface to be treated. A typical DR tool is shown in the Figure 2.13.

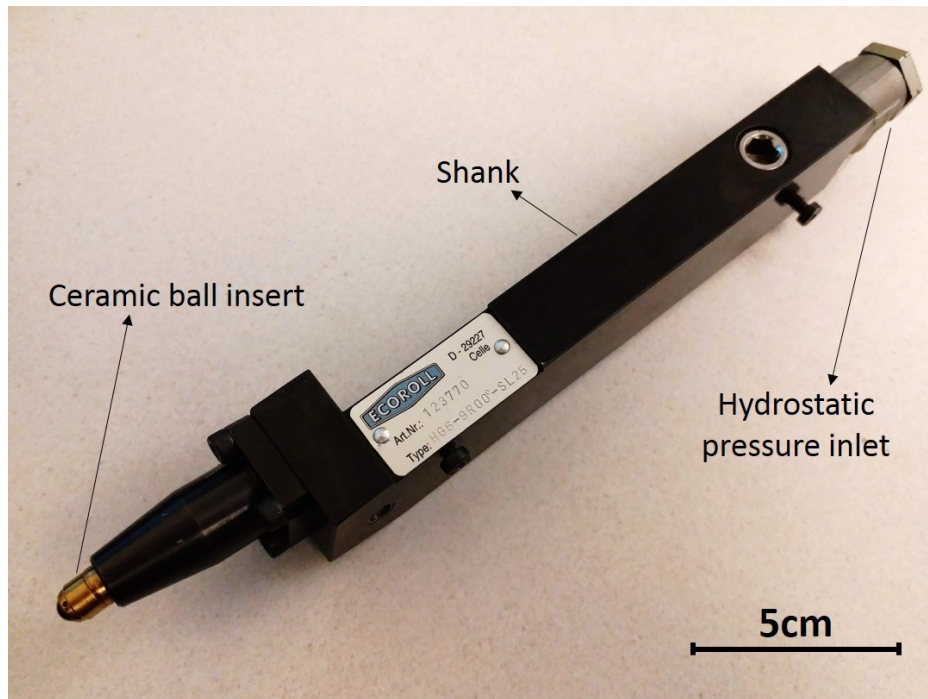


Figure 2.13 Deep rolling tool Ecoroll HG6-9R00-SL25.

Cold working treatments are known to improve fatigue, corrosion and surface properties. DR improves fatigue properties mainly due to a great depth of work hardening and due to the formation of a compressive stress field which would resist crack formation and growth [76]. A nanocrystalline region at the DR treated surface was seen in various materials [76]–[79]. This refined microstructure, due to work hardening during DR, inhibits crack initiation and hence the improved fatigue life [79], [80]. It is because of this greater depth of material that influenced the decision to use the DR treatment in this research. The DR treatment is also known to give a greater magnitude of CRS and better surface finish compared to other surface treatments like LSP, as shown in Figure 2.14, or Shot Peening (SP) [76], [78], [80]. The DR treatment was previously used to characterize Ti-6Al-4V for erosion in the literature [41].

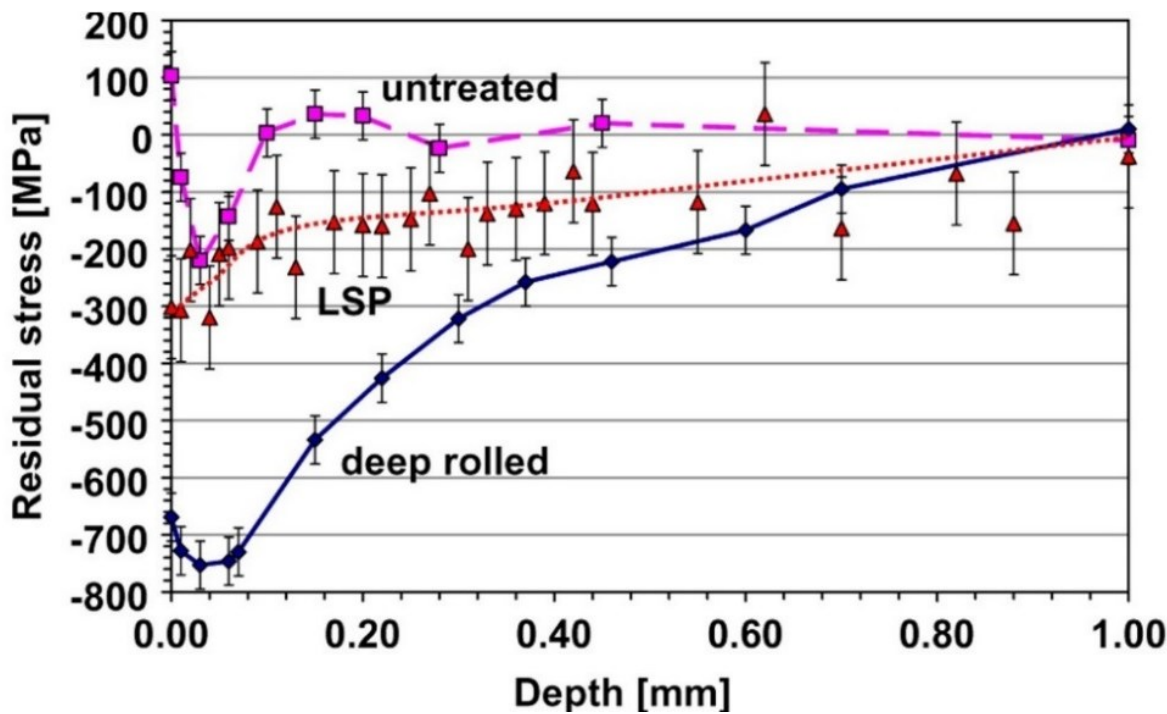


Figure 2.14 Residual stresses due to DR and LSP treatments [78].

Deep rolling parameters:

The DR equipment allows various parameters to be controlled independently. The resultant hardening, CRS, and surface finish achieved using DR treatment are dependent on the material and various process parameters such as pressure, speed, feed rate, number of passes, etc.

Pressure, sometimes also called deep rolling force, is the most discussed parameter in the literature. Greater pressure ensures greater depth and magnitude of CRS [81], [82] along with lower feed rate [81]. Increase in pressure has shown an increase in surface hardness and surface roughness in AISI 1060 steel [83]. Pressure, feed rate and number of passes were together found to be the most influential parameters in increasing the surface micro-hardness of the Ti-6Al-4V alloy [41]. Zhang [82] characterized 17-4 PH stainless steel by varying burnishing parameters and found that a greater pressure and feed rate increased the surface roughness of a cylindrical surface. Also, increase in burnishing pressure caused a marginal increase in Rockwell hardness of the same material [82]. The number of passes had very little effect on surface roughness in AISI 1060 steel [83] but in contrast, had the greatest effect on surface roughness of AISI 4140 steel [84] likely due to deformation of the soft ferritic matrix of duplex AISI 4140 steel. The ball material and lubricant have been found to be the least effective parameters on the surface response of the 4140 steel for both DR and LPB treatments [84], and are hence not considered in this work.

2.5. Suitable material

The motivation behind this research is to understand the WDE response to a potential surface treatment which could prolong the erosion life of blade materials. In the process of

studying surface treatments to address WDE problem, it was found in the literature that surfaces treated with DR and other similar processes did not respond well in the WDE environment even though it is known to improve the fatigue life through enhancing the surface properties of the components. The failure of the DR treatment in improving erosion performance was attributed to surface embrittlement due to hardening [41]. To verify the hypothesis that the failure is actually due to embrittlement from strain hardening, a material, which has a low strain hardening tendency, has to be tested for erosion by applying significant cold working treatment such as a DR treatment. The strain hardening exponent (n) is a parameter that shows the material's ability to be hardened when it undergoes some plastic deformation. Therefore, a material with suitable mechanical properties to gas turbine applications and low ' n ' value becomes a natural choice to test the hypothesis.

In the literature, alloys such as 4340 steel [85]–[87], 17-4 PH stainless steel [85], [86], [88], 17-7 PH stainless steel [86], various Copper-Beryllium alloys [87], [89], [90], and a few Aluminum or Zinc alloys [87], [91] are found to have very low n -values. The n -values of 17-4 PH and 17-7 PH stainless steels in their solution annealed and various aged conditions were reported to be as low as 0.01 to 0.05. Various Copper-Beryllium alloys such as Alloy 25, Alloy 190, Alloy 172, etc. have n -values ranging from 0.02 to 0.17. Alloys such as 17-4 PH, 17-7 PH stainless steels and Copper-Beryllium alloys offer versatility by being precipitation hardenable and are hence preferable. Additionally, these alloys will provide an opportunity to study the differences between hardening through precipitation and hardening through cold work. Precipitation hardening (also called aging) is a heat treatment where different mechanical properties can be obtained while keeping the composition unchanged. Having the same composition in various aged conditions ensures similar elastic properties; the difference is

observed only in their plastic properties. Among the discussed precipitation hardenable alloys with low n-value, Copper-Beryllium alloys are not considered in this work because they are not used in the applications encountering WDE. On the other hand, 17-4 PH and 17-7 PH stainless steels are used in aircraft and gas turbine applications [92]–[94] where WDE is a serious problem. Owing to a simpler heat treatment procedure for the aging of 17-4 PH stainless steel compared to that of 17-7 PH stainless steel [95], 17-4 PH steel can be chosen for experiments to study the effects of strain hardening on erosion behavior of DR treated samples.

The variations in mechanical properties of 17-4 PH stainless steel from aging are due to the formation of copper rich precipitates (CRP), which are of the order of a few dozen nanometers, within the laths of martensitic matrix [96]–[101]. The standard temperatures and procedures for solution treatment, the precipitation hardening treatments of 17-4 PH, and other heat resisting steels are described in the ASTM A693 standard [95]. Solution treatment is performed by heating the alloy to 1050°C followed by rapid cooling which creates a homogenous solid solution with fully dissolved copper; no trace of precipitates is found after this treatment [96]–[99]. Aging treatments for this material are carried out at temperatures ranging from 470 to 625°C followed by air cooling. At these elevated temperatures, copper atoms tend to cluster and form coherent precipitates of various sizes depending on aging temperature and aging time resulting in varied mechanical properties [96]–[98]. Aging at 480°C for an hour has been found to be most effective in terms of enhanced hardness of the material [96], [98]. Change in hardness with aging times at various aging temperatures can be seen in Figure 2.15 [96]. Prolonged over-ageing at 480°C has shown the formation of Cr-rich precipitates, which retains the hardness of the material, as the contribution of CRPs is lost, explaining the near constant hardness even after longer aging times at 480°C [97]. Increasing

aging temperature has shown a decrease in maximum achievable hardness which was attributed to precipitates growing in size and losing coherency with the BCC matrix [96], [98]. Interestingly, aging at temperatures greater than 580°C for over an hour makes it softer than the solution treated condition due to the formation of reverted austenite [96]–[100]. Austenite start temperature (A_s) for 17-4 PH is assumed to be close to that of the Fe-Ni binary system, i.e. 600°C, therefore austenite reversion kicks in when aged at 600°C or higher [98], [99]. The reversion of austenite favorably starts around CRPs formed during the initial stages of aging and eventually some of the copper dissolves back into growing reverted austenite [96], [98], [99]. This results in not just the change in microstructure but also the CRP content in the alloy. To eliminate the influence of any such microstructural changes, maximum aging temperature used in this work will be restricted to 550°C.

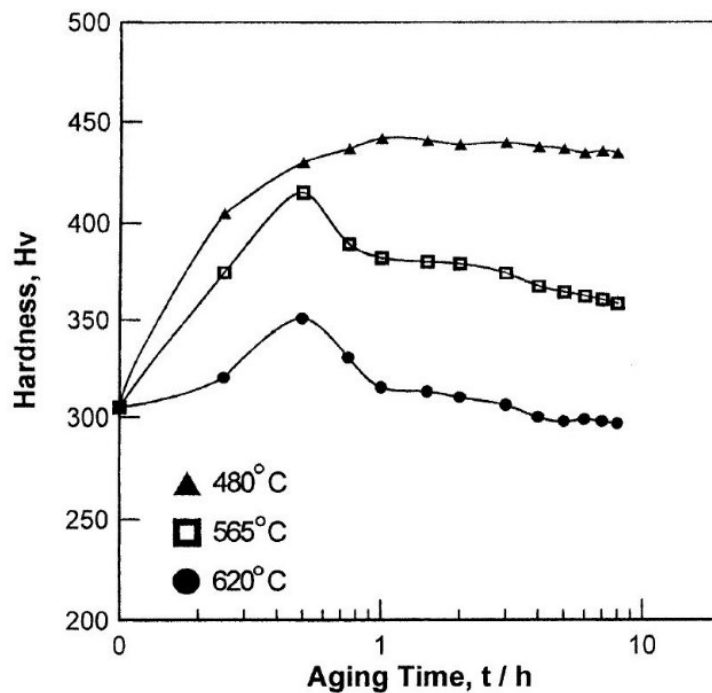


Figure 2.15 Change in hardness with aging of solution treated 17-4 PH stainless steel [96].

2.6. Objectives

The search for the best and most effective way of mitigating erosion damage in steam and gas turbines is currently on-going and significant resources have been dedicated to achieving this aim. Recently, surface treatments such as coatings and mechanical surface treatment have been explored. Moreover, most researchers are of the opinion that erosion damage is similar to fatigue damage due to the cyclic impacts. For this reason, mechanical treatments received considerable attention because they induce beneficial compressive residual stresses and work hard surface. Recent studies have shown that a combination of intermediate strain hardening and deep compressive residual stress levels are integral in mitigating erosion to a certain degree. However, only mild (or in some cases no significant) improvements were observed in the erosion performance due to the strain hardening effects of the surface treatments. This study aims to close the gap through the use of a suitable material which has a very low strain hardening exponent to evaluate its erosion performance after applying the Deep Rolling (DR) surface treatment. Specific objectives of this work include:

- Investigate the role of a strain hardening exponent and other mechanical properties on the WDE performance with and without deep rolling surface treatment.
- Study the effect of intermittent removal of strain accumulated from droplet impacts during the WDE.
- Investigate the damage mechanisms in the initial and advanced stages of treated and untreated conditions.

3. Experimental methodology

This chapter discusses in detail the methodology adopted to accomplish this research work. The chapter starts with materials selection and their suitable heat treatments, sample design and its preparation for the subsequent erosion testing. Further, various characterization techniques employed during the course of this research are also discussed in this chapter.

3.1. Material selection

Suitable materials were discussed in section 2.5 and the 17-4 PH stainless steel was chosen for the strain hardening experiments considering its low n-values and usage in WDE applications. 17-4 PH is a martensitic stainless steel having about 17% chromium, 4% nickel and 4% copper. The bulk composition of the 17-4 PH stainless steel used in this study is shown in Table 3-1. The alloy is precipitation hardenable and various properties can be achieved by means of aging treatments. The standard temperatures and procedures for solution treatment and the precipitation hardening treatments of 17-4 PH stainless steel are described in the ASTM A693 standard [95]. The as-received material is in the solution treated condition and its condition will be referred to as ‘Condition-A’. In addition to Condition-A, which is the solution treated condition, two aged conditions of 17-4 PH stainless steel are used. The H925 and H1025 conditions are achieved by aging the Condition-A for 4 hours at 495°C and 550°C respectively followed by air cooling. The H925 and H1025 conditions are chosen to avoid the austenite reversion which occurs at temperatures above 600°C.

Table 3-1 Composition of 17-4 PH stainless steel.

Element	Composition (wt. %)
C	0.038
Cr	15.35
Ni	4.22
Cu	3.4
Mn	0.98
Si	0.38
Nb	0.242
Ta	0.01
Mo	0.05
P	0.013
S	0.001
Fe	balance

Strain hardening in the erosion problem is not just from the surface treatment but also due to repeated droplet impacts as discussed in section 2.1.3. To better understand the contribution of strain hardening to WDE, it is important to study the accumulation of strain during the erosion by impacts. To study the influence of strain accumulated during water droplet impingement, intermittent strain relieving was performed and compared in a different set of erosion experiments. A different martensitic stainless steel grade X22CrMoV12-1, which is a commonly used blade material for steam turbine blades [102], is used for this purpose. 17-4 PH stainless steel cannot be strain relieved due to the activation of age-hardening at temperatures above 400°C [99], [103] and will introduce additional unknown factors. Therefore, X22CrMoV12-1 stainless steel is selected for this experiment because it has a well-established stress relieving temperature range of 660 to 690°C without the risk of activating some strengthening mechanisms or introducing some unknown factors.

Table 3-2 Typical composition of X22CrMoV12-1 stainless steel.

Element	Composition (wt. %)
C	0.18-0.24
Cr	11-12.5
Ni	0.3-0.8
Mo	0.8-1.2
V	0.25-0.35
W	max. 0.6
Nb	max. 0.05
Si	0.1-0.5
Mn	0.3-0.8
P	max. 0.035
S	max. 0.035
Fe	balance

X22CrMoV12-1 stainless steel, whose typical composition is given in Table 3-2, is used for studying accumulated strain during the WDE process. It is also a martensitic stainless steel tempered at about 700°C and was obtained in this condition. To ensure that the maximum accumulated strain is relieved each time, the samples were stress relieved at 680°C for 75 minutes followed by air cooling after each cycle, according to DIN 10269 standard [104].

3.2. Sample preparation

3.2.1. T-samples

17-4 PH steel samples are used for the strain hardening experiments which require some of them to be deep rolled before erosion testing. Figure 3.1 shows CAD models of the raw T-shape and the finished T-sample. The raw T-shapes are heat treated, DR treated and finally CNC machined to their finished shape as described by the flowchart shown in Figure 3.2. To measure the tensile properties at each aged condition, a few tensile dog-bone samples are aged

together with the discs and raw T-shapes (all of which were initially in the solution annealed Condition-A).

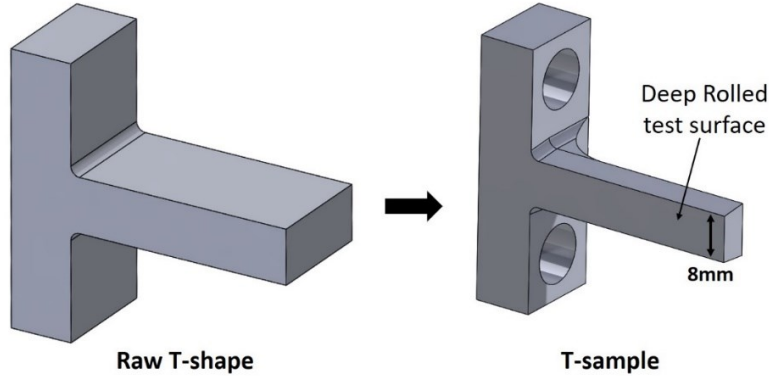


Figure 3.1 CAD models of raw T-shape and the finished T-sample.

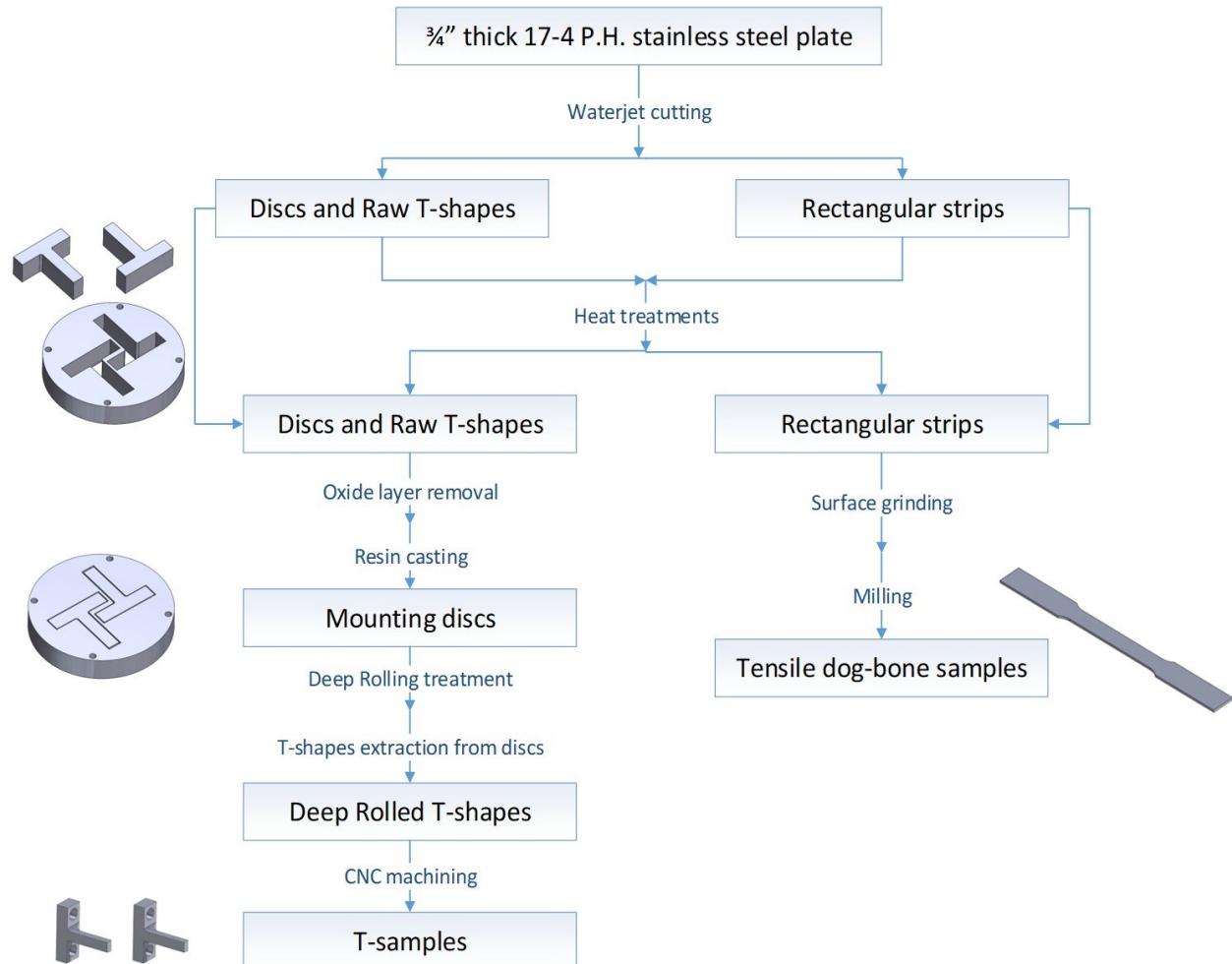


Figure 3.2 Flowchart of 17-4 PH stainless steel T-sample preparation.

To have a deep rolled surface on the finished T-samples for the erosion test, it was necessary to perform the DR treatment on the raw T-shapes before they are machined to their final shape. As deep rolling was to be performed on a lathe machine, the erosion test surface had to be flat and be part of a disc. This study is limited to normal impacts from water droplets and requires the flat impact surface to be 8 mm wide, meaning the erosion test surface should be part of the flat face of the disc. It was therefore decided to have a disc in which the raw T-shapes can be mounted. The mounting discs, each holding a pair of T-shapes in place, are DR treated after which the raw T-shapes treated surface is carefully extracted. These deep rolled T-shapes were ultimately CNC machined to the finished T-samples. They are designed for WDE testing in the erosion rig safely at speeds of up to 425m/s. This section further elaborates the T-sample preparation procedure from a $\frac{3}{4}$ inch thick 17-4 PH stainless steel plate.

Waterjet machining was employed to efficiently cut the discs and the raw T-shapes from within the discs, without having to waste material by traditional machining. It is to be noted that the sole purpose of the discs is to allow deep rolling on the T-samples by mounting raw T-shapes in the discs. As mentioned, a waterjet was employed to cut a $\frac{3}{4}$ inch thick plate to obtain discs, raw T-shapes and rectangular strips ensuring minimum material wastage from machining. Each disc is $\frac{3}{4}$ inch thick and 105 mm in diameter and has two raw T-shapes cut out from it as shown by a CAD model in Figure 3.3. Eight such discs and their respective sixteen raw T-shapes were cut from the plate. Rectangular strips of about 3mm thickness and $\frac{3}{4}$ inch wide were also cut using a waterjet cutter to be further machined to tensile dog-bone specimens. Each strip was reduced to a uniform thickness of 2mm by surface grinding to avoid any distortion in the samples due to machining stresses. The 2mm strips were milled to dog-

bone shape based on ASTM E8/E8M standard [105]. A picture of a tensile dog-bone specimen can be seen in Figure 3.4.

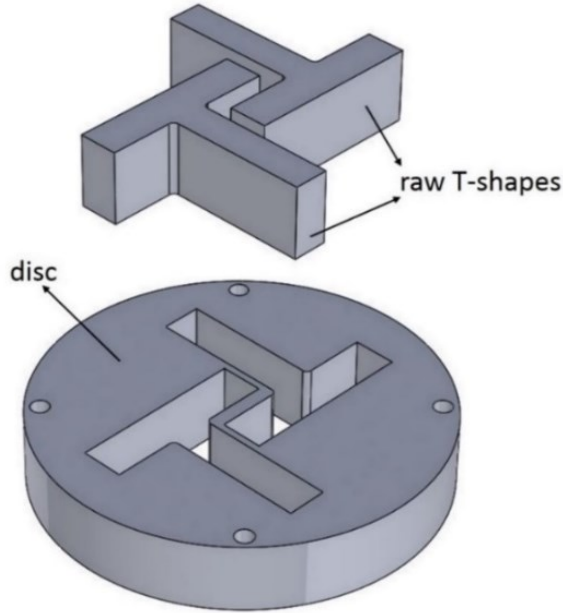


Figure 3.3 CAD model of a disc and two raw T-shapes after waterjet cutting.

Some of the T-samples in solution treated Condition-A have to be heat treated to aged H925 and H1025 conditions. A 3.5kW power rated Lindberg/Blue-M box furnace, having a maximum temperature range of 1100°C, was used for this purpose. Discs, raw T-shapes and tensile dog-bone samples were aged together in the furnace to obtain uniform properties in each of the samples. As per ASTM A693 standard [95], the furnace was maintained at 496°C and 550°C for four hours each to achieve H925 and H1025 conditions respectively. Following the four hours of aging at their respective temperatures, the samples were removed from the furnace and air cooled to room temperature. The heat treatment formed an oxide layer on the surface which had to be removed before the DR process. 240 grit grinding paper was employed to remove this layer from each sample.

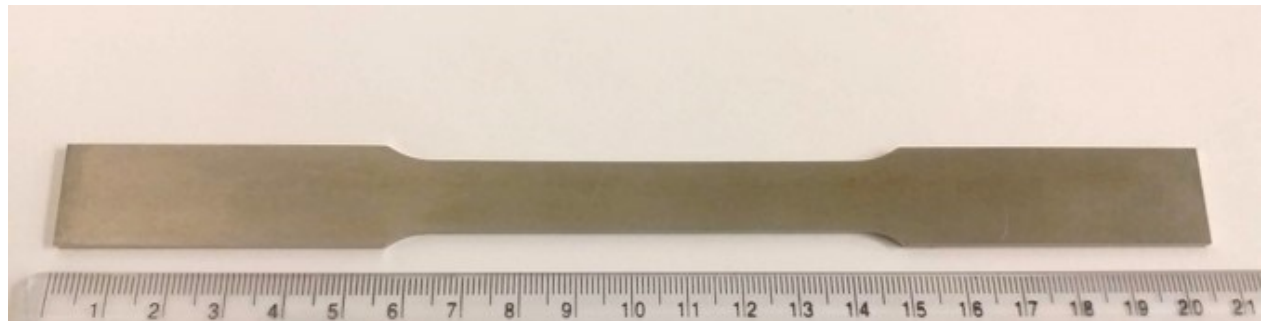


Figure 3.4 Tensile dog-bone specimen.

After the raw T-shapes were cleaned, they were assembled back into the discs from which they were cut. Waterjet machining leaves a visible kerf space of about a millimeter wide along the cutting path as portrayed in Figure 3.5. This kerf space allows the raw T-shapes to slightly displace within the disc. In order to have an efficient deep rolling treatment, it is important for the samples to be fixed, sitting flush and have a flat top surface.

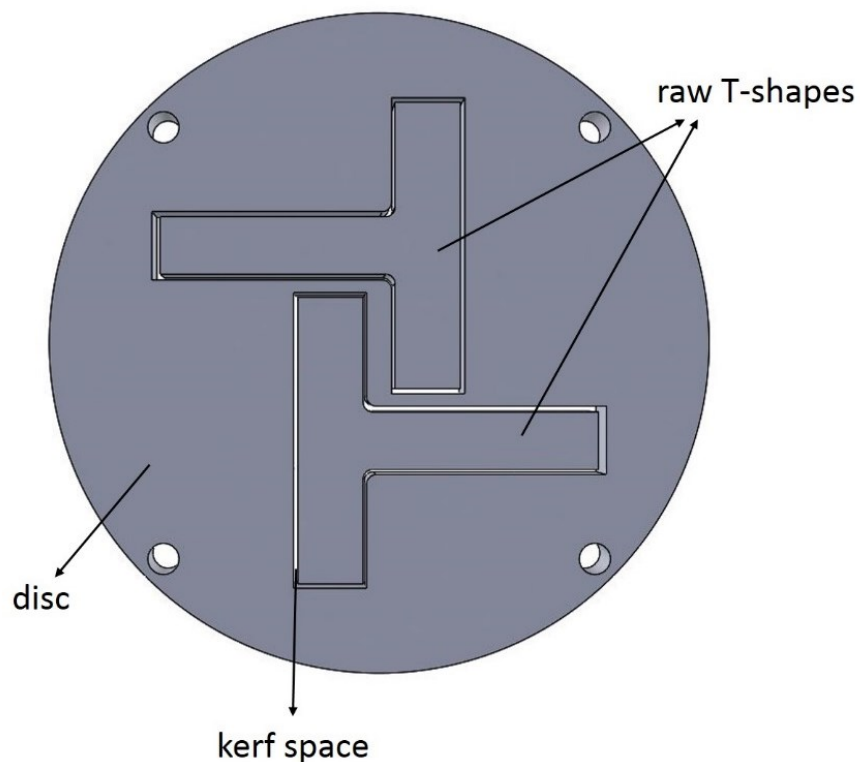


Figure 3.5 CAD model top-view of raw T-shapes assembled in a disc.

The kerf space was filled to the brim with epoxy resin and cured for 24 hours. Popsicle spacers were used to maintain uniform spacing around the gap. Resin casting, when cured, makes the mounting disc assembly complete and ready to be deep rolled as can be seen in Figure 3.6.



Figure 3.6 A resin casted mounting disc.

The deep rolling was performed on a King-Industrial KC-1440ML engine lathe machine using a deep rolling setup from Ecoroll as seen in Figure 3.7. The Ecoroll deep rolling setup comprised of an oil reservoir mounted with a primary low-pressure pump which feeds oil to a secondary high-pressure pump. This secondary pump inputs hydrostatic pressure to a HG6-9R00-SL25 deep rolling tool, shown in Figure 2.13. This hydrostatic tool, which has a 6mm diameter ceramic ball insert, was held and secured in the tool holder of lathe machine by its shank.



Figure 3.7 Deep rolling setup.

The mounting discs were reinforced by a backing disc (from behind) as an additional support for the raw T-shapes mounted in the discs during deep rolling. Backing and mounting discs were held in place by four bolts through them along the circumference. This arrangement of discs was held in the lathe chuck and pressure was supplied to hydrostatic tool by switching on the two pumps as can be seen in Figure 3.8. After the high-pressure pump was adjusted to a set pressure, the tool was brought in contact with the disc at a starting position. Longitudinal motion of the tool setup was restrained, and only the cross feed was allowed. Cross feed towards the center of the disc was activated to achieve a single pass of deep rolled surface on the mounted disc as the tool moves. Figure 3.8 shows a counterclockwise rotating mounting disc being deep rolled on a lathe machine. This procedure is repeated to achieve multiple passes.

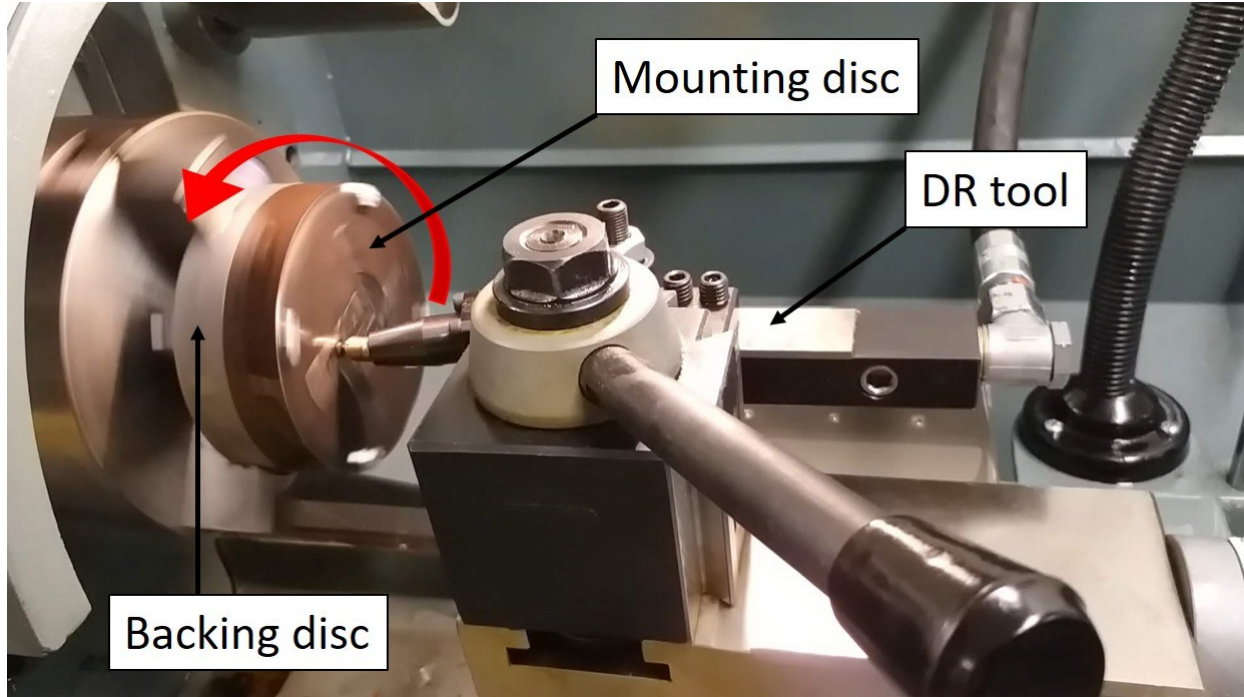


Figure 3.8 Deep rolling a mounting disc on lathe machine.

Deep rolling parameters from the literature were briefly discussed in section 2.4 and the optimum spindle speed, feed rate and number of passes was chosen based on that discussion. It is usually desirable to have a greater magnitude and depth of compressive residual stress (CRS) to achieve better mechanical properties. A lower feed rate of 0.0356mm/rev was chosen because a lower feed rate was found to give a better CRS and surface finish [81], [82]. At these conditions, the lower spindle speed has a better residual stress profile [82]. With all else the same, a greater number of passes have been found to result in more uniform residual stress profile along the depth [81], [84], and hence 3 passes were applied. Pressure is the most important and influential parameter [81]–[84]; Therefore both 100 and 200 bar were applied to the T-samples in Condition-A to shortlist one of them based on WDE performance. Table 3-3 summarizes the deep rolling process parameters used for sample preparation.

Table 3-3 Deep rolling process parameters.

Spindle speed (RPM)	Feed rate (mm/rev)	No. of passes	Rolling pressure (bar)
70	0.0356	3	100 or 200

After three passes of deep rolling are done, the mounting discs and rolled surface are removed from the lathe chuck and cleaned thoroughly. A distinct rolled surface with an improved surface finish is observed and shown in Figure 3.9. The deep rolled T-shapes are carefully extracted from the mounting discs by a hydraulic press.

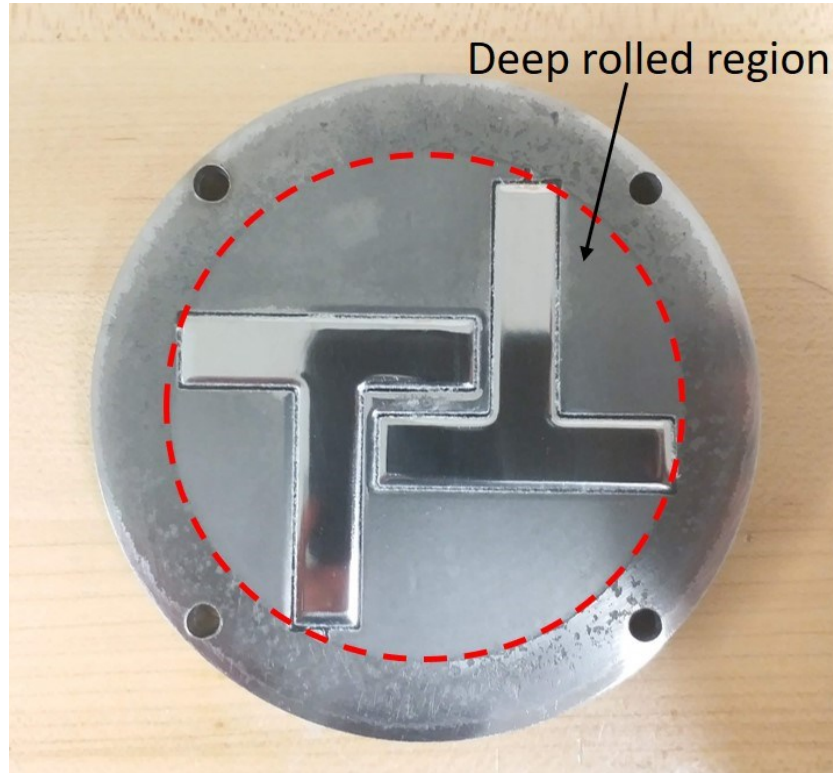


Figure 3.9 Deep rolled mounting disc.

The extracted T-shapes were CNC machined on a Maxmill QMC-1050 vertical machining center to their final shape. Finished T-samples are ready for erosion testing and can be seen in Figure 3.10. The T-samples each have an arm whose top surface is an 8mm wide

flat test surface. The base of each T-sample has two holes for bolting onto the rotating disc of the erosion test rig. These samples are designed for safe operation up to a maximum speed of 425m/s or 17,000rpm.

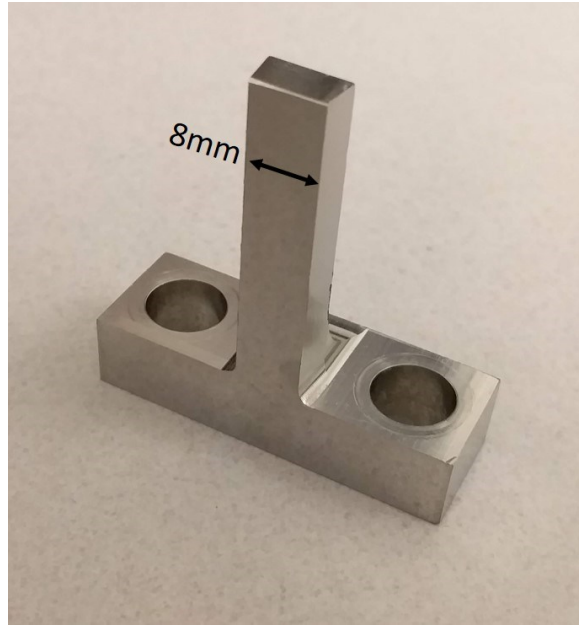


Figure 3.10 A finished T-sample.

3.2.2. Test coupons

X22CrMoV12-1 stainless steel is used to study the effects of intermittent stress relieving on the WDE behavior. As these samples do not require any surface treatment prior to their erosion testing, coupons (or inserts) were used as samples by inserting them in holders instead of using solid samples such as the T-samples. The sample holder is affixed to the rotating disc of the erosion rig and has a slot in which a coupon can be inserted and tested for erosion. Each sample holder holds a coupon in its slot which is well secured by a nut, bolt and washers. Figure 3.11 shows an exploded view of the sample holder assembly. The use of coupons saves sample machining time and is cost effective because, compared to the T-shaped samples, relatively very little material is replaced after testing is complete. The design speed of

sample holders, made of Ti-6Al-4V, is limited to 350m/s i.e. 14,000rpm on the rotating disc of erosion rig.

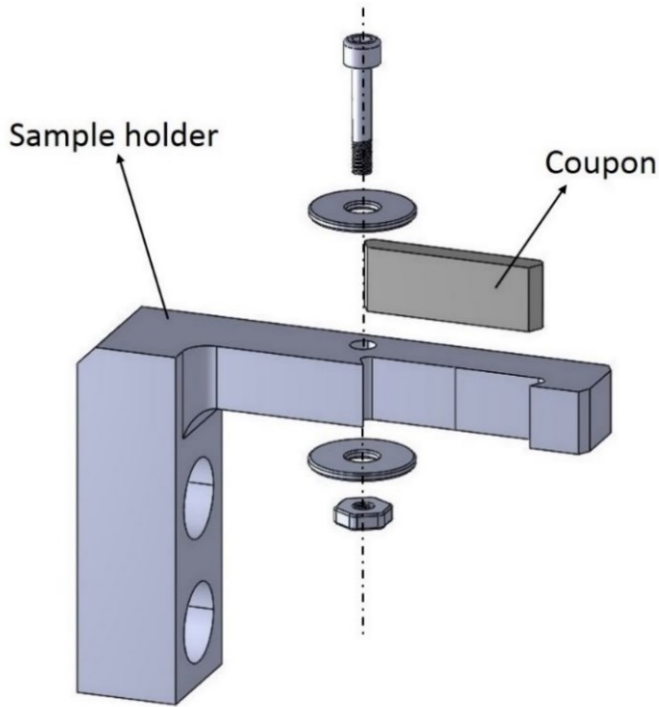


Figure 3.11 CAD model of sample holder assembly.

Strips of X22CrMoV12-1 were roughly cut by waterjet and were brought to uniform thickness of 3.5mm by surface grinding them. These strips were cut to smaller pieces and later ground, with 320 grit silicon-carbide paper, to assure the shape of the coupons had a snug fit within the sample holders. After the coupons have assumed the final shape, the test surface of the coupons was progressively ground and finished to a 1200grit silicon-carbide finish. The coupons can now be tested for erosion performance by fixing them into the sample holders. Coupons for 17-4 PH stainless steel in Condition-A, H925 and H1025 have also been prepared in this way to be tested for erosion in the ground condition without any surface treatments. These coupons will be used to check the erosion performance in each condition with ground surface finish and no prior strain from the DR treatment.

3.3. Characterization

Various characterization techniques were employed during this research to obtain tensile properties, hardness, surface roughness and erosion performance of the studied materials. A Scanning Electron Microscope (SEM) was also used to identify the erosion mechanisms of the eroded test samples by examining the eroded surface of the samples. This section describes the equipment used and procedures followed to characterize the various samples used throughout this research.

3.3.1. Erosion testing

The water droplet erosion tests were carried out on a custom erosion test rig at Concordia University. This erosion rig is composed of an 18-inch rotating disc, which has provision for mounting samples on it, which rotates at specific set speeds. The water droplet generating system then introduces water droplets across the front of the samples to simulate erosion conditions in accordance with the ASTM G73 standard, [25].

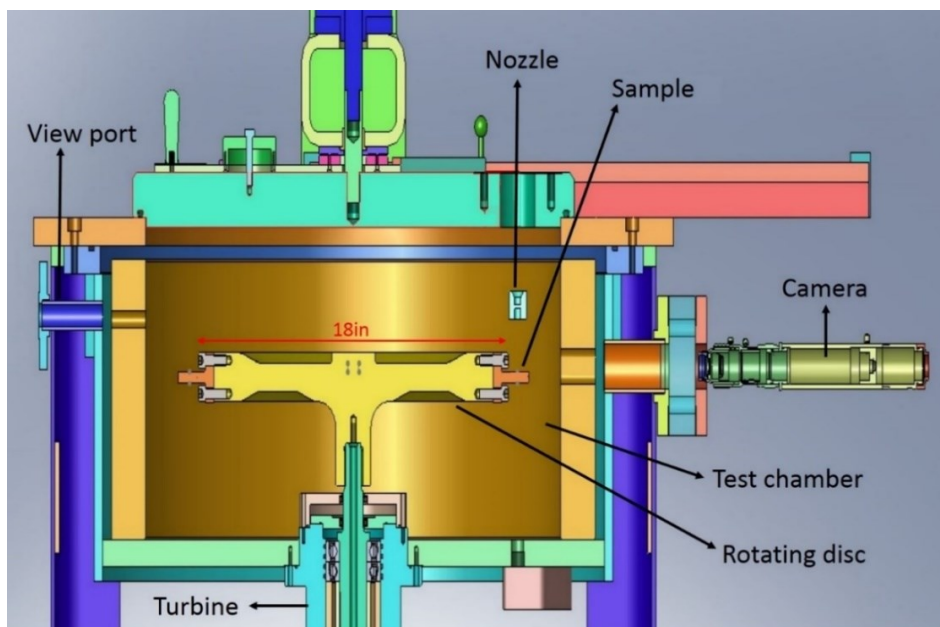


Figure 3.12 Schematic of water droplet erosion rig.

The water droplet erosion rig, as shown by the schematic in Figure 3.12, is controlled by a computer program. It allows erosion testing by constantly monitoring various operating parameters such as test chamber pressure, chamber temperature, bearing temperature, vibration level, etc. and by controlling various solenoid valves which allow chamber evacuation, draining of water, etc. This rig permits rotational speeds of up to 20,000rpm which corresponds to a linear impact speed of 500m/s on the test section of the samples. It has a test chamber that can be evacuated to 30-50mbar vacuum pressure during tests to minimize the air friction that can cause an eventual rise in temperatures of the rotating disc and bearings during erosion tests. Each sample is paired and tested against a reference sample to maintain balance and to limit vibration levels of the rotating disc. The test and reference samples are mounted diametrically opposite on a disc that is driven by a turbine powered by 100psi compressed air. When the disc reaches the desired set speed, water droplets are introduced for a set duration via a valve and using a nozzle positioned over the samples in the chamber. The samples experience normal droplet impacts only during the test duration. As the test time ends, the water supplied to the nozzle is stopped and the rotating disc is gradually brought to rest by decelerating the turbine with compressed air. The water accumulated during the erosion test in the chamber is constantly drained to a scavenge tank beneath the chamber. The test chamber is pressurized to atmospheric pressure before the samples are removed from the disc. Finally, the samples are removed and cleaned thoroughly. This ends a single cycle of erosion testing on a pair of samples; multiple such cycles constitute a single erosion test. The erosion test is periodically interrupted to track the erosion mass loss as it progresses with time. Samples are weighed after every cycle of testing on a sensitive balance, which is accurate up to 0.2 mg, to measure the

eroded mass. Mass loss and cycle time are used to plot the erosion curves, as in Figure 2.1. In the case of strain relieving studies, the test sample was relieved at the end of every cycle.

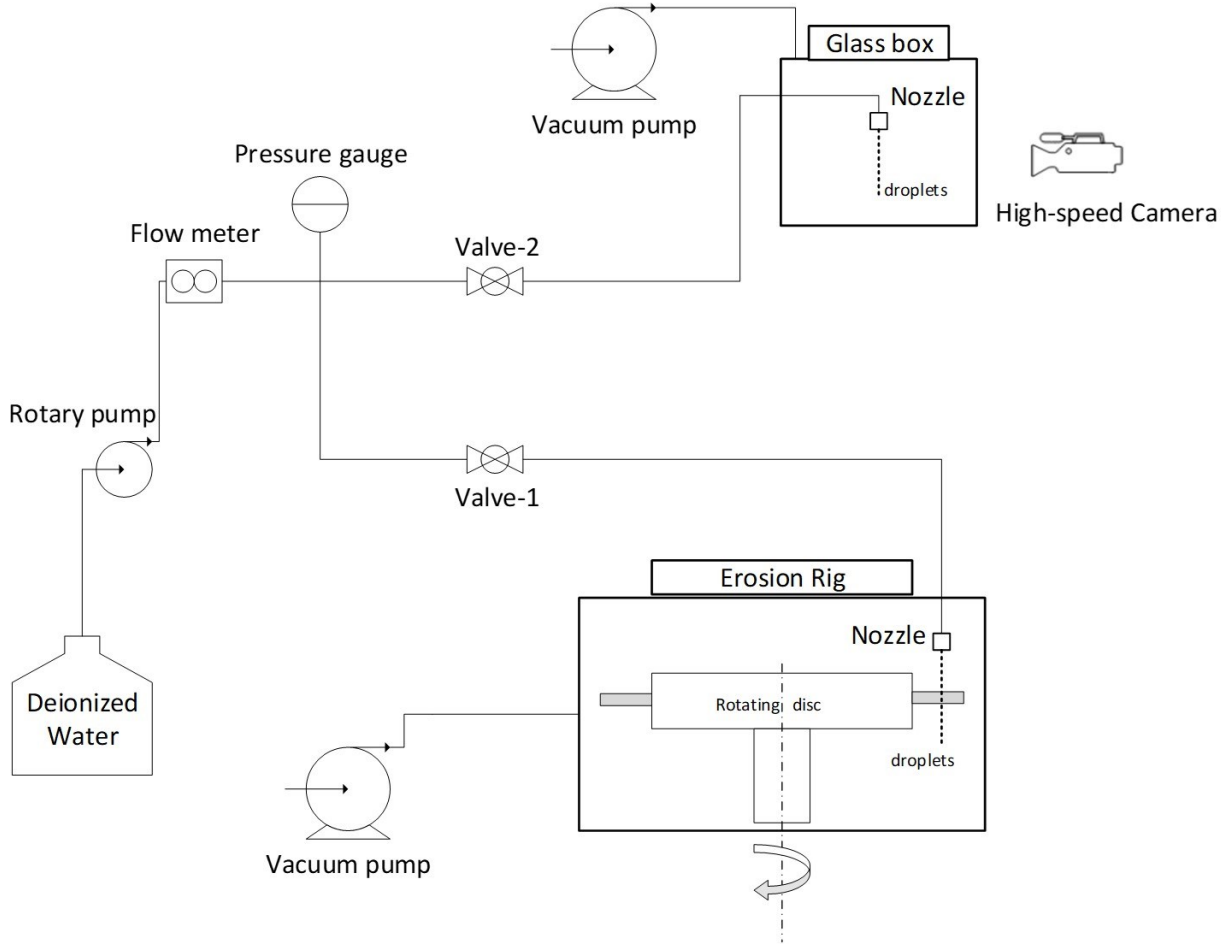


Figure 3.13 Schematic of water droplet generation system.

The water droplet generating system, used to introduce droplets in this rig, consists of a rotary pump that pumps deionized water from a reservoir to the nozzles in the erosion rig or to a glass box having the same pressure as the rig as shown in Figure 3.13. Valves 1 and 2 are used to control the supply of water to the erosion rig and the glass box respectively. Only one valve is opened at any given time, while the other one is fully closed. The water passes through a flowmeter, pressure gauge and valves 1 or 2 before it reaches either nozzle. The water line pressure, indicated by the pressure gauge before the start of test (i.e. when the valves are

closed), was maintained at 30psi. As the valve is opened for the duration of tests, the pressure drops to about 1psi and a flowrate of 0.05liters/min is maintained to obtain droplet size of 460 μm . This was established, with the use of a high-speed camera (9000fps) and the glass box set up, solely for the characterization of the droplet size distribution and the number of droplets. A nozzle with an orifice diameter of 400 μm was used to obtain approximately 460 μm diameter droplets. As the deionized water exits the nozzle and enters the chamber or the glass box, it starts to form droplets of water due to flow separation. At vacuum pressures of 30-50 mbar and at a standoff distance of 50 mm from the nozzle, droplets are formed at an average size of 464 μm and nearly 6 droplets exist over the 8 mm width at any given time [41], [46], [50], [58]. The droplet size distribution derived from the 400 μm orifice diameter nozzle is shown in Figure 3.14.

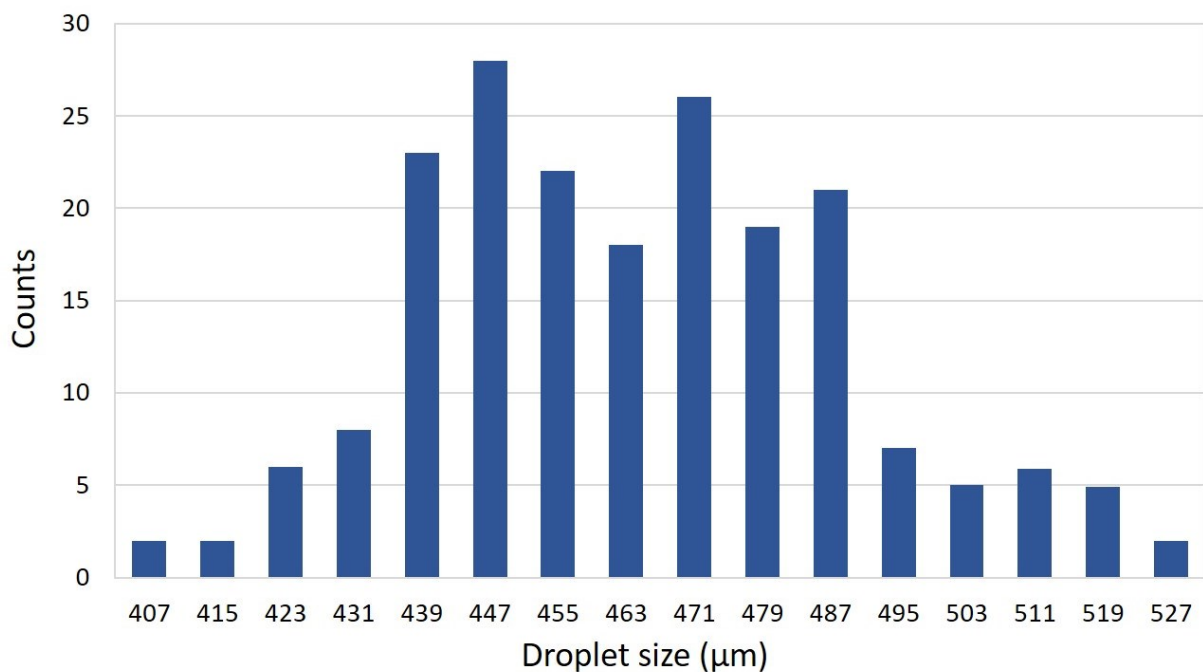


Figure 3.14 Droplet size distribution of a 400 μm nozzle.

The erosion test parameters such as test speeds, droplet size, number of droplets and impact angle along with various test conditions for the droplet generation such as water line pressure, flow rate and test chamber pressure used in this work are summarized in Table 3-4.

Table 3-4 Erosion test parameters and conditions used.

Parameters	Variants
Linear impact speed (m/s)	250, 300
Average droplet size (μm)	464
Impact angle ($^{\circ}$)	90
Test chamber pressure (mbar)	30-50
Initial waterline pressure (psi)	30
Waterline pressure during test (psi)	1
Flow rate (liters/min)	0.05

3.3.2. Tensile testing

Tensile tests were performed on 17-4 PH stainless steel samples in the solution treated Condition-A as well as in the aged H925 and H1025 conditions to obtain their yield strength, ultimate strength, percentage elongation and strain hardening exponent. The tensile tests were carried out as per the ASTM E8/E8M standard [105] on an Instron-3382 universal testing machine. Each tensile dog-bone sample, seen in Figure 3.4, was affixed in a jaw fixture between crossheads. An Instron extensometer of 50 mm gauge length was mounted on the sample to measure the displacement during each test as shown in Figure 3.15. The samples were pulled at a crosshead speed of 1mm/minute amounting to a strain rate of about 0.003/minute based on the extensometer. Tensile load, machine displacement and extensometer displacement values were constantly recorded by a computer and were later analyzed to

calculate the tensile properties. Two samples were tested at each condition to check for the repeatability.

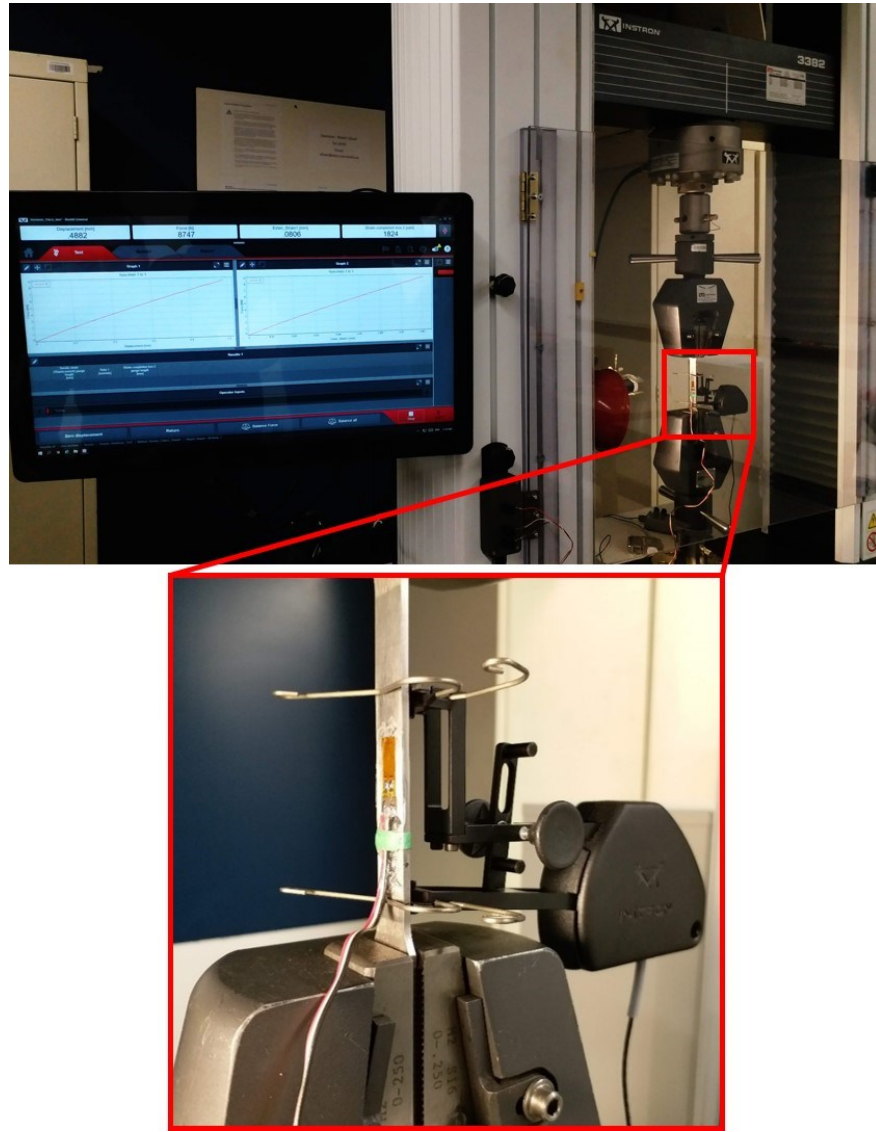


Figure 3.15 Tensile testing of dog-bone sample on Instron-3382 machine.

A 50 mm gauge length was marked on the thin side of the tensile samples prior to testing. The readings for the width and thickness were measured 3 times each (to find an average) within the marked gauge length of each sample. The average width and average thickness were utilized to obtain the average cross-sectional area which was used to calculate the engineering stresses. 0.2% yield and tensile strength were obtained from engineering stress

versus engineering strain graphs. Resilience is calculated by measuring the area under the elastic region of the engineering stress versus engineering strain curves, shown by the highlighted region in Figure 3.16. The material fractures with further strain as seen in Figure 3.16. Engineering stresses and strains were used to calculate the true stresses and true strains using equations 9 and 10 [85], [86].

$$\sigma_T = \sigma_E(1 + \varepsilon_E) \quad \dots \dots \dots (9)$$

$$\varepsilon_T = \ln(1 + \varepsilon_E) \quad \dots \dots \dots (10)$$

Equation-11 gives the relation between true stress and the true strain within the plastic region where strength coefficient ‘K’ and strain hardening exponent ‘n’ are material dependent constants [85], [86]. A log-True stress versus log-True strain is plotted for the plastic region and its slope gives the strain hardening exponent ‘n’.

$$\sigma_T = K\varepsilon_T^n \quad \dots \dots \dots (11)$$

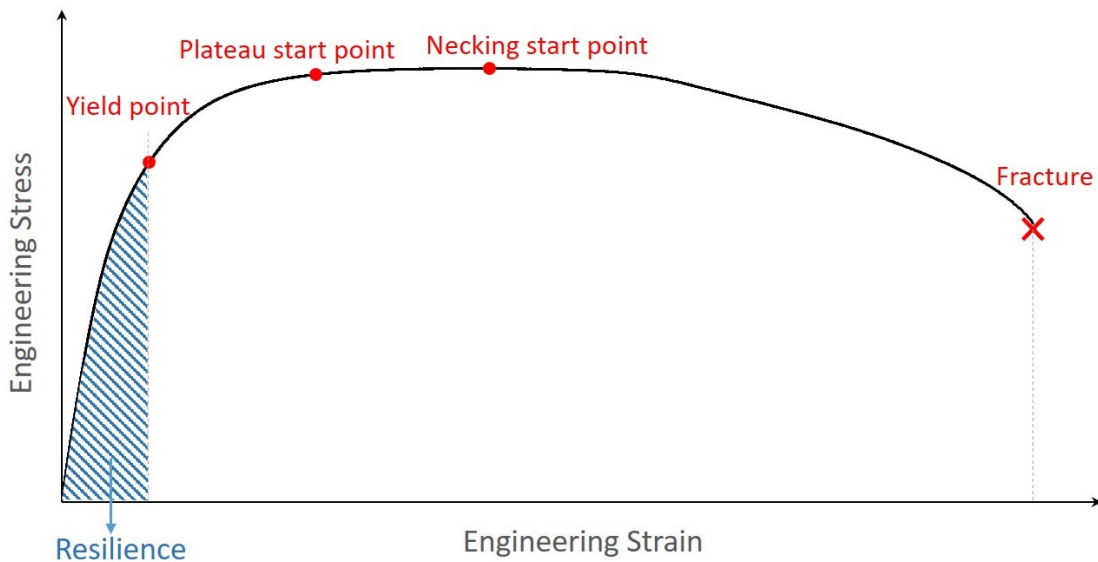


Figure 3.16 Illustration of resilience and critical points on tensile stress-strain curve.

3.3.3. Hardness testing

Rockwell hardness and Vickers micro-hardness were measured during this study. The Rockwell hardness of 17-4 PH stainless steel samples in each condition were measured using a Wilson Rockwell hardness testing machine on a C-scale, which uses a spherconical diamond indenter and 150kgf load. The Rockwell hardness was only used to verify if the proper aged condition was achieved for the raw T-shapes and tensile dog-bone samples.

The Vickers micro-hardness was measured for both 17-4 PH and X22CrMoV12-1 stainless steel samples. A Mitutoyo MVK-H1 micro-hardness testing machine, as seen in Figure 3.17, was used with 300gf and 500gf loads for the X22CrMoV12-1 and 17-4 PH stainless steels respectively. The load was applied for a dwell duration of 15 seconds in each case. The surface micro-hardness of 17-4 PH stainless steel T-samples was measured on both the polished surface and the deep rolled surface. The deep rolled surface of each T-sample was prepared by three rolling passes while the polished surface was achieved by grinding to a 1200 grit finish. Measurements from both surfaces will help check for an increase in hardness with the DR treatment. An average of ten readings is taken for each sample.



Figure 3.17 Mitutoyo MVK-H1 micro-hardness testing machine.

3.3.4. Laser scanning confocal microscopy

An Olympus LEXT OLS4100 laser scanning digital microscope is used for the surface roughness measurements as well as for the microstructure examination of the sectioned 17-4 PH samples. This microscope having a resolution of 10 nanometers was used to measure the line roughness of the DR and polished surfaces of erosion test samples. A $1225\mu\text{m} \times 1225\mu\text{m}$ area, which is representative of the sample surface prior to erosion testing, was selected and 20 lines were randomly selected from within the area. For each sample average line roughness (R_a), measurements were taken at each line and an average of them is calculated.

The microstructure of the sectioned erosion test samples was also observed. An erosion test sample in each condition was sectioned, mounted and polished before etching with Fry's reagent for 13 seconds. This allowed for imaging of the microstructural features in the samples at each aged condition.

3.3.5. Scanning electron microscopy

A Hitachi S-3400N SEM was used to examine craters and pits of the erosion test samples. Secondary Electrons (SE) were used for studying crater surface imaging and Back Scattered Electrons (BSE) was utilized to observe the microstructure in sectioned samples. The evolution mechanism of pits and craters during erosion in X22CrMoV12-1 steel was studied by imaging pits at different stages of their growth. Cross-section imaging of 17-4 PH stainless steel samples was also done to study the influence of microstructure on crack propagation and WDE behavior.

4. Results and Discussions

Materials suitable for the study are selected based on the discussion in section 2.5. Samples were fabricated using the selected materials and characterized for their properties and WDE performance. A set of WDE experiments have each been designed: to evaluate the influence of strain hardening caused by the DR treatment; and to evaluate the effect of intermittent strain relieving during WDE.

Parameters such as microstructure, surface roughness, tensile properties and microhardness are obtained prior to evaluating the WDE behavior of the 17-4 PH steel samples for the strain hardening experiments. The WDE behavior is discussed in the purview of ascertained properties and micrographs of erosion samples.

The strain relieving experiments were conducted on the X22CrMoV12-1 steel with varying frequency of intermittent strain relieving of the test samples. The qualitative differences observed were explained using the micrographs taken at various intervals along the WDE test.

4.1. Microstructure of 17-4 PH stainless steel

The microstructure of the DR treated 17-4 PH stainless steel in various conditions was examined by polishing and etching the sectioned samples in Fry's reagent. Figure 4.1, Figure 4.2 and Figure 4.3 show the cross-section SEM micrographs of the DR treated samples in the solution annealed Condition-A, H925 and H1025 conditions respectively. All the three conditions have equiaxed martensitic grains of about $30\mu\text{m}$ and the sporadic presence of δ -ferrite stringers is also observed away from the sample surface, as shown in Figure 4.4 . The martensite packet boundaries are not clearly visible in Condition-A but the contrast is improved

in the aged alloys. The prior austenite grain boundaries were visible in the aged conditions owing to improved contrast [98].

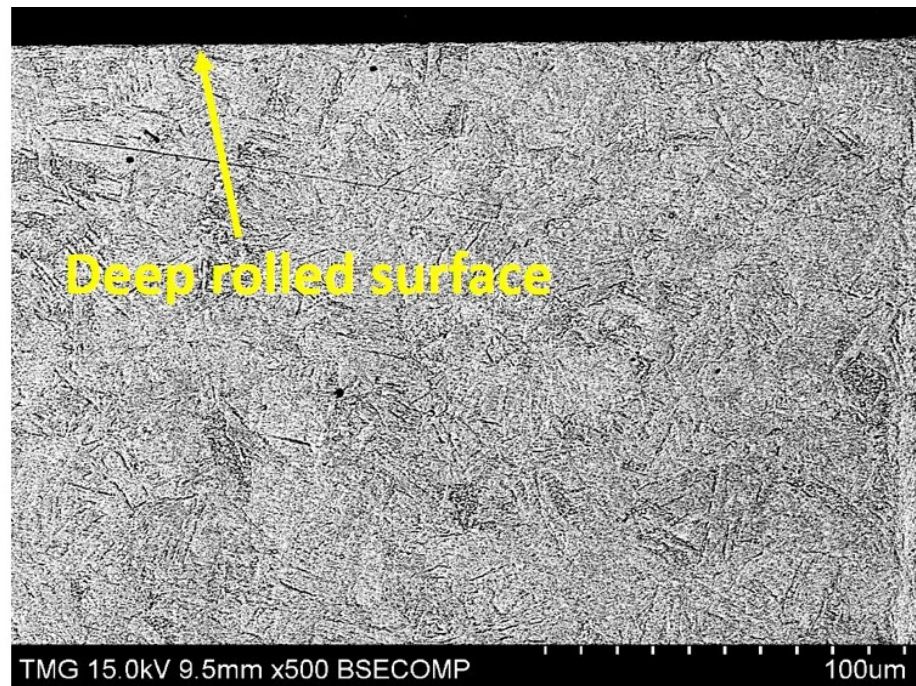


Figure 4.1 Microstructure of 17-4 P.H. steel in Condition-A.

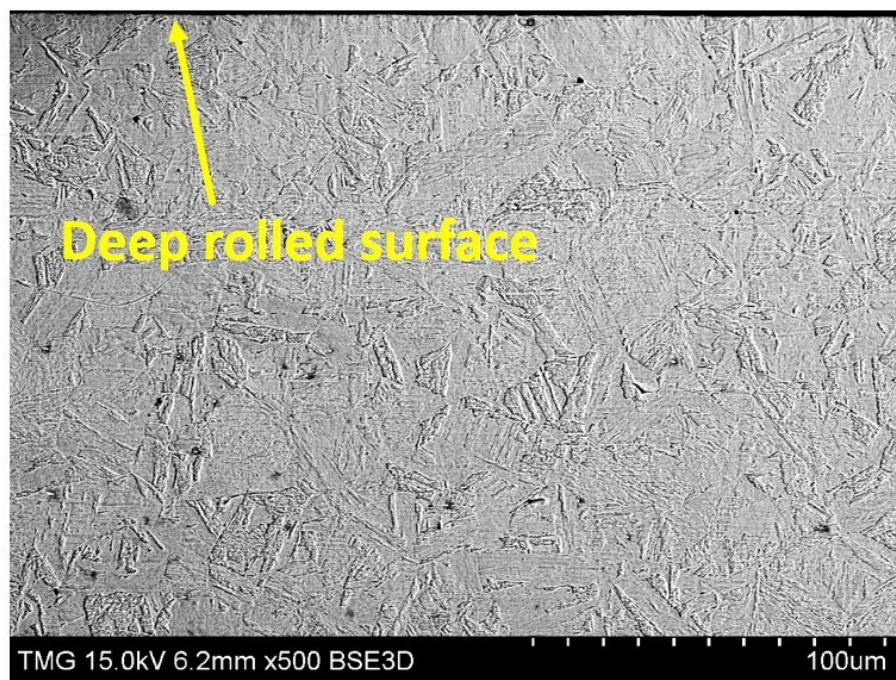


Figure 4.2 Microstructure of 17-4 PH steel in H925 condition.

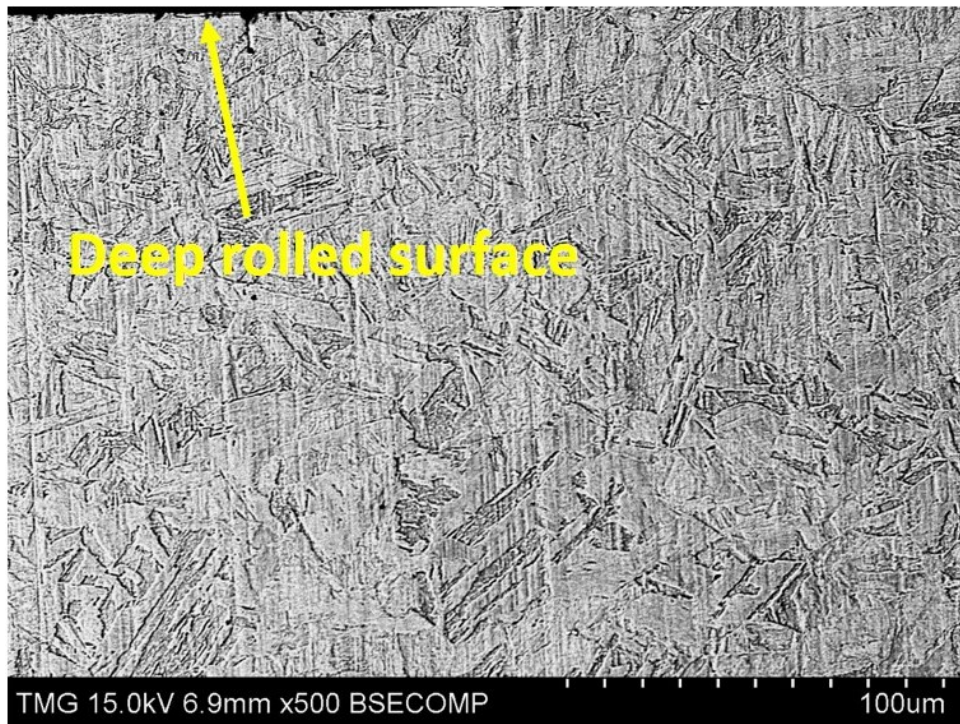


Figure 4.3 Microstructure of 17-4 PH steel in H1025 condition.

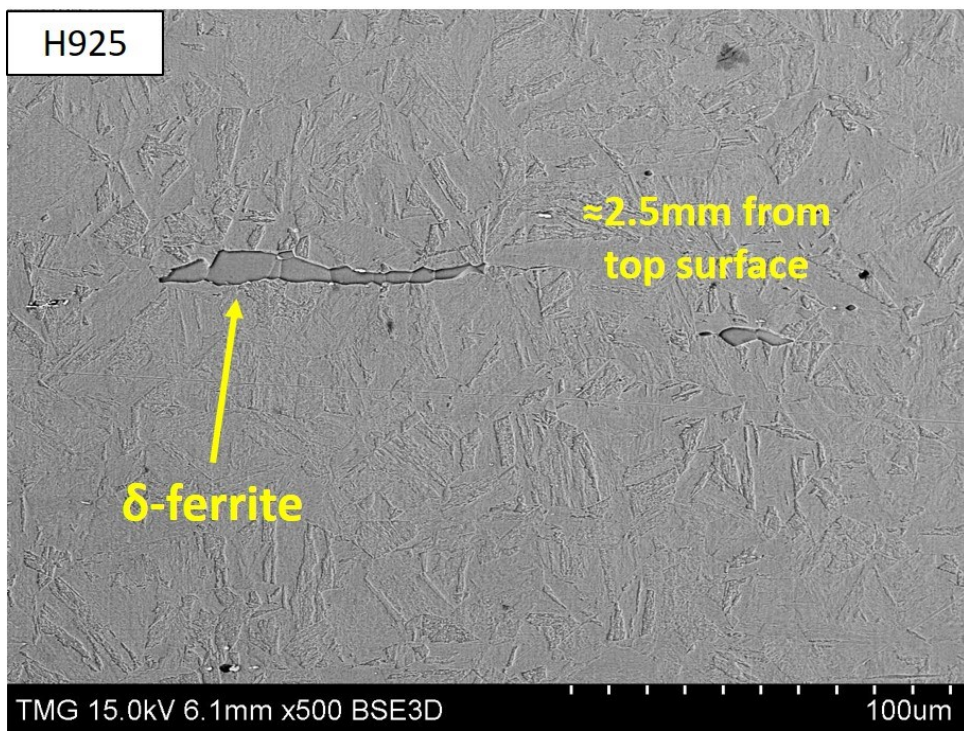


Figure 4.4 δ-ferrite in the microstructure of 17-4 PH stainless steel.

4.2. Tensile properties of 17-4 PH stainless steel

Tensile properties were obtained for the solution treated condition-A and H925, H1025 aged conditions. The raw data collected for each sample was analyzed. A set of two samples were tested at each condition. Each set of samples at every condition showed repeatable results as demonstrated in Figure 4.5, showing engineering stress-strain curves of two samples in the H1025 condition. The difference in the corresponding proof yield strengths and tensile strengths of each set of samples is within $\pm 5\text{ MPa}$.

Engineering stress-strain curves were plotted for the samples in each condition. A curve representing each condition is shown in Figure 4.6. The slope of the linear elastic section of each curve gives the modulus of elasticity (E), which is found to be around 190GPa in each case. Condition-A has the lowest yield and tensile strengths while H925 has the highest yield and tensile strengths among the three conditions. H1025 has a relatively intermediate yield and tensile strength. Elastic resilience is the maximum energy absorbed per unit volume by the sample without undergoing plastic deformation. The elastic resilience, which largely depends on the yield strength, is measured to be about 3.35, 6.68 and 5.65 MJ/m^3 for Condition-A, H925 and H1025 respectively.

The n-value for condition-A was found to be the highest among the three conditions at about 0.15 and H1025 was found to have the lowest value of about 0.02. H925 condition has an intermediate n value of about 0.06. These properties were very similar for the used replicas; therefore, their average is used for further discussions in this chapter.

Table 4-1 summarizes the measured tensile properties of 17-4 PH stainless steel in each condition. As no changes in the microstructure were observed with the aging treatments (Figure

4.1, Figure 4.2 and Figure 4.3), the change in tensile properties is solely an effect of copper based precipitates [96]–[99].

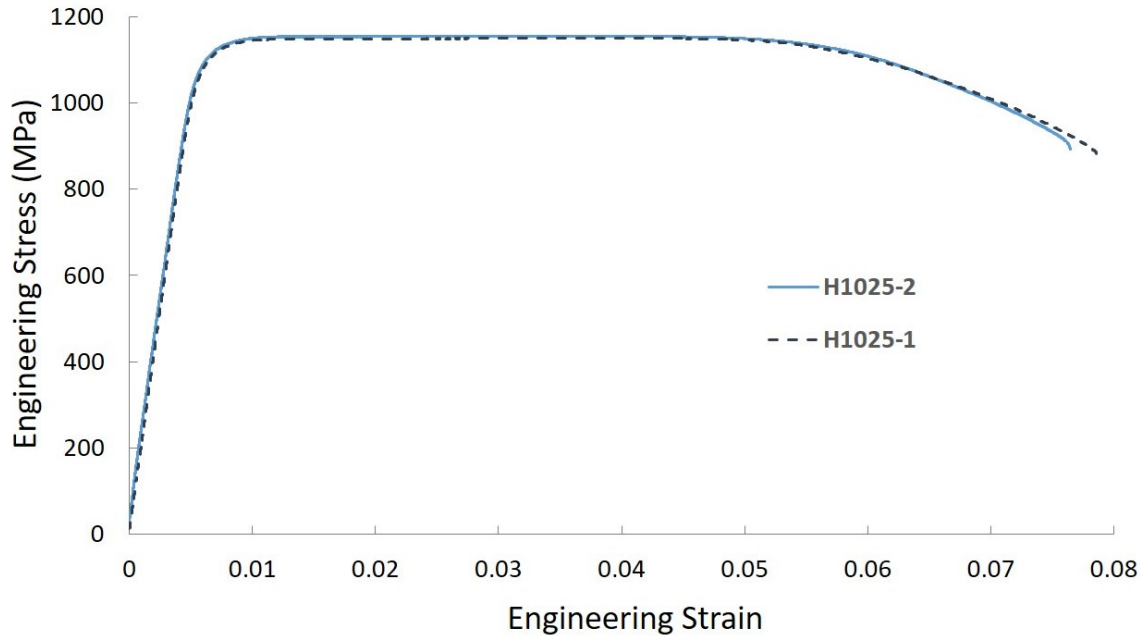


Figure 4.5 Engineering stress-strain curves of samples in H1025 condition.

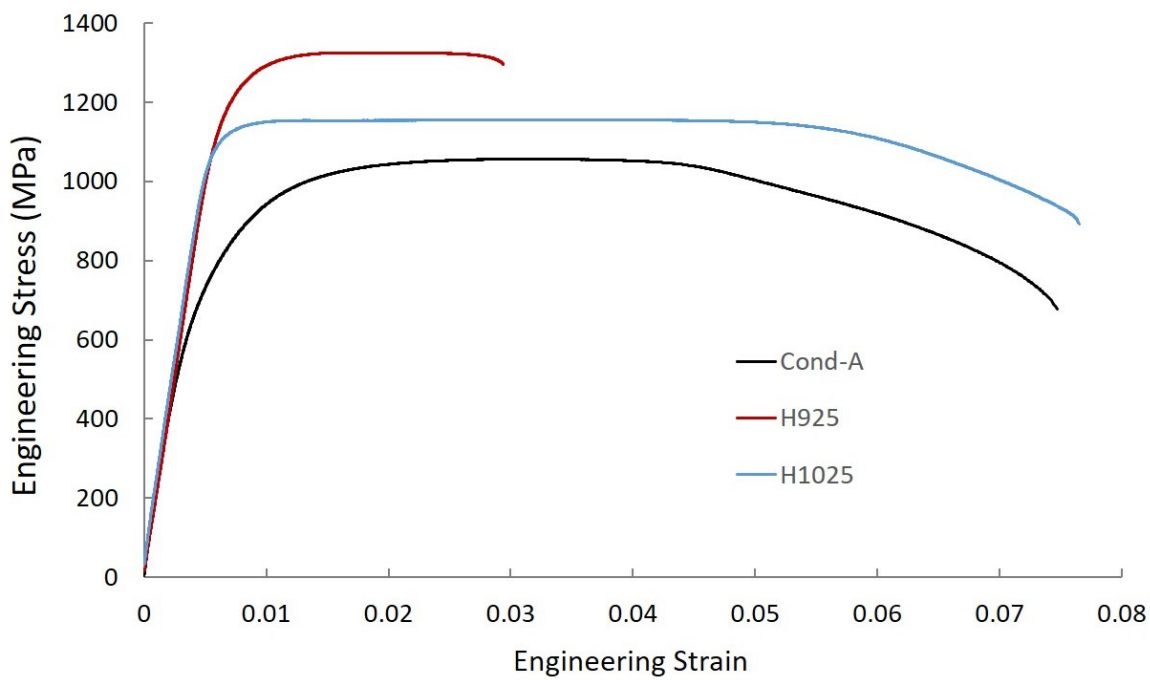


Figure 4.6 Engineering stress-strain curves of 17-4 PH stainless steel.

Table 4-1 Tensile properties summary of 17-4 PH stainless steel.

Sample condition	Strain rate (mm/min.)	% elongation at fracture	Young's modulus (GPa)	0.2% offset Yield strength (MPa)	Tensile strength (MPa)	Strain hardening exponent (n)	Elastic resilience (MJ/m ³)
Condition-A	1	6.9	187	830	1056	0.15	3.35
H925	1	5.5*	195	1257	1324	0.06	6.68
H1025	1	7.1	196	1133	1153	0.02	5.65

* Fracture occurred in the gauge length outside the region covered by extensometer for both the samples in H925 condition.

4.3. Micro-hardness

The micro-hardness values of T-samples in various aging conditions of 17-4 PH stainless steel after grinding with a 1200 grit were acquired using a 500g load for a dwell time of 15sec and are shown in the Table 4-2. The average micro-hardness of Condition-A is about 320 HV_{0.5} and that of H925 and H1025 is 401 and 347 HV_{0.5} respectively. With three passes at 100 bar pressure of the DR surface treatment, an increase in surface micro-hardness is observed for each condition. Similarly, the micro-hardness values and their average after the DR surface treatment were recorded and are shown in the Table 4-2. The average micro-hardness of Condition-A increased to about 337 HV_{0.5} after DR. Expectedly, the H925 and H1025 conditions have increased micro-hardness to 448 and 377 HV_{0.5} respectively due to the DR treatment. The average micro-hardness of Condition-A was consistent for the used replicas.

An increase in micro-hardness with the cold work was observed in each condition but the level of increment is different for each condition. Figure 4.7 shows a comparison of the micro-Vickers hardness in 17-4 PH stainless steel before and after the DR treatment. A rise of about 5.2, 11.6 and 8.7% were observed for Condition-A, H925 and H0125 respectively (Table 4-2). The increment in the values was found to be strongly dependent on the initial hardness of the base material. Among the three conditions, Condition-A and H925, having the least and the highest initial micro-hardness values respectively, show the least and the highest hardness increments after DR treatment. Condition H1025, which had a relatively moderate initial micro-hardness, showed a moderate rise after the DR treatment. The increase in surface micro-hardness after the DR treatment is due to the strain induced by cold working [41], [82].

Table 4-2 Micro-Vickers hardness of polished and DR treated surface of 17-4 PH samples.

	Condition-A	H925	H1025	Condition-A DR	H925 DR	H1025 DR
Micro-hardness readings	323.2	413.5	343.1	338.2	440.1	374.4
	325.0	408.3	345.0	340.6	450.3	374.2
	309.6	397.2	349.2	335.1	443.1	377.2
	320.5	398.4	351.3	336.0	440.9	382.8
	325.0	400.7	341.5	345.0	449.2	379.0
	324.0	404.3	341.9	336.0	451.0	377.5
	328.1	397.5	351.3	334.6	445.5	375.0
	318.2	397.0	343.8	333.3	453.0	378.7
	316.8	401.4	347.7	335.4	452.1	371.2
	317.3	396.1	351.5	342.0	453.4	376.3
Standard deviation	5.4	5.7	4.0	3.8	5.0	3.2
Average:	320.8	401.4	346.6	337.6	447.9	376.7
% Increase in average micro-hardness due to DR:				5.2	11.6	8.7

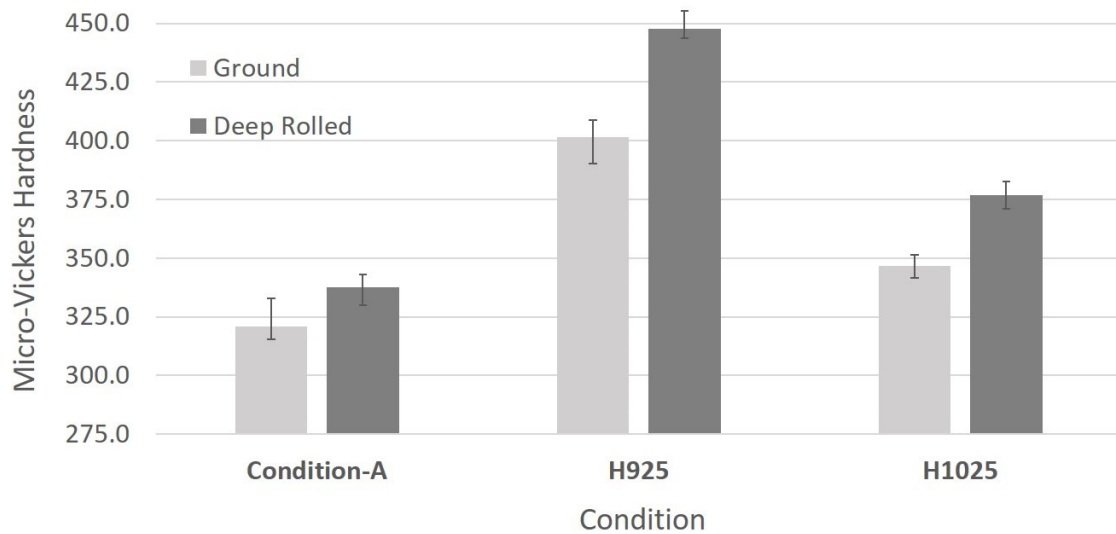


Figure 4.7 Average micro-Vickers hardness of 17-4 PH stainless steel before and after deep rolling.

The X22CrMoV12-1 stainless steel samples used in the stress-relieving experiments are also tested for surface micro-hardness using a 300g load and a dwell time of 15 seconds. The reference samples were only stress-relieved once before the start of the tests so that both samples are at the same state before WDE starts. Two different test samples, corresponding to each stress relieving test (to be relieved after every 2 minutes and 30 seconds of erosion testing), were relieved 6 and 47 times respectively by the end of the tests. The surface micro-hardness was measured to verify if there are significant microstructural changes in the samples from the beginning to the end of the tests. As shown in Table 4-3, the average micro-hardness was about 274 HV_{0.3} after one cycle of stress-relieving, i.e. at the start of erosion tests. The values were consistent for each reference samples in their specific condition. After 6 cycles of stress-relieving, the average micro-hardness value saw a negligible drop to 269 HV_{0.3}. But after 47 cycles of stress-relieving, the average micro-hardness was reduced to about 256 HV_{0.3}. A reduction of about 18 HV_{0.3}, although not significant, could be a result of further tempering of martensite during the relieving cycles.

Table 4-3 Micro-Vickers hardness in X22CrMoV12-1 stainless steel.

	After 1 cycle of stress relieving	After 6 cycles of stress relieving	After 47 cycles of stress relieving
Micro-hardness readings	279.9	267.9	255.7
	265.5	269.9	252.4
	270.8	266.5	260.5
	272.2	272.6	250.1
	275.4	270.9	255.1
	273.1	266.4	257.0
	277.2	269.4	253.3
	280.1	267.8	254.1
	270.1	271.1	259.3
	277.8	269.0	261.6
Standard deviation	4.7	2.0	3.7
Average:	274.2	269.2	255.9

4.4. Surface roughness

The average line surface roughness prior to erosion testing of each sample is calculated by taking an average of 20 roughness measurements. The average values are shown in Table 4-4. The average surface roughness of the DR samples is comparable and is about $0.105\mu\text{m}$ for each sample with a standard deviation of $0.028\mu\text{m}$. The ground samples which were progressively ground to a 1200grit finish had an average surface roughness of about $0.012\mu\text{m}$ with a standard deviation of $0.002\mu\text{m}$. The surface roughness was comparable for each ground sample and was better than that of the DR samples.

Table 4-4 Average surface roughness of erosion samples.

Sample	Average surface roughness, R_a (μm)	Standard deviation
Condition-A DR	0.113	0.028
H925 DR	0.105	0.011
H1025 DR	0.103	0.021
Condition-A ground	0.013	0.001
H925 ground	0.012	0.001
H1025 ground	0.011	0.002

The surface appearance was consistent among the samples having the same type of surface preparation (i.e. DR treatment or grinding). Therefore, only one sample from each type is discussed here. A comparison of surface topology of the DR and ground samples were observed at the same magnification is shown in Figure 4.8. The plastic deformation marks along the rolling direction can be seen on the DR treated samples. Three rolling passes create a series of parallel deformation tracks and micro-pit like defects in the DR samples. These defects are limited to the surface of the DR samples as they were not observed in the cross-sections shown in Figure 4.1, Figure 4.2 and Figure 4.3. The ground samples have a plain surface without any such deformation marks or surface defects. The relatively greater surface roughness in the DR treated samples can be attributed to the deformation tracks.

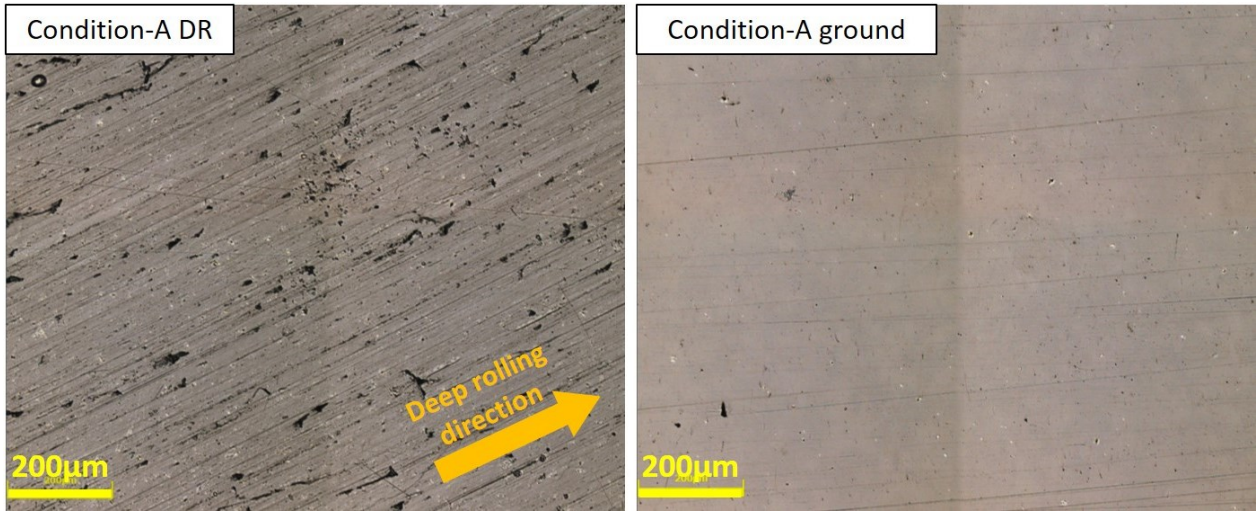


Figure 4.8 Surface appearance of Condition-A samples with DR treatment and 1200grit ground finish.

4.5. Erosion performance

Different stainless steels have been characterized for erosion with the purpose of studying the effect of strain hardening on WDE as discussed in section 3.1. 17-4 PH stainless steel was used for all the strain hardening experiments. These experiments are performed on samples with and without DR surface treatment. The X22CrMoV12-1 stainless steel was only used for the stress relieving experiments.

The observations from sections 4.1 to 4.4 are used to discuss their influence on WDE in this section. As discussed in section 2.1.3, during the incubation period, plastic strain is progressively developed along with repeated dissipation of energy by elastic deformation. The accumulated plastic strain due to repeated impacts contributes to hardening of the material [34], [39]. In case of WDE, it can be said that resilience is roughly proportional to the amount of energy that is dissipated without causing damage during each loading cycle [71]. The strain hardening exponents and elastic resilience for each condition will therefore be used to analyze the results of strain hardening experiments (section 4.5.2). The surface roughness is measured because lower surface roughness will elongate erosion incubation at the same impact conditions

[46]. The surface finish is found to be dissimilar for each surface preparation type (with and without DR). Since DR treatment resulted in higher roughness than the grinding, this must contribute to the improved WDE performance of the reference samples.

4.5.1. Demonstration of repeatability

Polished 17-4 PH stainless steel samples were tested for erosion in the as-received condition which is the solution annealed Condition-A. Both samples were ground uniformly to a 1200grit surface finish. Erosion tests using impact speeds of 250 and 300m/s were performed on identical samples to ascertain the repeatability of the erosion tests on this erosion rig. The result for the test performed at 300m/s is shown below. Figure 4.9 and Figure 4.10 show the cumulative mass loss versus time and the instantaneous erosion rate versus time curves respectively, to demonstrate repeatability on this erosion rig. Each curve in Figure 4.9 and Figure 4.10 represents an identical sample with 1200grit surface finish.

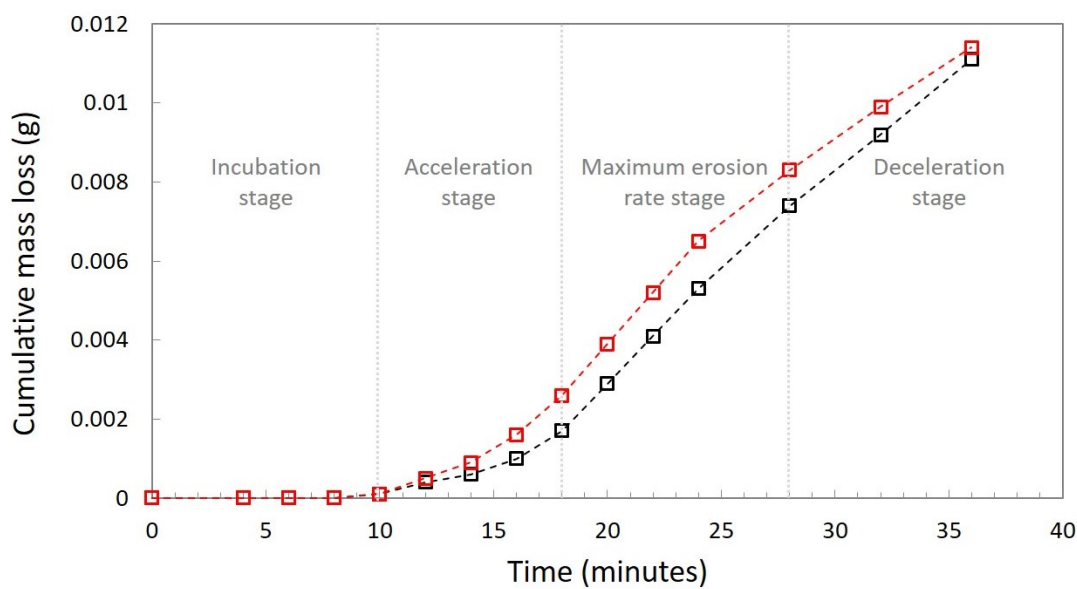


Figure 4.9 Repeatability WDE test of 17-4 PH stainless steel in As-Received condition at impact speed of 300 m/s.

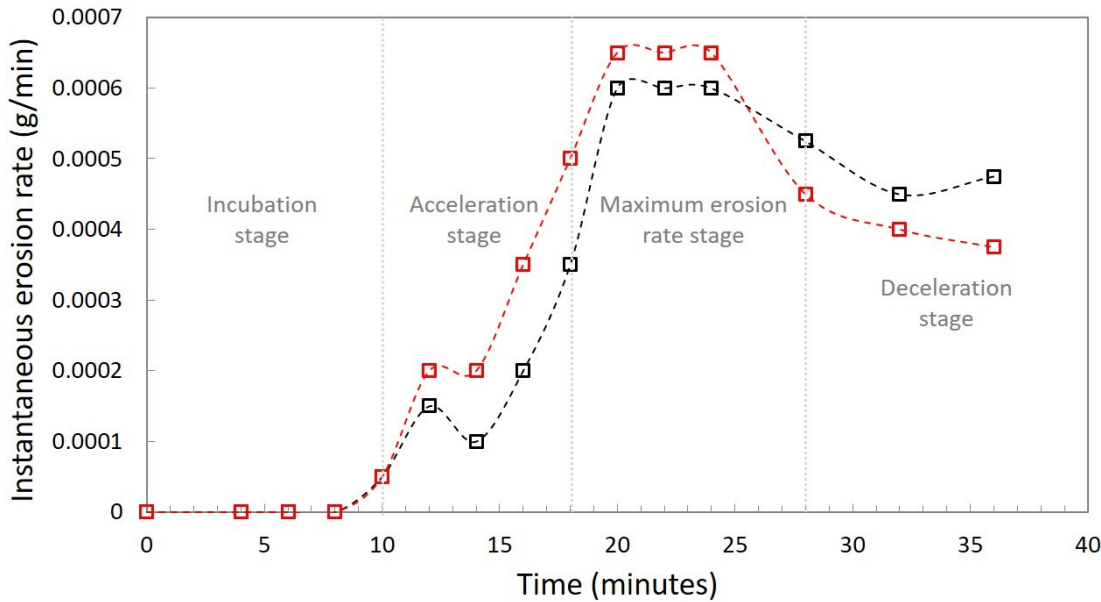


Figure 4.10 Instantaneous erosion rate curve of 17-4 PH stainless steel in As-Received condition at impact speed of 300m/s.

As can be seen in Figure 4.9, similar erosion curves of both samples demonstrate the uniformity in conditions experienced by each sample during the erosion test. It is therefore safe to compare the erosion performance of samples undergoing similar erosion conditions during a test. However, the erosion performance between different tests can only be qualitatively compared owing to the differences that may have arisen from the testing conditions itself. The separation between the curves observed during their maximum erosion rate stage could be due to some of the uncontrollable differences in grain size, orientation and erosion crater dynamics. No difference in the incubation time was observed as it can only be detected if the cycle duration is shorter than the difference in incubation times. Hence, the cycle duration during the initial stages has to be selected as small as practically possible. Despite having the same incubation time, there could be a difference in acceleration or maximum erosion rate leading to an error in mass loss during the maximum erosion rate stage. A maximum error of 0.0011g in mass loss is observed between the curves during the maximum erosion rate stage at impact

speed of 300m/s. A maximum difference of 0.00005g/min in the instantaneous erosion rate is observed during the maximum erosion rate stage as can be seen in Figure 4.10. Similarly, a maximum error of 0.002g in mass loss during the maximum erosion rate stage and a maximum difference of 0.00005g/min in the instantaneous erosion rate during the maximum erosion rate stage are observed at an impact speed of 250m/s. Therefore, such differences in mass loss and/or instantaneous erosion rate are considered to be within the acceptable range for the 17-4 PH steel samples from the WDE test as summarized in Table 4-5. It is worth noting that the erosion curve of 17-4 PH stainless steel shows an atypical acceleration stage which differs from that of most other metals. Although this stage appears elongated in the mass loss curve, there is no significant rise in mass loss. Therefore, a hump or a step is reflected in the acceleration stage of the instantaneous erosion rate curve of this material, which is absent in Figure 2.1(b). Some titanium alloys have reportedly shown similar atypical WDE behavior [4].

Table 4-5 Acceptable difference in mass loss and erosion rate during maximum erosion rate stage.

Impact speed (m/s)	Mass loss accuracy range	Erosion rate accuracy range
250	$\pm 0.0020\text{g}$	$\pm 0.00005\text{g/min}$
300	$\pm 0.0011\text{g}$	$\pm 0.00005\text{g/min}$

In this study, cumulative mass loss and the instantaneous erosion rate are plotted against the exposure time in minutes. It is to be noted that the same exposure time results in different number of droplet impingements for WDE tests conducted at different impact speeds on this erosion rig. This difference arises due to the different rotational speeds that are used to achieve the desired impact speeds. The number of droplet impingements over a period of time can be calculated from exposure time using Equation-12. Where the average number of droplet

impingements per rotation is 6 droplets per 8mm width of the sample (as discussed in the section 3.3.1); WDE test speeds of 250 and 300m/s are achieved at 10,000 and 12,000 RPM respectively in this erosion rig; and the exposure time is in minutes. The product of RPM and exposure time in minutes gives the number of cycles of droplet impacts.

$$\text{Number of droplets } (N_{drop}) = N_{drop/rotation} * \text{RPM} * \text{time} \quad \dots \dots \dots \quad (12)$$

4.5.2. Strain hardening results

The erosion behavior of 17-4 PH stainless steel with and without DR is discussed in this section. The 17-4 PH stainless steel in each condition was tested for WDE at 250 and 300 m/s impact speeds. Condition-A was chosen as a reference condition for all the strain hardening experiments because of its relatively greater n-value, allowing for the evaluation of erosion performance with respect to their n-values.

4.5.2.1. Erosion behavior without DR treatment

To examine the erosion behavior of 17-4 PH without the DR surface treatment, test coupons were used. This set of experiments is performed to solely ascertain the general WDE performance of 17-4 PH in Condition-A, H925 and H1025. The coupon test surface of each sample is ground to a 1200 grit finish. Each sample from this set of experiments is therefore named by its condition followed by a suffix ‘ground’ in the figures.

The erosion curves of Condition-A versus H925 and Condition-A versus H1025 at impact speed of 250m/s are shown in Figure 4.11 and Figure 4.12, respectively. The incubation period was 38 minutes long for Condition-A in each case while it was 98 and 53 minutes for H925 and H1025, respectively. The incubation time of H925 and H1025 are about 2.5 times and 1.4 times that of Condition-A, respectively. The maximum erosion rate is about

0.000085g/min in H925 (Figure 4.11) and is about 0.000097 and 0.000095g/min in Condition-A and H1025, respectively (Figure 4.12 and Figure 4.11). A significant difference in the incubation times of H925 and Condition-A is observed while the maximum erosion rate is similar. H1025 has a slightly longer incubation time and a similar maximum erosion rate; hence, the behavior of H1025 is considered only marginally better than Condition-A. The difference in erosion performance, in terms of incubation time, between Condition-A versus H925 is clearly discernible. The difference observed in the case of Condition-A versus H1025 is small, despite the greater strength and elastic resilience of H1025 compared to Condition-A. The difference in incubation times at 250m/s impact speed can also be observed in the macrographs shown in Figure 4.13 and Figure 4.14. H925 results in larger increase in incubation time than H1025.

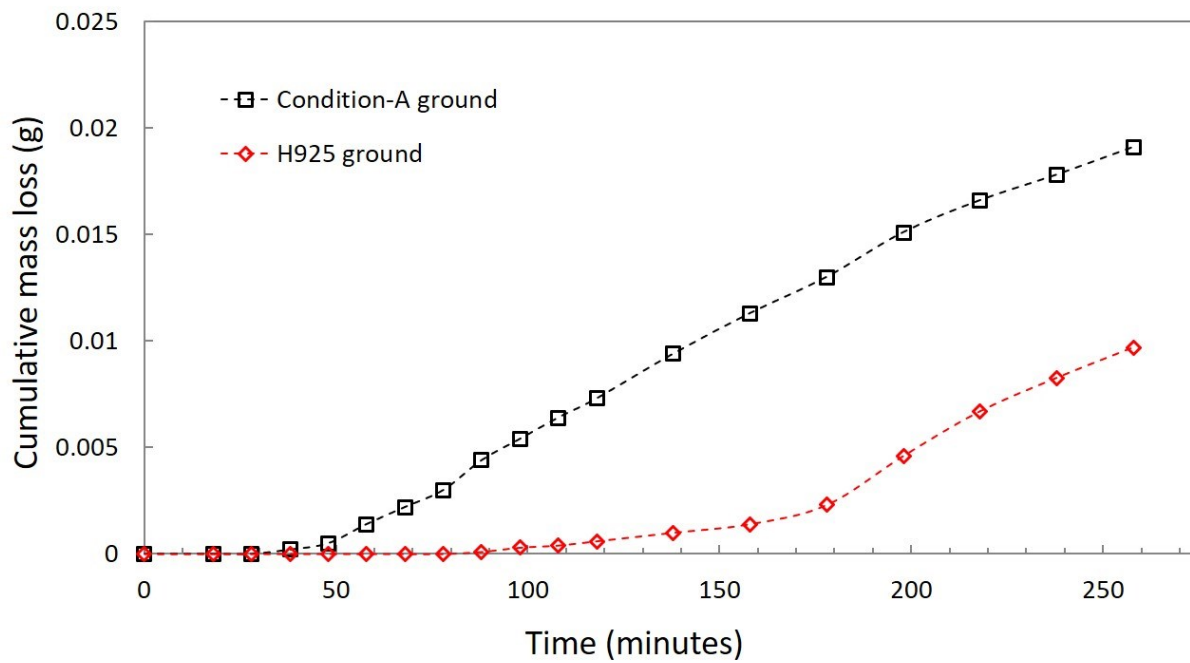


Figure 4.11 Erosion curves of Condition-A vs H925 without the DR treatment at impact speed of 250m/s.

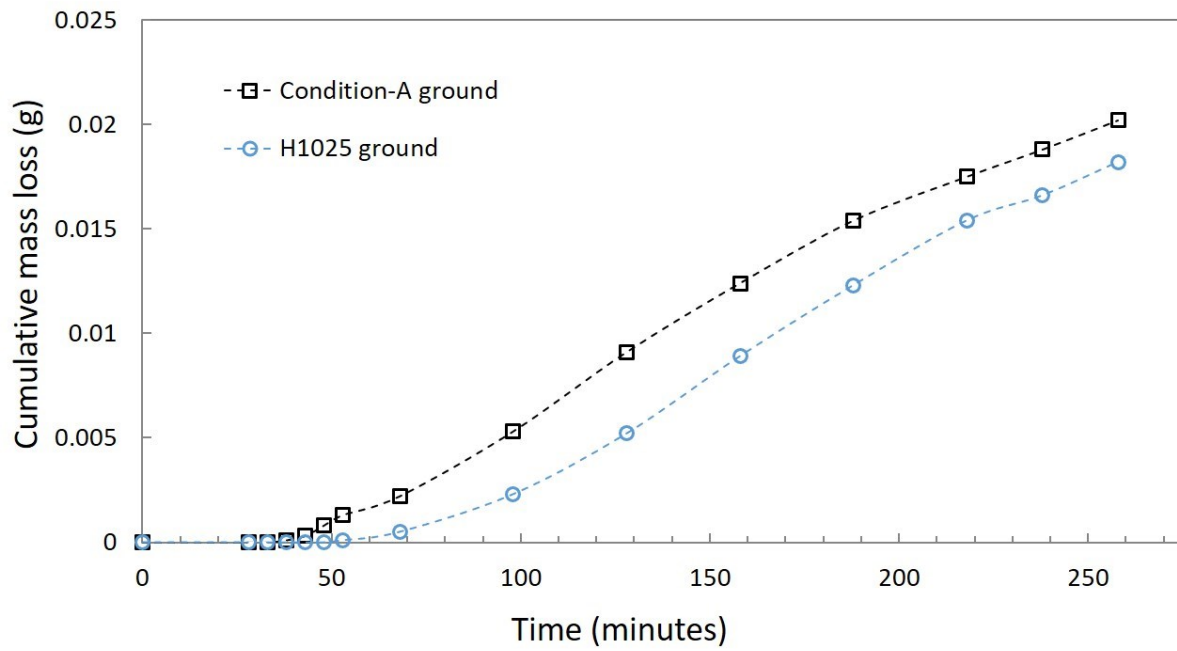


Figure 4.12 Erosion curves of Condition-A vs H1025 without DR treatment at impact speed of 250 m/s.

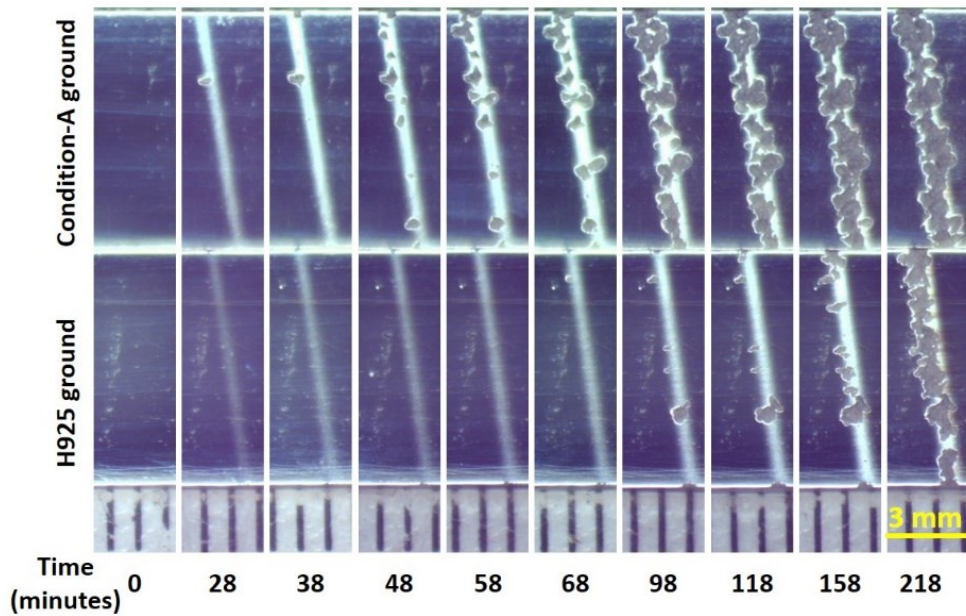


Figure 4.13 Evolution of craters in Condition-A ground versus H925 ground tested at 250 m/s. These macrographs correspond to Figure 4.11.

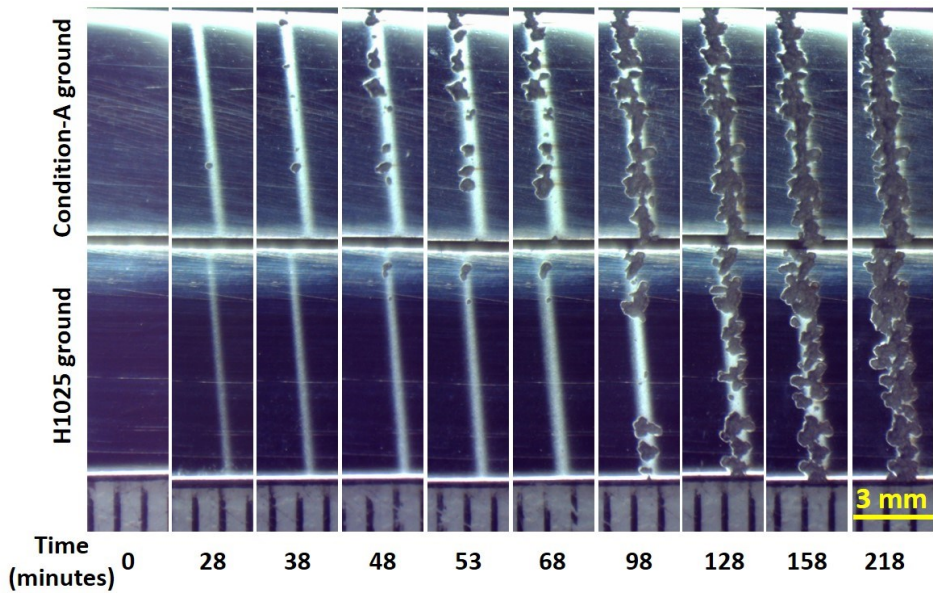


Figure 4.14 Evolution of craters in Condition-A ground versus H1025 ground tested at 250 m/s. These macrographs correspond to Figure 4.12.

The erosion curves of Condition-A versus H925 and Condition-A versus H1025 at impact speed of 300m/s are shown in Figure 4.15 and Figure 4.16, respectively. The incubation time is about 10 minutes for Condition-A in each case and is about 10 and 12 minutes for H1025 and H925, respectively. The maximum erosion rate is about 0.000350g/min for H925 (Figure 4.15) and is about 0.0005 and 0.000410g/min for Condition-A and H1025 respectively (Figure 4.16). As the impact speed was increased to 300m/s, the erosion progressed faster i.e. shorter incubation and greater erosion rate are observed. After comparing the samples at this speed (300m/s), H925 had a slightly better performance to Condition-A in terms of incubation time and maximum erosion rate. H1025 had a very similar erosion behavior to Condition-A with no difference in incubation time or maximum erosion rate. While the difference in incubation time and maximum erosion rate is negligible in Condition-A versus H925, H925 has a relatively longer acceleration. Slightly improved erosion performance, with respect to that of Condition-A, is observed in H925 but not in H1025 at 300m/s. This is in accordance with the

evolution of craters in Condition-A versus H925 and Condition-A versus H1025 tested at 300m/s shown in Figure 4.17 and Figure 4.18, respectively.

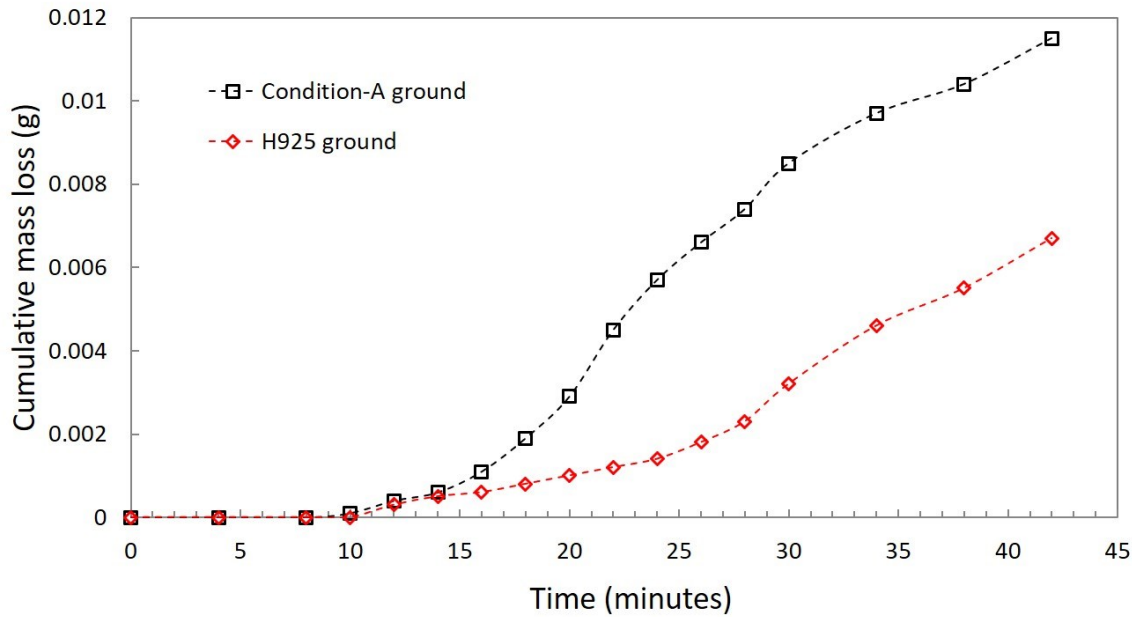


Figure 4.15 Erosion curves of Condition-A vs H925 without the DR treatment at impact speed of 300m/s.

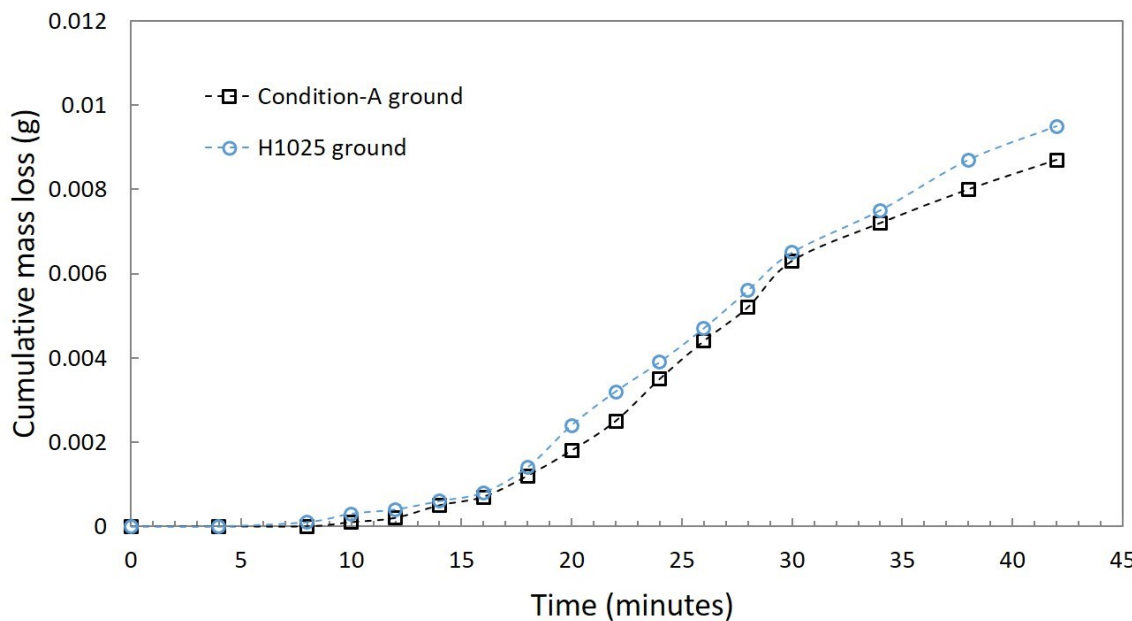


Figure 4.16 Erosion curves of Condition-A vs H1025 without the DR treatment at impact speed of 300m/s.

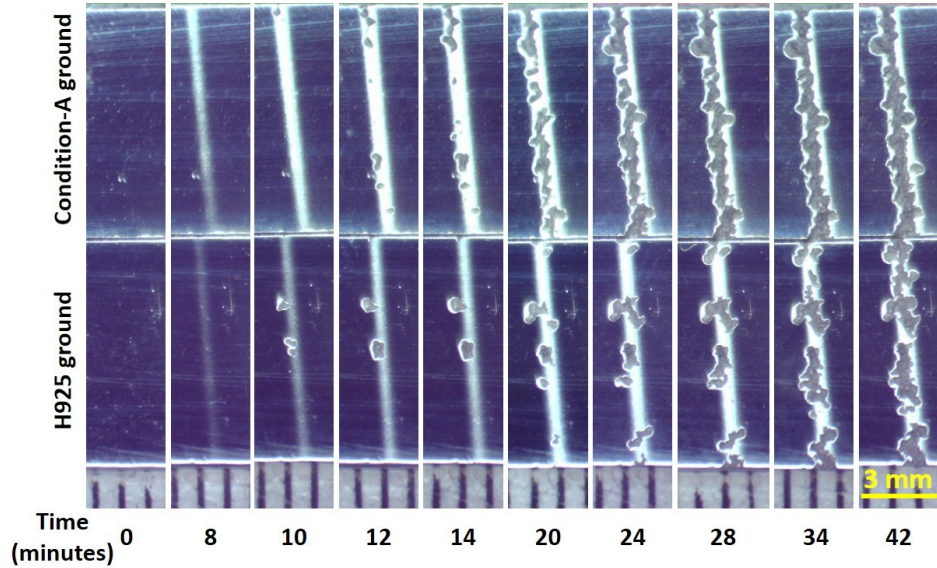


Figure 4.17 Evolution of craters in Condition-A ground versus H925 ground tested at 300 m/s.

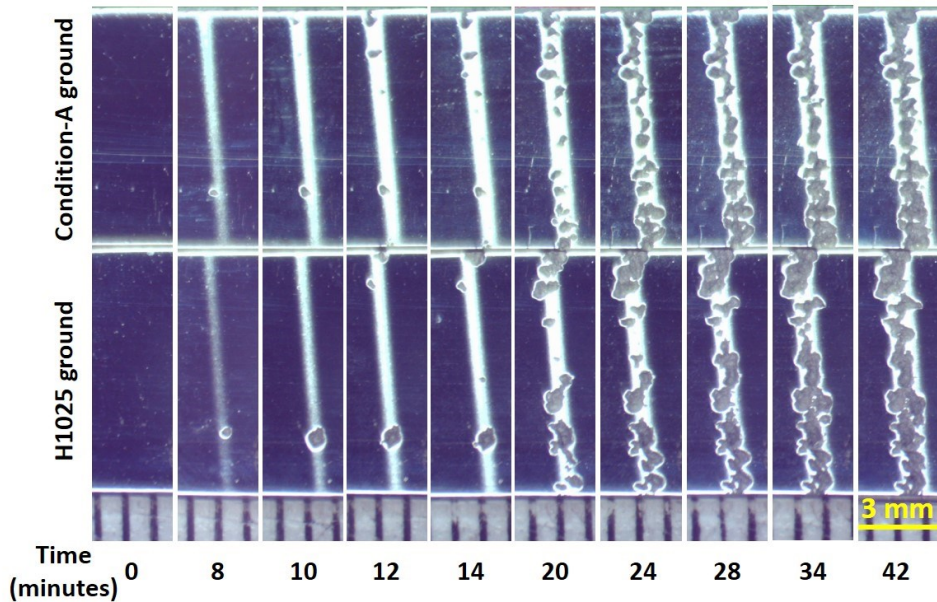


Figure 4.18 Evolution of craters in Condition-A ground versus H1025 ground tested at 300 m/s.

Figure 4.19 and Figure 4.20 summarize the erosion curves of ground samples at 250 and 300m/s, respectively. The aging treatments on Condition-A have resulted in H925 and H1025 conditions possessing improved properties such as strength and elastic resilience as discussed in section 4.2. Greater strength and elastic resilience are known to improve the erosion

resistance in metals as reported in [9], [43], [71]. While Condition-A has relatively low strength and elastic resilience among the three conditions, H925 and H1025 have relatively high and moderate strengths and elastic resilience respectively. Although the erosion behavior of the ground samples is in the order of their strengths, it is clearly not proportionate to their strengths or elastic resilience. The disproportionate erosion performance with respect to their strengths and elastic resilience is observed at both impact speeds. The erosion curve of H1025 is similar to that of Condition-A as opposed to the erosion curve of H925 which diverges tremendously from the curve of Condition-A. As the WDE is a progressive damage phenomenon, the work hardening from repeated impacts is believed to play a role in erosion [4], [28], [39]. Therefore, the influence of strain hardening on WDE behavior of 17-4 PH stainless steel is investigated by including the strain hardening exponents in the current work.

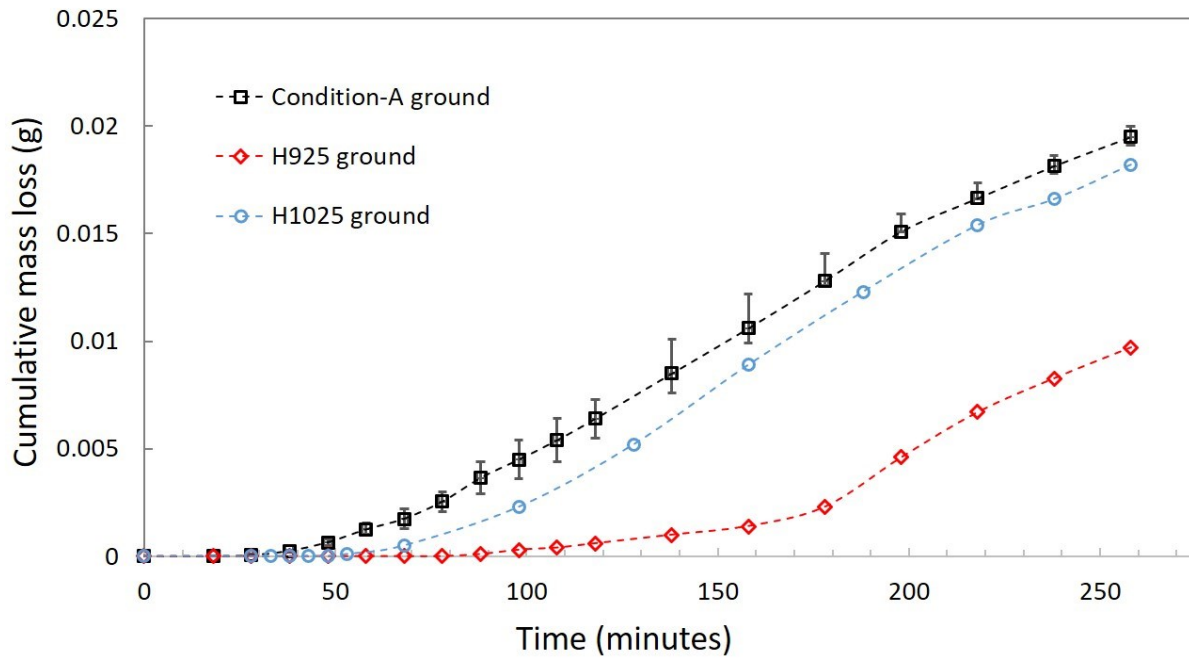


Figure 4.19 Erosion curves of ground samples at impact speed of 250 m/s.

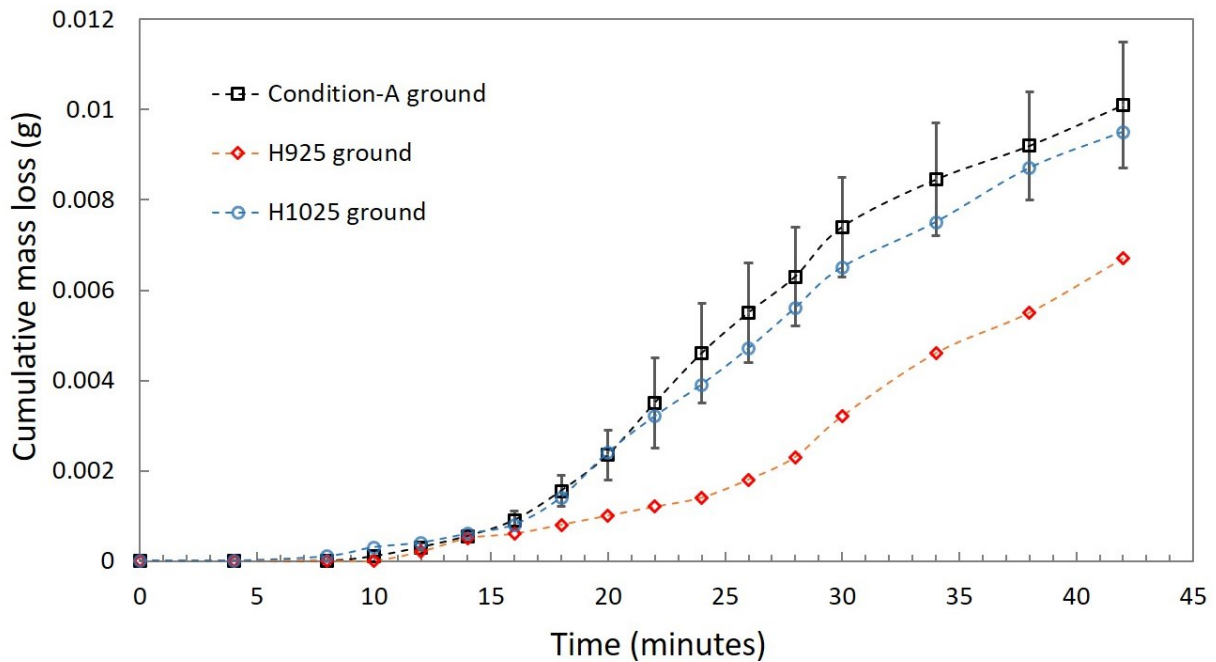


Figure 4.20 Erosion curves of ground samples at impact speed of 300 m/s.

Radar charts are plotted with various mechanical properties against the erosion incubation times for impact speeds of 250 and 300m/s as shown in Figure 4.21 and Figure 4.22, respectively. These radar charts are plotted with Condition-A as a reference condition, so the variation in incubation time can be visualized with respect to the variation in their mechanical properties. The strength, elastic resilience and micro-hardness of both H925 and H1025 are greater than those of Condition-A. However, only the erosion resistance of H925 is found to be relatively greater. This inconsiderable difference in erosion behavior of Condition-A and H1025 is apparent at both impact speeds (250 and 300m/s) despite considerable difference in their strength and elastic resilience. Table 4-6 provides a summary of these observations. Of the various mechanisms discussed in section 2.1, strain builds up progressively at the exposed surface under the influence of impact pressures and lateral jetting until failure i.e. the end of incubation period. Therefore, the erosion behavior is discussed further in terms of tensile behavior of each condition observed in section 4.2.

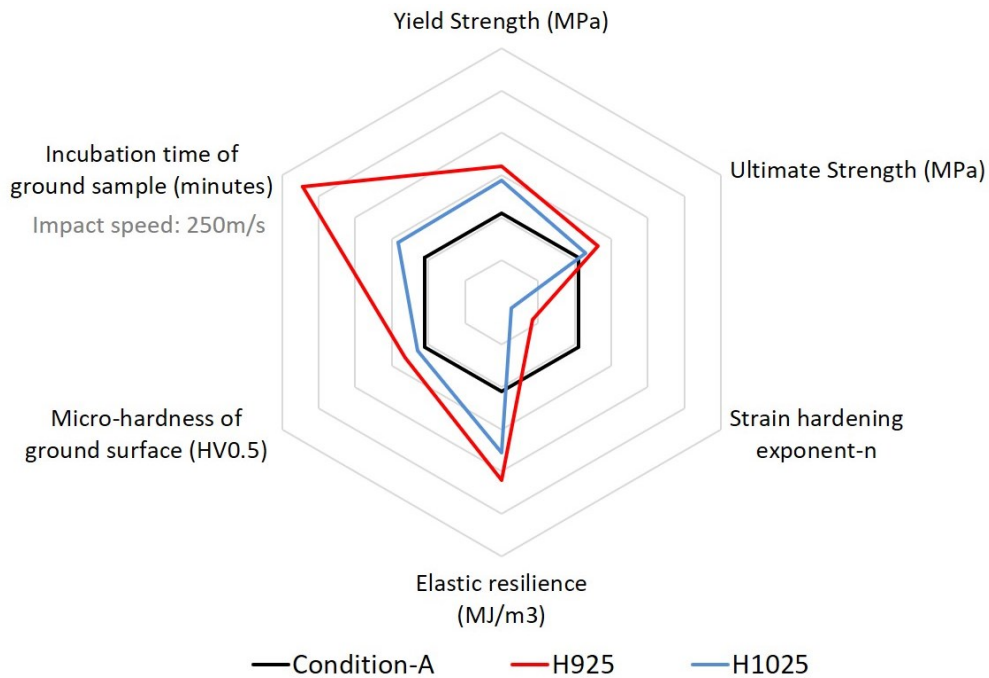


Figure 4.21 Radar chart showing erosion incubation time of ground samples tested at 250m/s and mechanical properties of each condition.

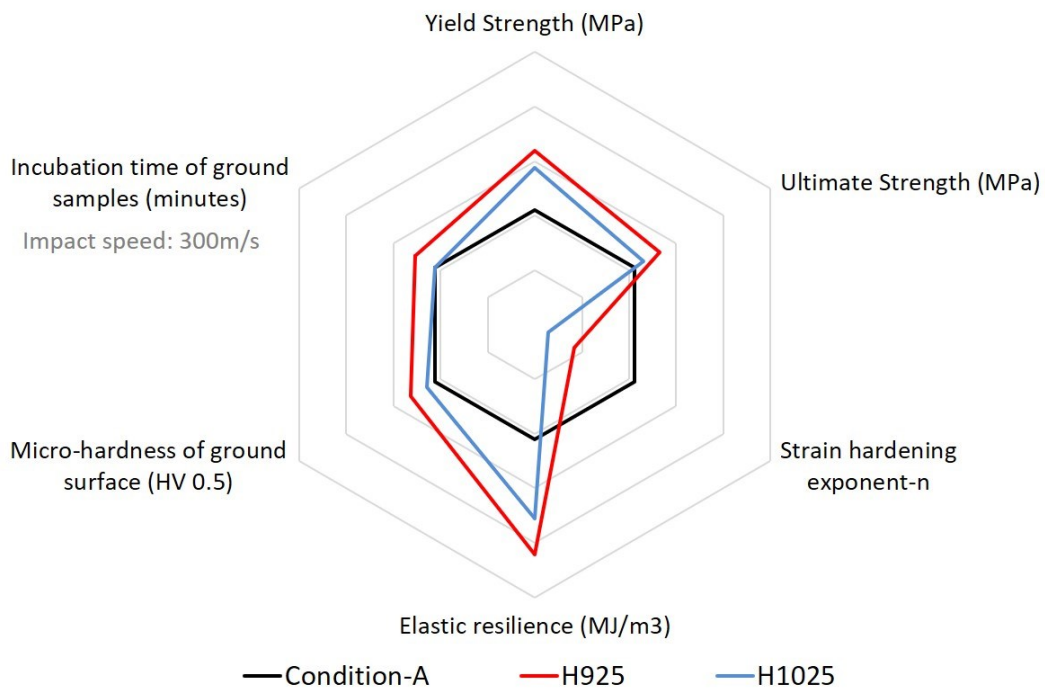


Figure 4.22 Radar chart showing erosion incubation time of ground samples tested at 300m/s and mechanical properties of each condition.

Table 4-6 Summary of relative properties and erosion performance of ground samples for each condition.

Condition	Yield Strength	Ultimate strength	Elastic resilience	Strain hardening exponent	Erosion performance (250m/s)	Erosion performance (300m/s)
Condition-A	Low	Low	Low	High	Low	Low
H925	High	High	High	Intermediate	High	High
H1025	Intermediate	Intermediate	Intermediate	Low	Low	Low

Materials gain strength and elastic resilience due to strain hardening. The rate at which material gains strength is indicated by its strain hardening exponent ‘n’. Condition-A has lower strength but greater rate of strain hardening. H1025 has relatively moderate strength but barely strain hardens. H925 has both greater strength and strain hardening than H1025. With the accumulation of strain in material, the yield point advances towards the fracture point along its curve and consequently the elastic resilience is also increased. A schematic which shows the difference in strain hardening behavior in each condition can be seen in Figure 4.23. The points A, J and P are the yield points of unstrained Condition-A, H1025 and H925 respectively. When exposed to droplet impacts, strain is developed in the material depending on the experienced resistance. The resistance to develop strain is provided in terms of its yield strength and elastic resilience. It is assumed that during each cycle of impacts, the elastic resilience energy is dissipated and the strain is developed when the impacting energy exceeds resilience. Therefore, the greater the yield strength of a material, the greater is the resistance of that material to develop further strain. When each condition is exposed to the same number of droplet impact cycles (N), the strain causes its yield point to shift towards its fracture point. For instance, the yield point could progressively shift from A to B, from J to K and from P to Q in Condition-A,

H1025 and H925 respectively after N cycles of droplet impacts, due to strain hardening (Figure 4.23).

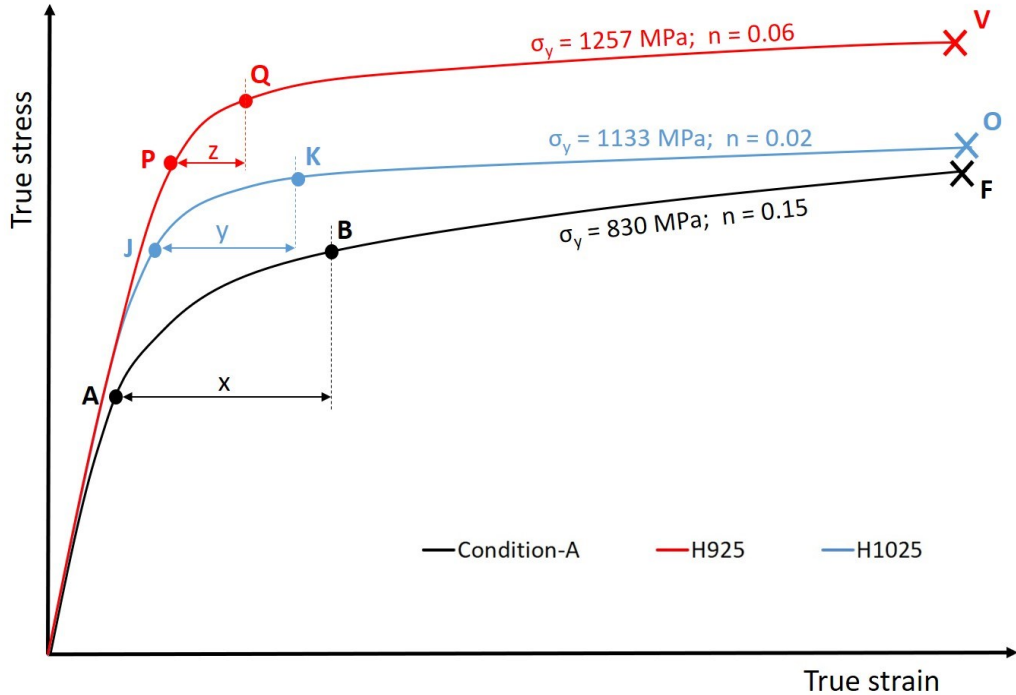


Figure 4.23 Schematic showing progression of yield point due to strain in ground samples.

The shift in yield points by distances x , y , and z , in the graph is observed for Condition-A, H1025 and H925 respectively. This progression of yield point is governed by yield strength and elastic resilience at each cycle of impact. It is worth noting that the elastic resilience is greater at points B, K and Q compared to that at points A, J and P respectively. The resistance to each N cycles of droplet impacts is greater than that during the previous N cycles. This means the yield point progresses by distances less than x , y and z in respective conditions after successive N impact cycles. These distances are progressively reduced until the fracture point at a rate which depends on the n value of condition. Not much change is expected in strength and elastic resilience when observing H1025 (for instance from K to O) due to its small n -value. On the other hand, a large change in strength and elastic resilience can be expected in

Condition-A (from B to F) due to its large n-value. The rate at which the yield point progresses towards fracture is hence greater in Condition-A than in H1025. Fracture marks the end of incubation here and the time taken to reach the fracture point is the incubation time. Various other erosion mechanisms come into play once the erosion starts. In addition to mechanical properties, the erosion pit shape and dimensions play an important role in erosion [106].

Considering strain hardening and the progressive increase in elastic resilience, it can be concluded that the shorter incubation time of H1025 is due to its very low n-value despite having a greater yield strength compared to Condition-A. In other words, the identical performance of Condition-A and H1025 is due to their lower yield strength but greater n-value of Condition-A, and also due to a greater yield strength but lower n-value of H1025 condition. The superior erosion performance of H925 is due to its greater starting yield strength and also because of work hardening, which provides even greater resistance to develop strain.

4.5.2.2. Erosion behavior after DR treatment

The 17-4 PH stainless steel samples with DR surface treatment are evaluated for their WDE behavior using T-samples contrary to coupons. H925 and H1025 were tested against Condition-A as a reference at 250 and 300m/s impact speeds. The test surface of each T-sample is deep rolled and each sample from this set of experiments is therefore named by its condition followed by a suffix ‘DR’ in the figures. The DR treatment induces strain in addition to Compressive Residual Stresses (CRS) which are beneficial for fatigue properties [41], [74], [82], [107]. This set of experiments is performed to study the WDE behavior of 17-4 PH stainless steel modified via DR surface treatment and the results are later compared with those of ground samples (in section 4.5.2.3) to study the contribution of DR to the WDE performance.

Before performing the experiments with DR samples, the rolling pressure to be applied on the T-sample preparation for the WDE experiments had to be finalized through verifying the effect of pressure on WDE performance. For this reason, some of the Condition-A samples were DR treated at rolling pressures of 100bar and 200bar, and tested against each other for erosion at 250 and 300m/s. No difference in incubation times was observed but the maximum difference in mass loss during the maximum erosion rate stage was about 0.0025g and 0.0016g at impact speeds of 250 and 300m/s respectively. Taking into account the repeatability of the WDE test, the erosion performance of the 100bar sample was marginally better than that of the 200bar sample at both speeds. It is natural to have greater work hardening in materials with higher rolling pressure [39]. This means the 100bar samples can take additional droplet strikes before failure compared to the 200bar samples and this explains the better erosion behavior of 100bar. Using a 100bar rolling pressure for samples will maximize the focus on erosion response of DR treated samples by allowing more strain from droplet impacts during the incubation period. Therefore, 100bar rolling pressure was selected for preparing each DR T-sample in this study.

The erosion curves of Condition-A versus H925 and Condition-A versus H1025 at impact speed of 250m/s are shown in Figure 4.24 and Figure 4.25, respectively. The incubation period of Condition-A is about 48 minutes in each case. H925 and H1025 have relatively longer incubation times of 158 and 68 minutes, respectively. At 250m/s, the distinction in their incubation period is clearly evident. The incubation period of H925 is about 3.3 times that of Condition-A and the incubation period of H1025 is slightly longer than that of Condition-A. The maximum erosion rate is about 0.000148g/min in Condition-A. The maximum erosion rates in H925 (Figure 4.24) and H1025 (Figure 4.25) are similar to that in Condition-A at about

0.000111 and 0.000120g/min, respectively. While the differences in incubation time are clearly discernible, the maximum erosion rate is similar for each condition. In terms of incubation period, it can be said that H925 had a superior erosion performance as its incubation period ends at about the start of deceleration stage in Condition-A. H1025 showed a marginally better erosion performance, in terms of incubation period, compared to that of the Condition-A.

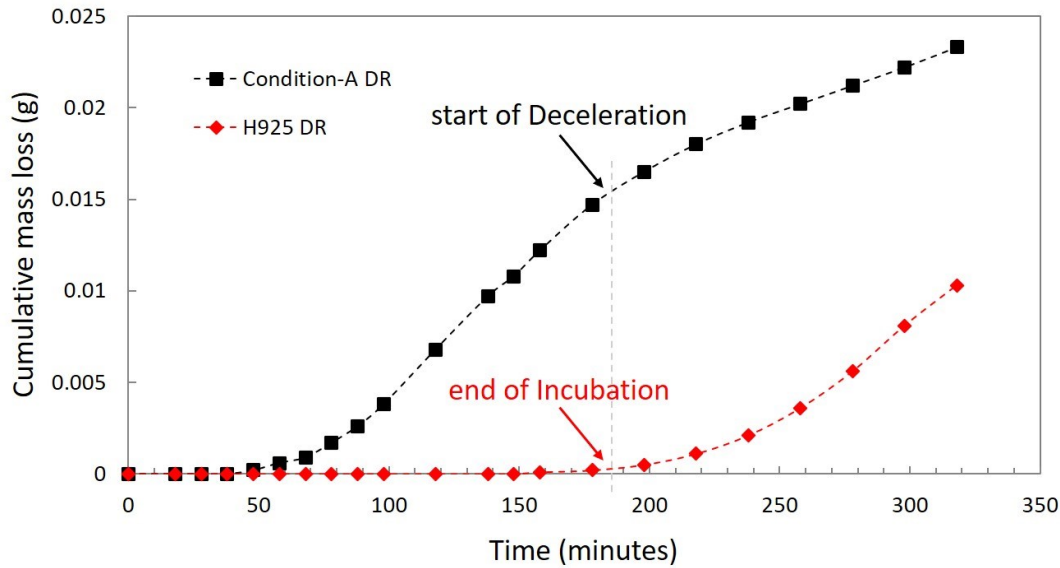


Figure 4.24 Erosion curves of Condition-A vs H925 with DR treatment at impact speed of 250m/s.

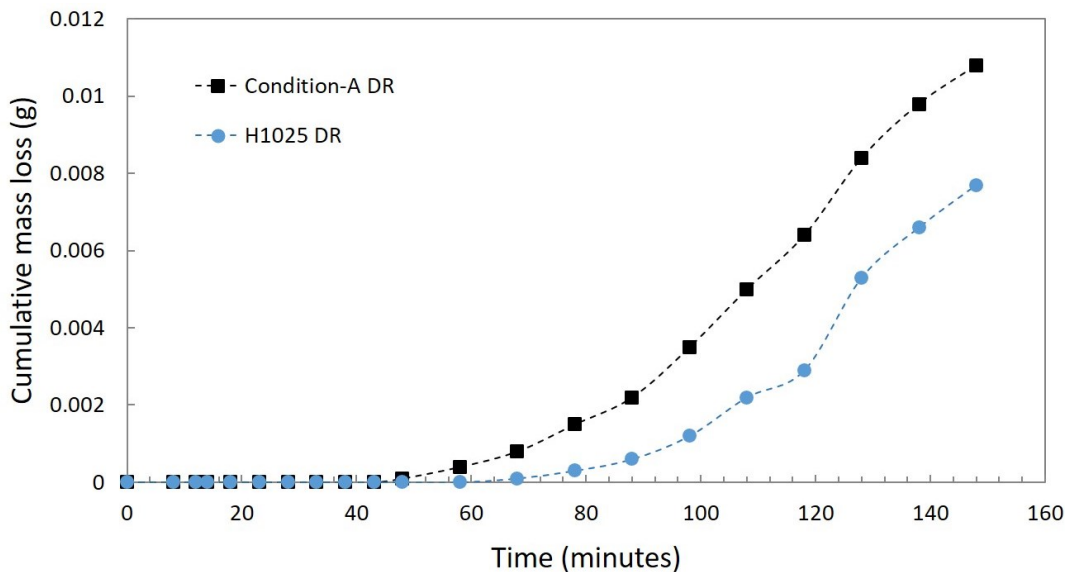


Figure 4.25 Erosion curves of Condition-A vs H1025 with DR treatment at impact speed of 250m/s.

The evolution of craters in the DR samples tested at 250 m/s is shown in Figure 4.26 and Figure 4.27. The end of the incubation period is typically marked by surface roughening and loss of material through the formation of micro-pits [46], [50]. The micro-pits grow in their size to form large visible pits with successive droplet impacts. It can be observed that the pit formation in H925 starts after a significant delay in comparison with Condition-A (Figure 4.26). Not much time difference in the start of erosion is observed between H1025 and Condition-A (Figure 4.27). The erosion mass loss is accelerated (due to impact pressures and lateral jetting) with successive impacts as the pits grow in size and coalesce to form a crater. As the erosion crater develops in its width and depth, the sample erodes to the maximum erosion rate stage. Erosion in H925 only started after the crater is fully developed in Condition-A, thereby making H925 significantly better than Condition-A (Figure 4.26). Beyond the maximum erosion rate stage, only a minute change in crater width is observed as the crater primarily deepens and the erosion starts to decelerate [50].

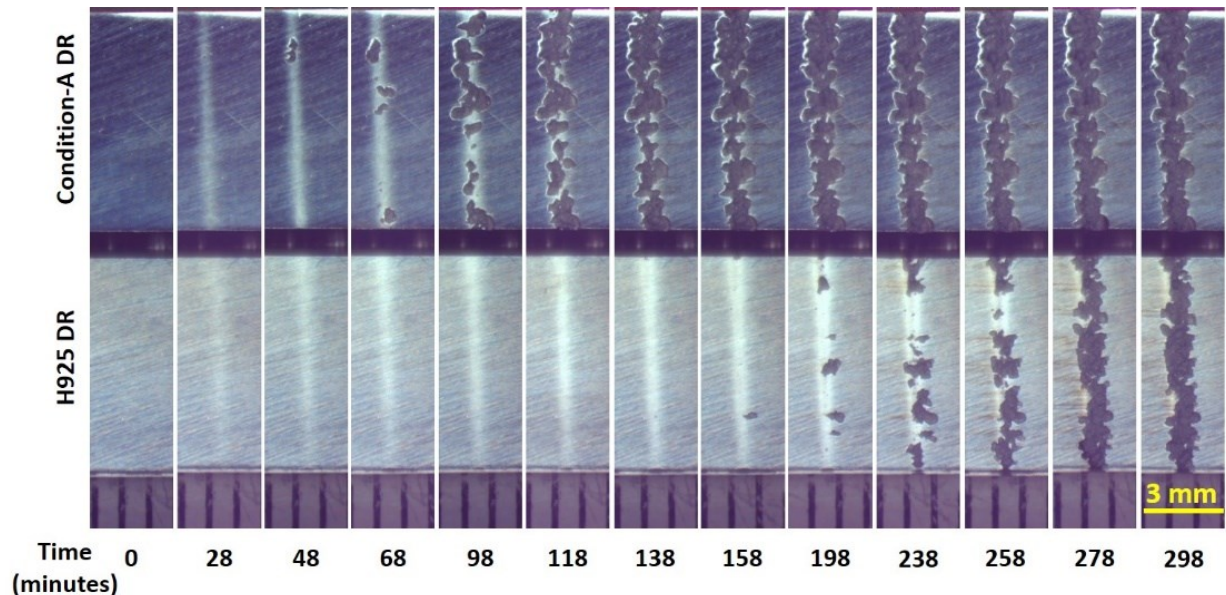


Figure 4.26 Evolution of craters in Condition-A DR versus H925 DR tested at 250 m/s.

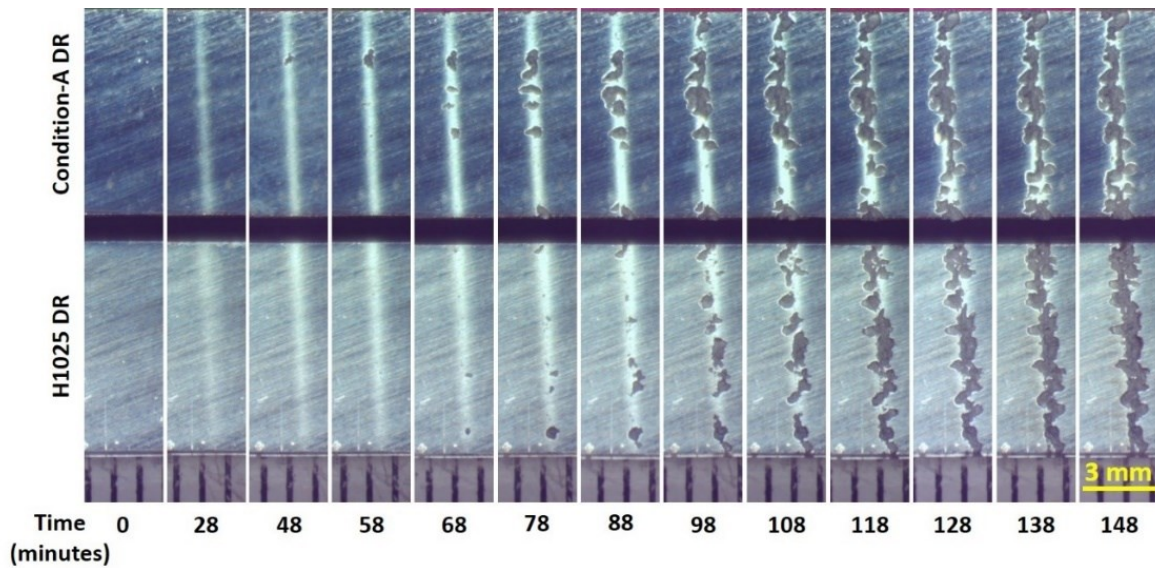


Figure 4.27 Evolution of craters in Condition-A DR versus H1025 DR tested at 250 m/s.

The erosion curves of Condition-A versus H925 and Condition-A versus H1025 at impact speed of 300m/s are shown in Figure 4.28 and Figure 4.29, respectively. The incubation period of Condition-A is on average about 10 minutes long. H925 and H1025 have incubation time of about 18 and 10 minutes, respectively. At 300m/s, the distinction in the incubation periods of Condition-A versus H925 is clearly evident but is absent in the case of Condition-A versus H1025. The incubation period of H925 is about 1.8 times that of Condition-A and the incubation period of H1025 is the same as Condition-A. The maximum erosion rate is about 0.000450g/min for H925 (Figure 4.28) and is about 0.000575 and 0.000475g/min for Condition-A and H1025 respectively (Figure 4.29). At an impact speed of 300m/s, H925 has a better erosion performance compared to Condition-A in terms of incubation time and maximum erosion rate. Condition-A and H1025 have similar erosion performance in terms of incubation time and maximum erosion rate at impact speeds of 250 and 300m/s. H925 had a better erosion performance in terms of incubation time only at 250m/s as not much improvement was observed in the maximum erosion rate.

The evolution of erosion craters for impact speed of 300m/s in Condition-A versus H925 and Condition-A versus H1025 can be observed in Figure 4.30 and Figure 4.31, respectively. The erosion in H925 is initiated at the end of the maximum erosion rate stage in Condition-A (Figure 4.30). On the other hand, the erosion initiates and progresses simultaneously in Condition-A and H1025 (Figure 4.31). This makes the erosion performance of H925 better than Condition-A and H1025, which have similar performance at 300m/s.

An acceleration in erosion is observed at 300m/s (Figure 4.30 and Figure 4.31) when compared to the macrographs of 250m/s tests (Figure 4.26 and Figure 4.27) in each condition. This acceleration in erosion i.e. shortened incubation and increased erosion rate, is an effect of increase in impact speed as was discussed in section 2.2.1.

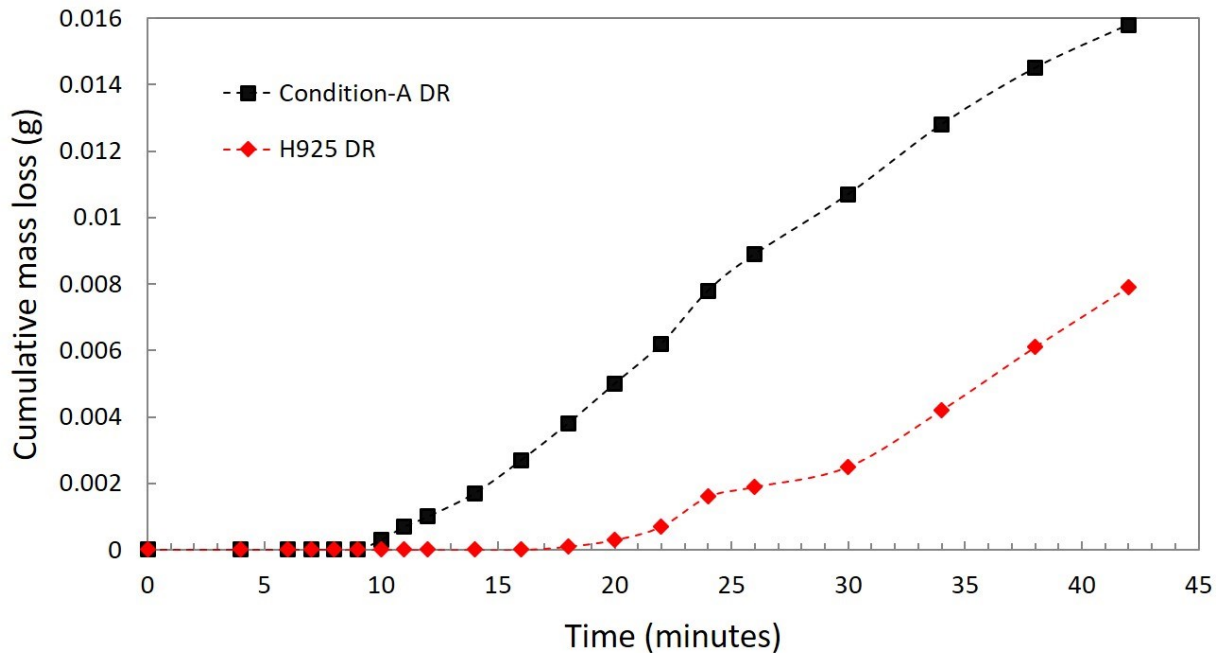


Figure 4.28 Erosion curves of Condition-A vs H925 with DR treatment at impact speed of 300 m/s.

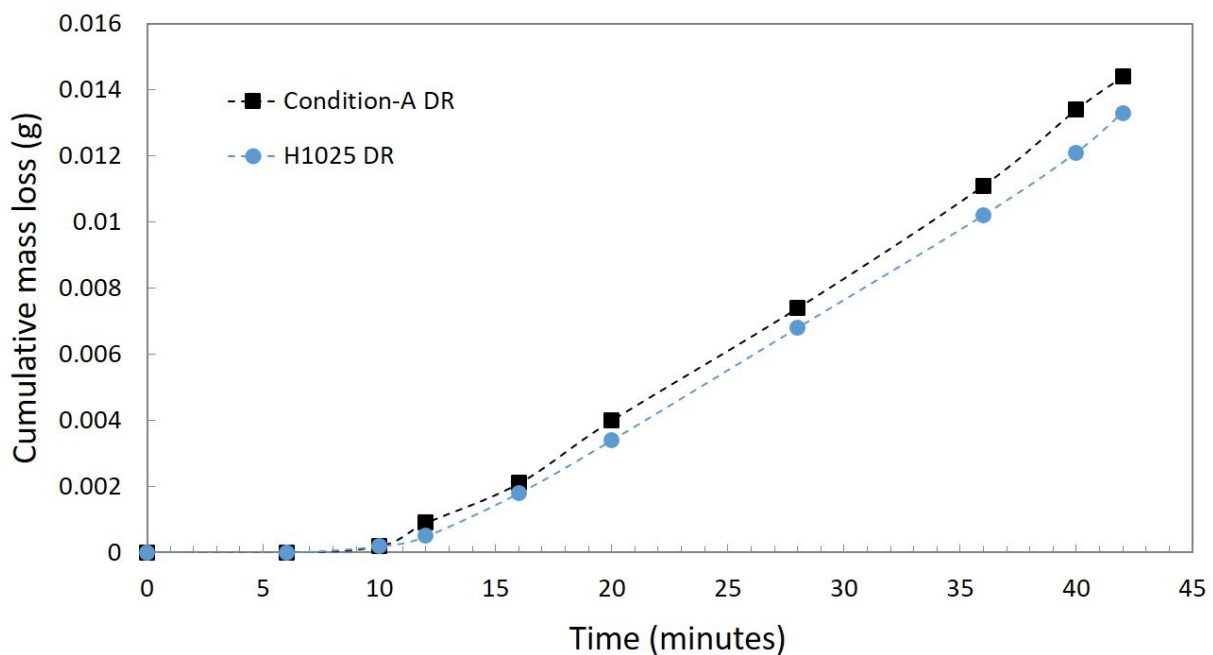


Figure 4.29 Erosion curves of Condition-A vs H1025 with DR treatment at impact speed of 300m/s.

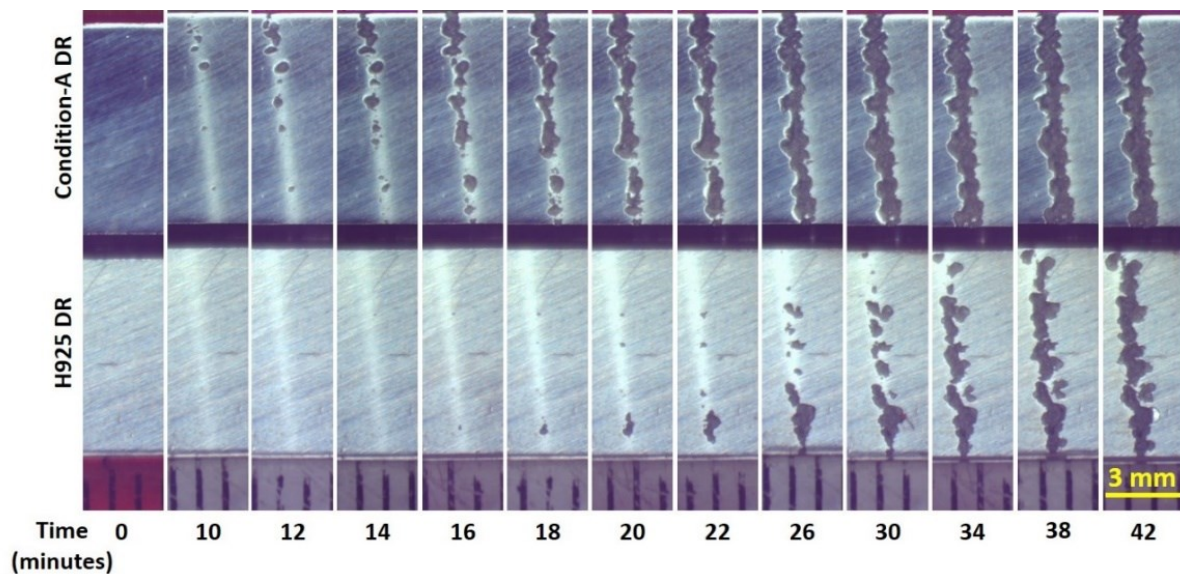


Figure 4.30 Evolution of crater in Condition-A DR versus H925 DR tested at 300 m/s.

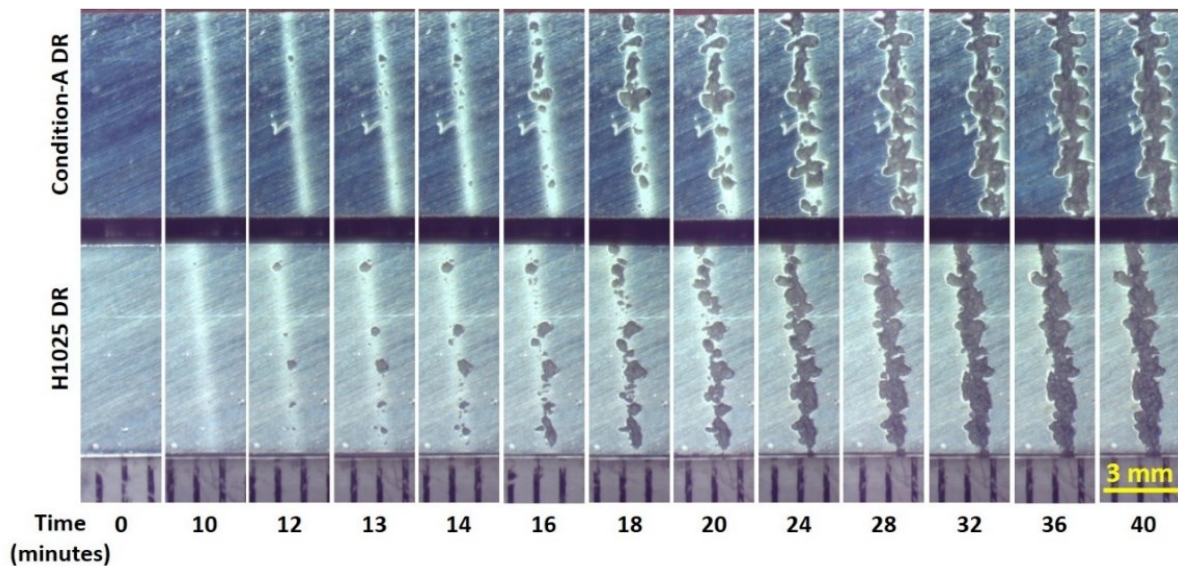
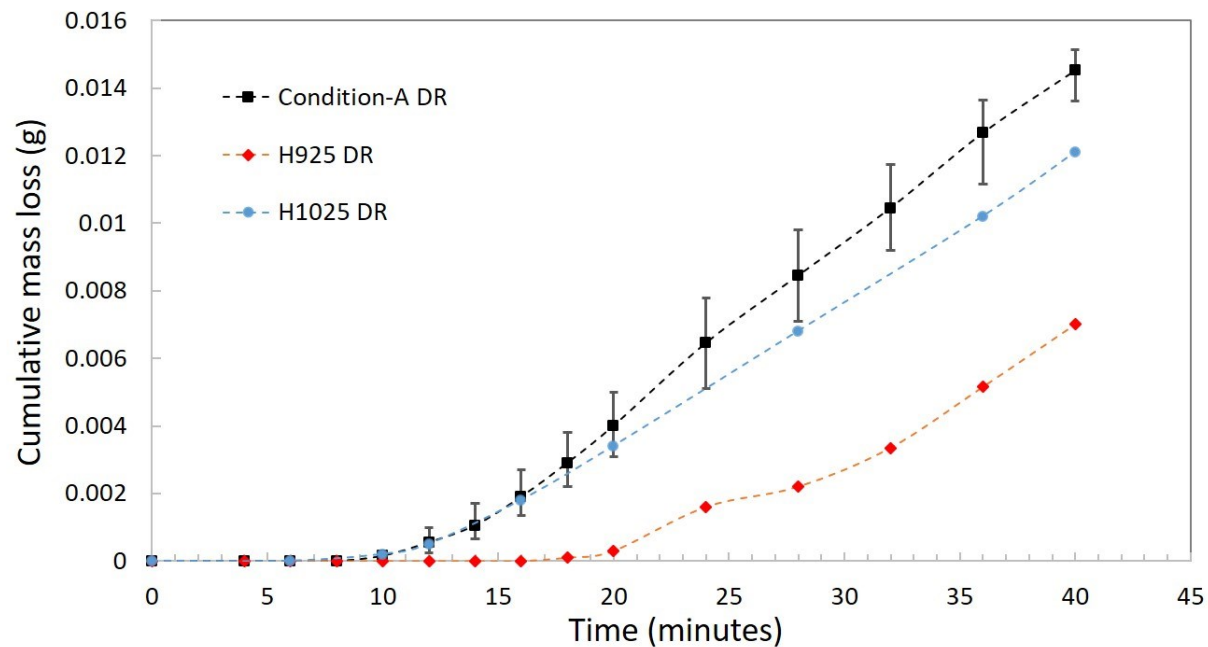
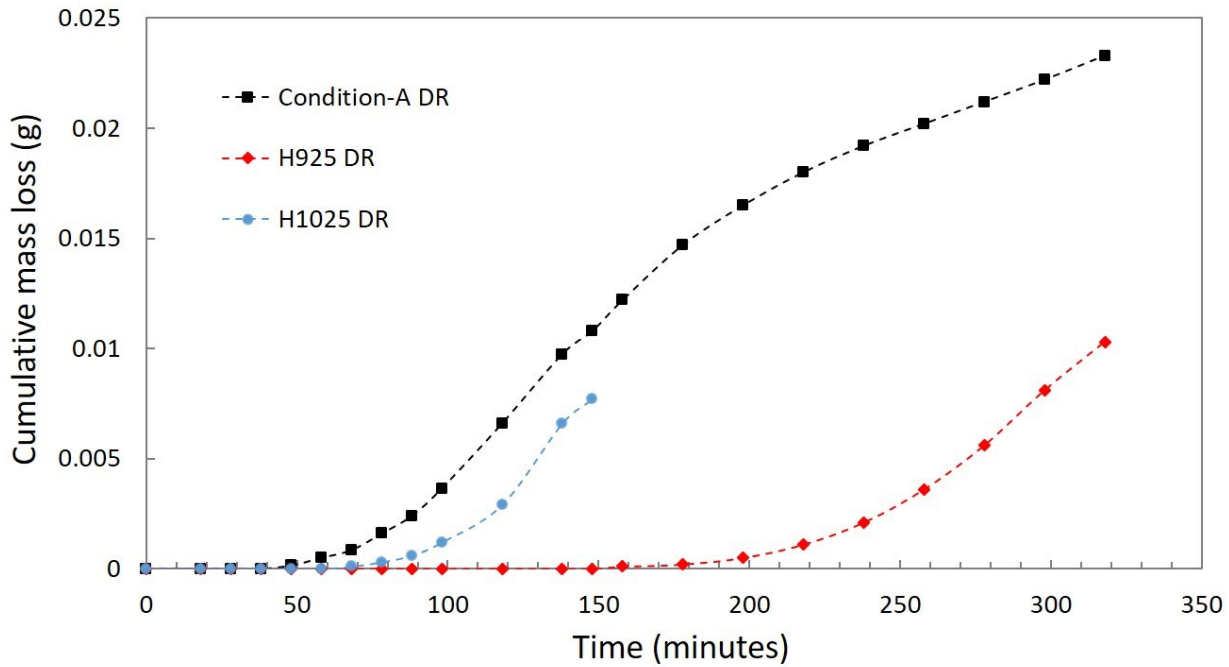


Figure 4.31 Evolution of crater in Condition-A DR versus H1025 DR tested at 300 m/s.

The erosion curves of DR treated samples at 250 and 300 m/s are summarized in Figure 4.32 and Figure 4.33, respectively. At 250 and 300m/s, the erosion behavior of DR samples is in the order of their strengths but disproportionately. The difference in erosion curves (incubation time and/or maximum erosion rate) with reference to that of Condition-A is clearly evident for H925 while there was no clear difference for H1025. Such qualitatively disproportionate behavior is also observed in the ground samples (section 4.5.2.1). In case of the DR samples, there is strain in addition to Compressive Residual Stresses (CRS) in the treated surface prior to WDE tests. This erosion behavior found in the DR samples is an effect of initial strain from cold work and the beneficial effect of CRS which are known to provide resistance to crack propagation. These issues are therefore considered further during the analysis of the DR samples.



Radar charts are plotted with various mechanical properties against the erosion incubation times for impact speeds of 250 and 300m/s. Figure 4.34 and Figure 4.35 show these radar charts plotted with Condition-A as a reference condition, so the variation in incubation time can be visualized with respect to the variation in their mechanical properties. Table 4-7 provides a summary of these observations. It should be noted that the strengths and elastic resilience shown in these charts are from the unstrained material i.e. before DR treatment. However, the surface micro-hardness is from the DR surface and is greater than that of the ground samples as reported in section 4.3. The strength and elastic resilience of both H925 and H1025 are greater than those of Condition-A. The micro-hardness of the DR treated surface in H925 and H1025 is also greater than that of Condition-A. But only the erosion resistance of H925 is found to be relatively greater. Although there is some improvement in the incubation time of H1025 with respect to Condition-A, it is not much considering its strength, elastic resilience and surface micro-hardness. This disproportionate behavior of H1025 with respect to other conditions is clearly discernible at both impact speeds. Similar disproportionate behavior of H1025 is experienced in the ground samples (section 4.5.2.1), indicating that the WDE behavior is influenced by the material properties of 17-4 PH steel in various conditions rather than by the DR surface treatment. As the WDE behavior gets complicated at the start of erosion, the analysis is primarily based on the incubation stage.

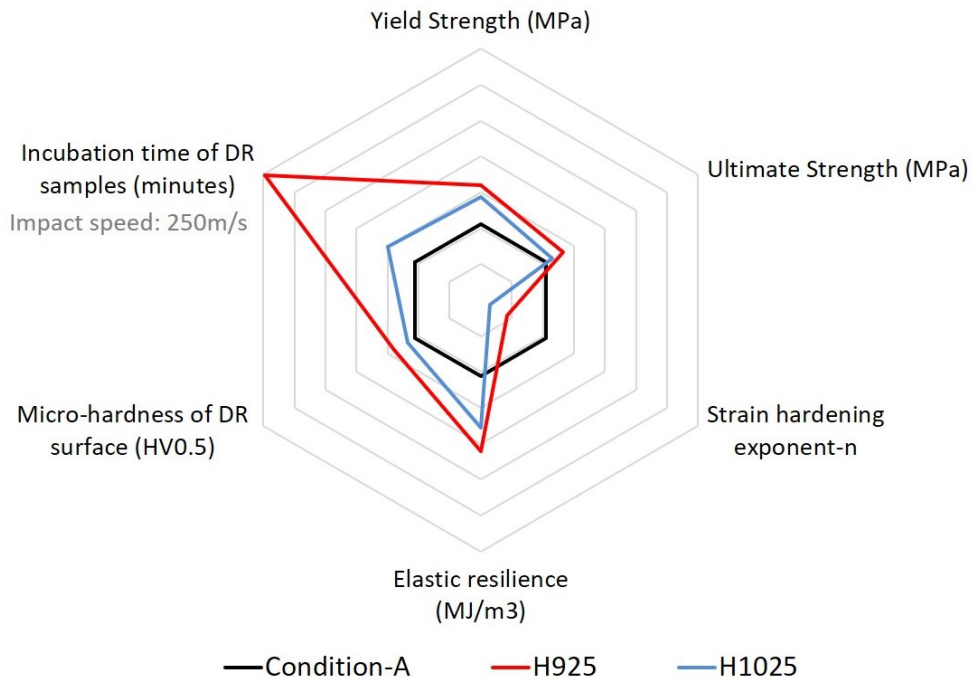


Figure 4.34 Radar chart showing erosion incubation time of DR samples tested at 250m/s and mechanical properties of each condition.

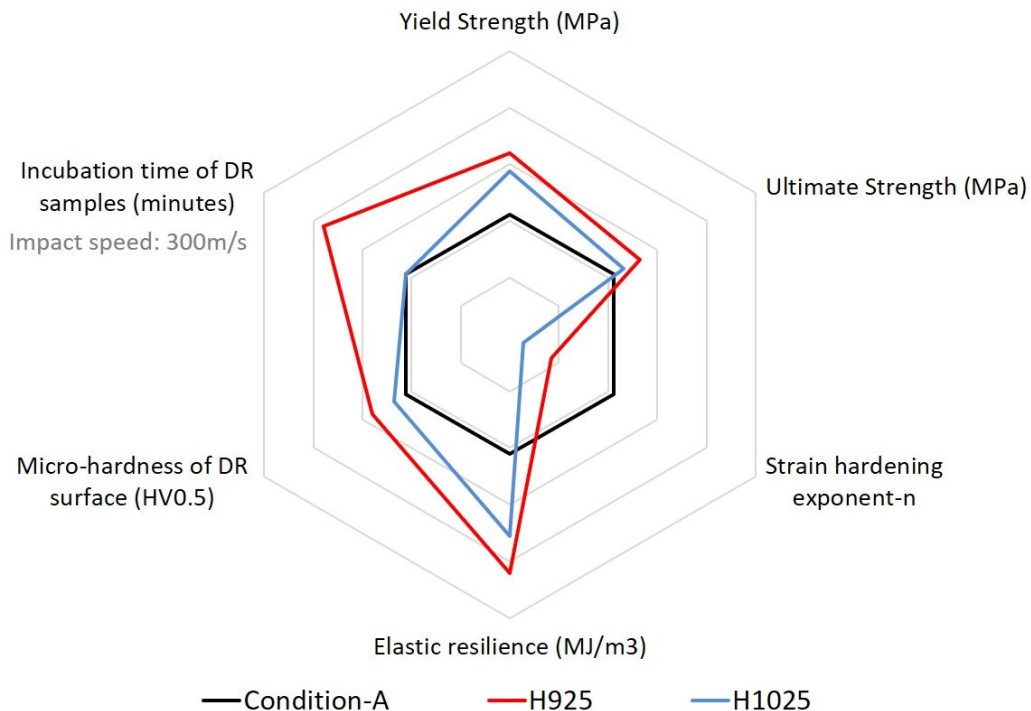


Figure 4.35 Radar chart showing erosion incubation time of DR samples tested at 300m/s and mechanical properties of each condition.

Table 4-7 Summary of relative properties and erosion performance of DR samples for each condition.

Condition	Yield Strength	Ultimate strength	Elastic resilience	Strain hardening exponent	Erosion performance (250m/s)	Erosion performance (300m/s)
Condition-A	Low	Low	Low	High	Low	Low
H925	High	High	High	Intermediate	High	High
H1025	Intermediate	Intermediate	Intermediate	Low	Low	Low

Similar to the analysis in section 4.5.2.1, the strain hardening behavior is analyzed for DR samples. A schematic which shows the difference in strain hardening behavior of the DR samples in each condition can be seen in Figure 4.36. The points A', J' and P' represent the new yield points in Condition-A, H1025 and H925 respectively after DR surface treatment. At these points, there is strain from the DR treatment and CRS in the material. The surface micro-hardness of the DR surface (Table 4-2) is greater than that of the ground surface (Table 4-2) in each condition, which confirms the occurrence of strain hardening in the treated surface. When exposed to droplet impacts, further strain is developed in the material depending on the resistance provided by the strain hardening, elastic resilience and the beneficial CRS. As discussed for ground samples (Figure 4.23), the elastic resilience energy is dissipated after each impact cycle and the strain is developed when the impacting energy exceeds the resilience energy. When the DR samples in each condition were exposed to the same number of droplet impact cycles (N), the strain causes their yield points to shift towards their fracture point. For instance, the yield point could progressively shift from A' to B', from J' to K' and from P' to Q' in Condition-A, H1025 and H925 respectively after the N cycles of droplet impacts (Figure 4.36). The shift observed in the yield points by distances x', y', and z', in the graph for

Condition-A, H1025 and H925 respectively, is governed by the magnitude of the yield strength, elastic resilience and beneficial CRS at each cycle of impact.

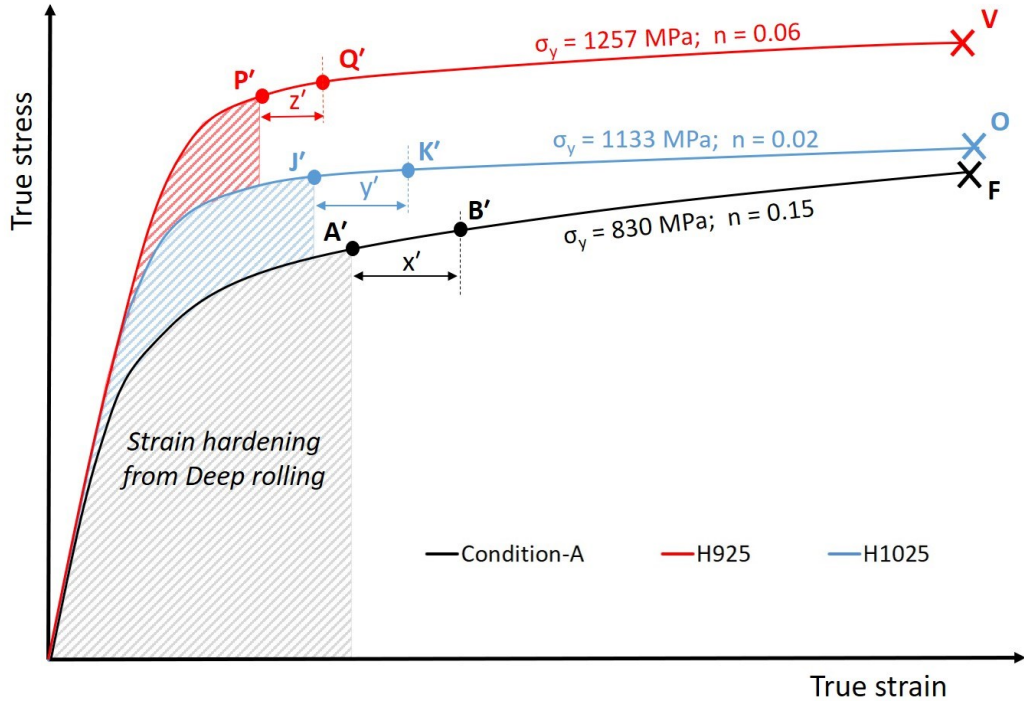


Figure 4.36 Schematic showing progression of yield point due to strain in DR samples.

This added strain is believed to contribute to a decrease in erosion resistance as the amount of strain required to failure is decreased [39]. The beneficial CRS should have aided in resisting erosion as no decrease in the incubation time is observed with the DR treatment. When starting from the same point on respective curves (Figure 4.23 and Figure 4.36), the resistance provided by the material is greater in DR samples than in the ground samples due to the presence of CRS. This means, the progression of yield point towards fracture is slower in DR samples than in the ground samples for the same cycles of droplet impacts. Therefore, the incubation time of DR samples is greater or comparable to that of ground samples despite having some initial strain from the DR treatment.

Considering the strain and the beneficial CRS from the DR treatment in addition to tensile properties, it can be concluded that the erosion behavior during the incubation time is dominated by the mechanical properties of the material. The identical performance of Condition-A and H1025 is due to lower strength and greater n-value of Condition-A as opposed to greater strength and lower n-value of the H1025 condition. The superior erosion performance of H925 is due to its greater strength and resilience and also because of work hardening. The CRS provides additional resistance to that strain hardening. While it is known that work hardening increases both the strength and brittleness in metals, it can be inferred from these results that the contribution of strain hardening in resisting erosion is greater than the contribution of embrittlement in accelerating the erosion.

4.5.2.3. Effect of the DR treatment

The erosion performance with and without the DR treatment in each condition has been evaluated as discussed in sections 4.5.2.1 and 4.5.2.2. The effect of the DR surface treatment is observed by comparing the incubation times and the maximum erosion rates in the ground (without DR treatment) and DR samples. The results of the incubation time and the maximum erosion rate at 250 and 300m/s with and without the DR treatment are summarized in Table 4-8. Generally, an improvement in the incubation time at the expense of an increased maximum erosion rate is observed with the DR treatment. At 250m/s impact speed, an increase in the incubation time with the DR treatment can be observed but an increase in the maximum erosion rate with the DR treatment is negligible in each condition. The incubation time is increased by about 10, 60 and 15 minutes in Condition-A, H925 and H1025, respectively. At an impact speed of 300m/s, the increase in incubation time with the DR treatment is not visible in Condition-A and H1025 but only visible in H925. A relatively significant increase in the

incubation time of about 6 minutes was observed in H925 with the DR treatment, but an increase in the maximum erosion rate with DR treatment is clearly visible in each condition. An increase in the maximum erosion rate of 0.000075, 0.0001 and 0.000065g/min was observed in Condition-A, H925 and H1025, respectively.

With the increase in impact speed from 250 to 300m/s, the difference in the incubation time is diminished. There could perhaps be small differences in incubation time which are not captured due to the relatively large cycle time used in the 300m/s tests. The acceleration in erosion due to the increase in impact speed diminishes the differences in the incubation time of 17-4 PH steel. On the contrary, the difference in the maximum erosion rate is increased with an increase in impact speed. Such effects were also observed in UNSM treated samples with an increase in impact speed by Gujba et al. [55]. Beyond the incubation stage, various other erosion mechanisms come into play. In addition to mechanical properties, the erosion pit shape and dimensions play an important role in erosion [106]. Since the differences in incubation time are not noticeable at 300m/s, only the 250m/s erosion test curves of ground and DR samples are superimposed to observe the effect of the DR treatment.

Table 4-8 Summary of incubation times and maximum erosion rate in DR and ground samples.

Test speed	Condition	Without DR treatment		With DR treatment	
		Incubation time (minutes)	Maximum erosion rate (g/min)	Incubation time (minutes)	Maximum erosion rate (g/min)
250m/s	Condition-A	38	0.000097	48	0.000148
	H925	98	0.000085	158	0.000111
	H1025	53	0.000095	68	0.000120
300m/s	Condition-A	10	0.000500	10	0.000575
	H925	12	0.000350	18	0.000450
	H1025	10	0.000410	10	0.000475

The erosion curves of the ground and the DR conditions at 250m/s impact speed are superimposed to visualize the observations already made in Table 4-8. Figure 4.37, Figure 4.38 and Figure 4.39 show superimposed erosion curves of the ground and the DR samples in Condition-A, H925 and H1025 respectively. The erosion starts later in the DR samples but they erode with a greater erosion rate. This causes the erosion curves of the DR samples to cross those of the ground samples. It is observed that the erosion curves of the DR and ground samples in Condition-A and H1025 are similar in nature despite some slight differences in the incubation time and maximum erosion rate. The initial difference is relatively large and discernible in the case of H925, but the ground and DR curves seem to intersect one another during the maximum erosion rate stage. This makes the overall WDE behavior till the end of the maximum erosion stage in the DR treated samples similar to that in the ground samples in each condition. The DR treated samples are further investigated by scrutinizing the SEM micrographs at various stages to check for dependence of erosion mechanisms on the surface condition of the 17-4 PH steel.

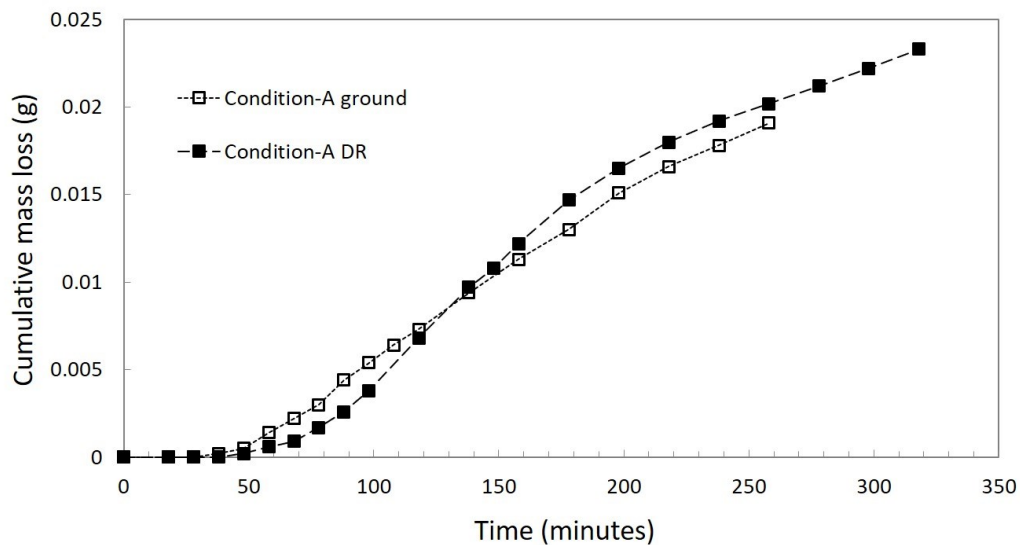


Figure 4.37 Superimposed erosion curves of ground and DR samples in Condition-A at 250m/s impact speed.

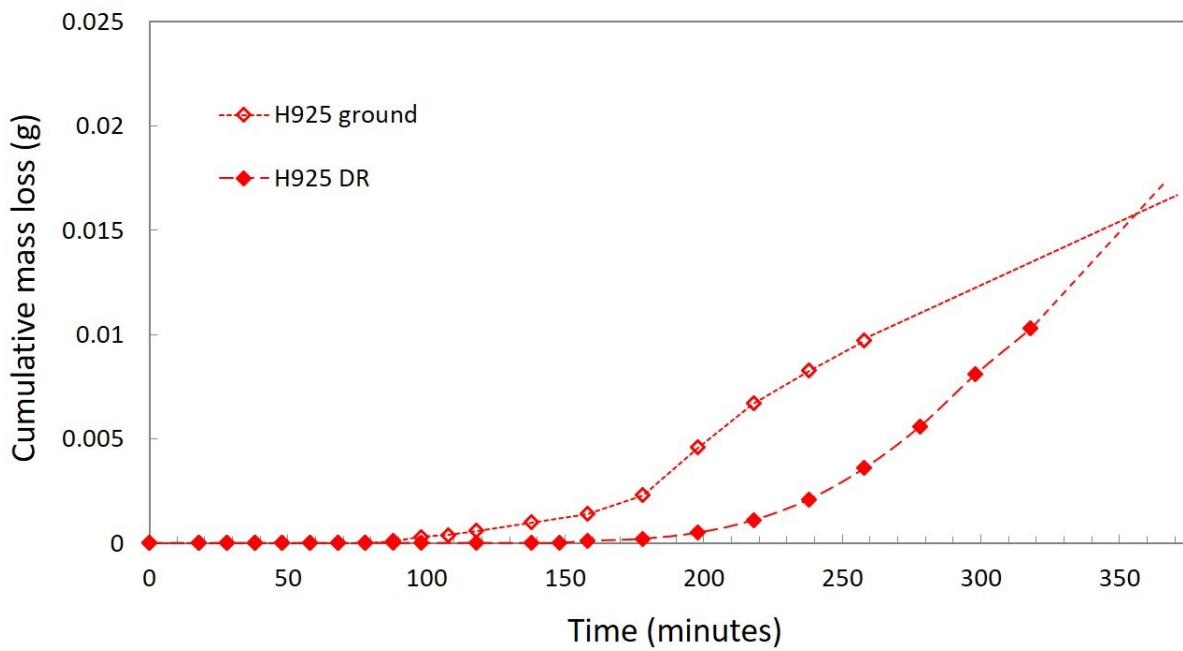


Figure 4.38 Superimposed erosion curves of ground and DR samples in H925 at 250m/s impact speed.

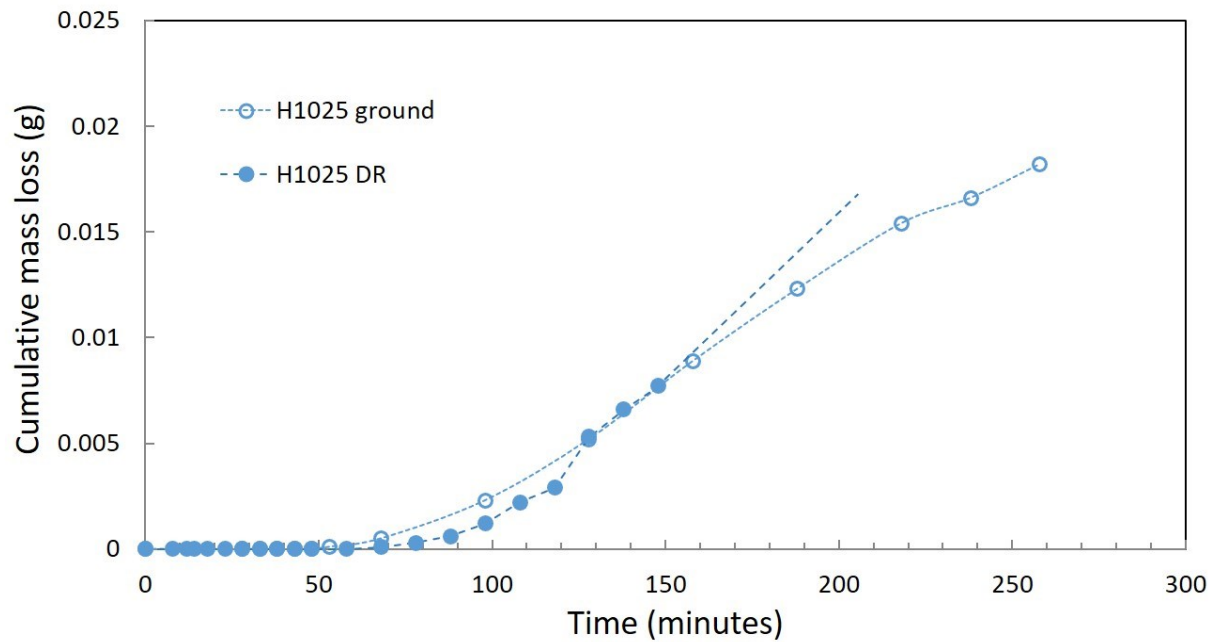


Figure 4.39 Superimposed erosion curves of ground and DR samples in H1025 at 250m/s impact speed.

It is to be noted that the surface roughness of the ground samples is finer than that of the DR samples as discussed in section 4.4. The deep rolled surface was examined at the end of the incubation stage in each DR sample. The surface was marred by plastic deformation lines formed by deep rolling along the rolling direction. Due to the droplet impacts, micro-pits are formed preferentially at the wider deformation lines which tend to grow in width transverse to the rolling direction as shown by arrows in Figure 4.40. In the absence of such wide deformation marks in the ground samples (Figure 4.8), it is expected that the ground samples have an advantage in delaying the start of erosion. Nevertheless, considering that the number of such wide deformation marks is not too high in each sample, their effect on the DR samples can be safely neglected.

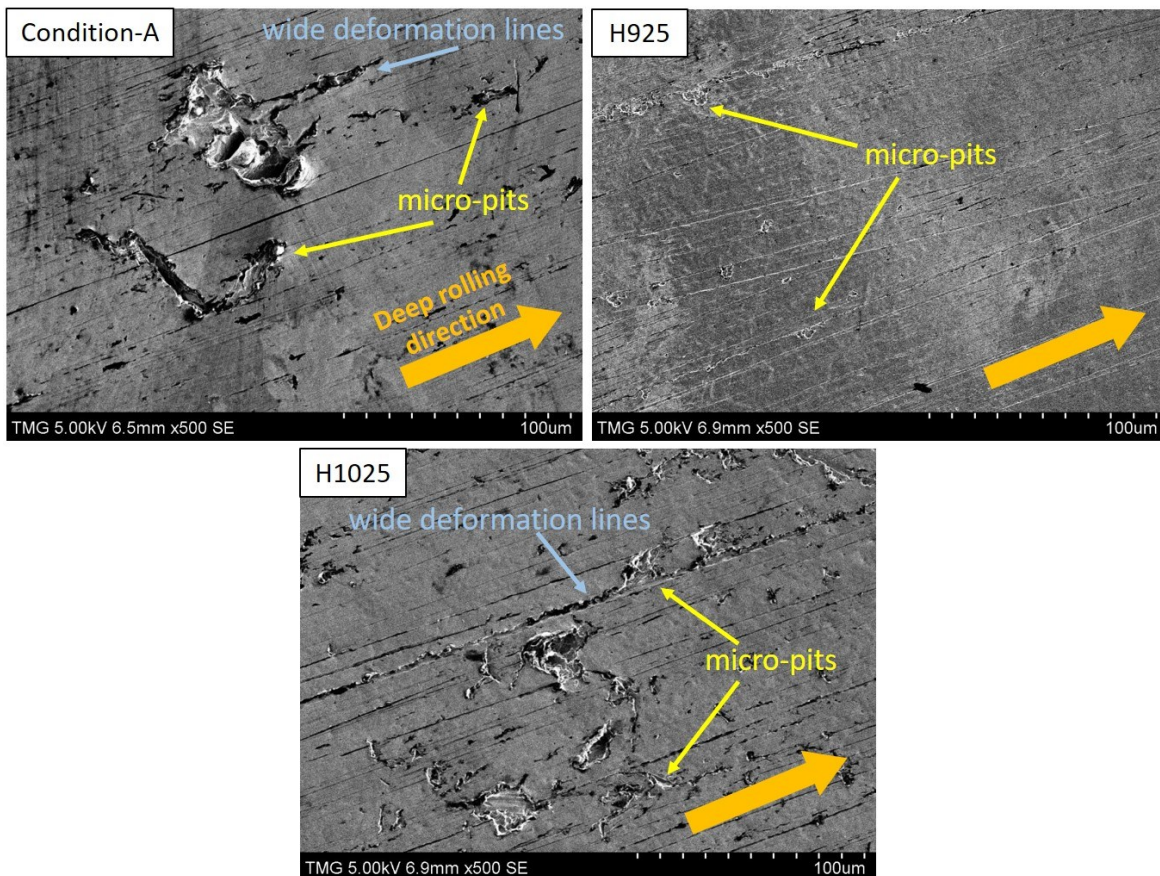


Figure 4.40 Preferential micro-pit formation on the deep rolled surface at the end of incubation period.

The modified region at the DR treated surface [76]–[79] provides potential sites for reflection of stress waves generated at impact. The impact loading together with the lateral jetting causes some shallow micro-pits to form. Such micro-pits from erosion on the treated surface were also observed by Ma et al. [41]. However, brittle cracks were seen in the DR surface exposed to erosion tests and was attributed to work hardening from droplet impacts [41]. The absence of such surface cracking in the current DR treated samples is likely due to the low strain hardening exponent of 17-4 PH stainless steel. The impact loading of 17-4 PH stainless steel provides favorable conditions for transgranular fracture [88]. Transgranular fracture is observed predominantly in micro-pits in each DR sample as shown in Figure 4.41. In the acceleration stage, pits grow rapidly and coalesce predominantly by intergranular fracture as shown in Figure 4.42. As the freshly exposed surface from fracture is struck by subsequent droplet impacts, it is deformed until further cracks are generated causing the material to break away as chunks. Severe plastic deformation is observed in the periphery of the pits and is referred to as material folding. Similar plastic deformation was observed by Ma et al. [41] and Gujba et al. [50] and was attributed to the shear waves from lateral jetting of liquid. However, the micro-pit formation and pit growth mechanism observed in the current work for each condition is the same.

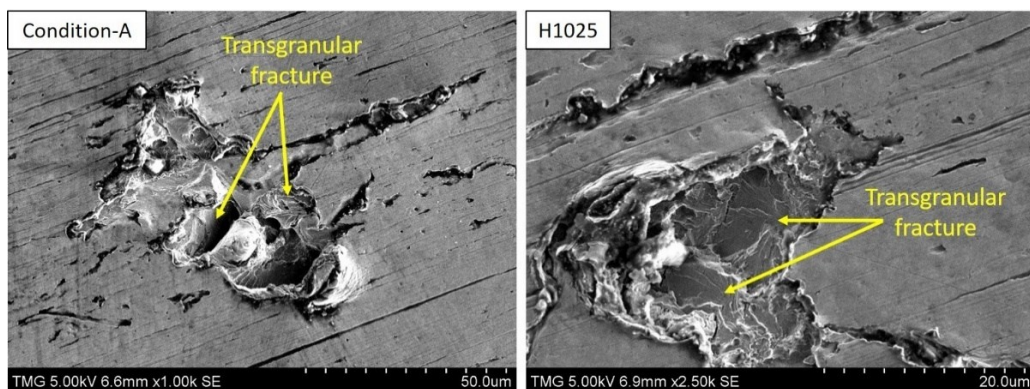


Figure 4.41 Transgranular fracture in micro-pits.

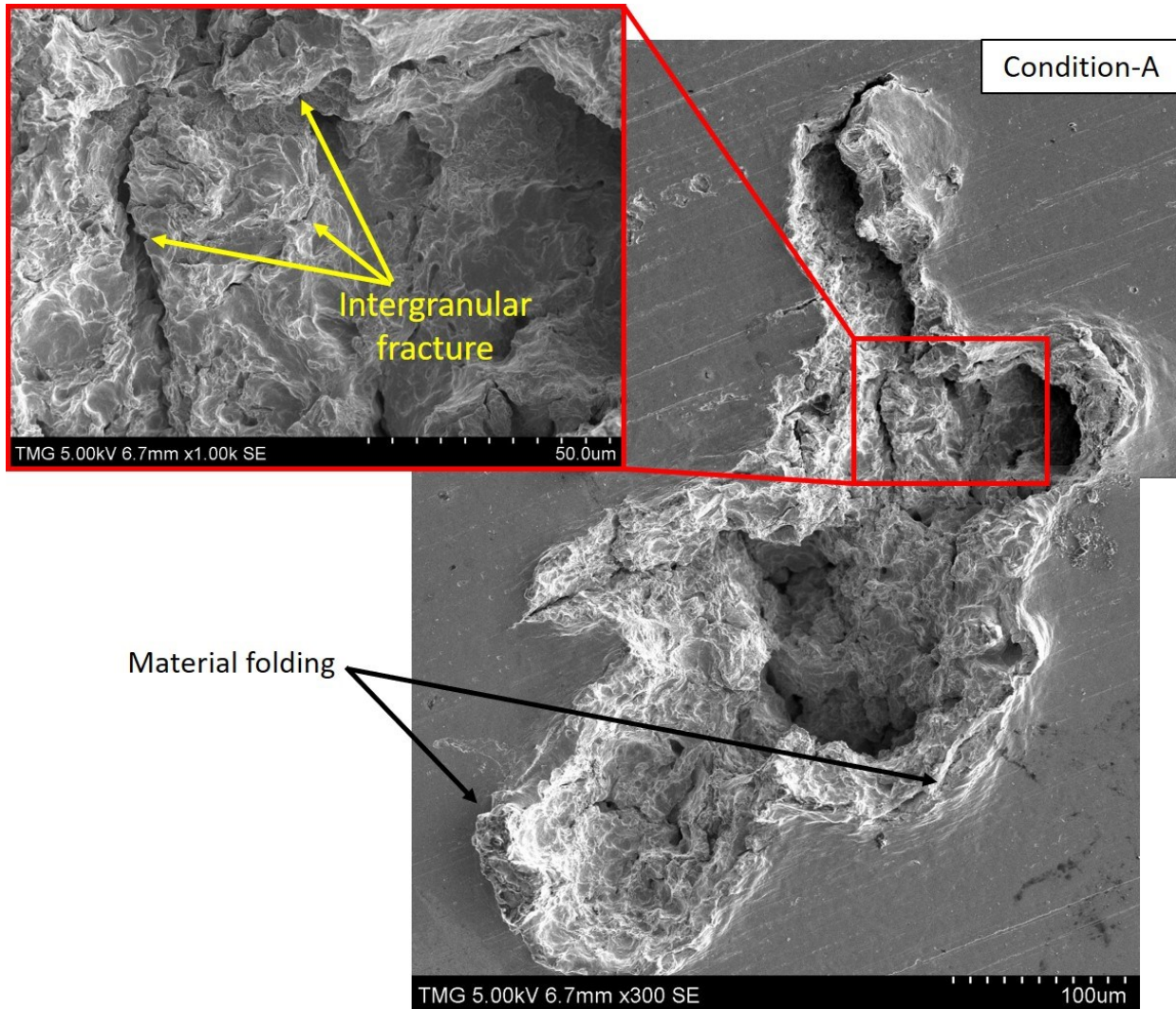


Figure 4.42 Pit growth by intergranular fracture and material folding.

Under favorable conditions, the material folding also results in the upheaval of material.

In the presence of subsurface cracks, the shear waves and lateral jetting generated at impact causes the upheaval of material at the surface [42], [50], [51], [108]. Material upheaval is seen in the periphery of the expanding crater and is away from the crater as shown by Figure 4.43. The subsurface cracks grow in size originating from the erosion pit and into the material until it removes a large chunk of strained material under the action of expanding liquid [15]. This mechanism of material removal is observed in each condition and it ensues when the conditions

are suitable during erosion. The occurrence of material upheaval mechanism was found to be independent of the condition of the material.

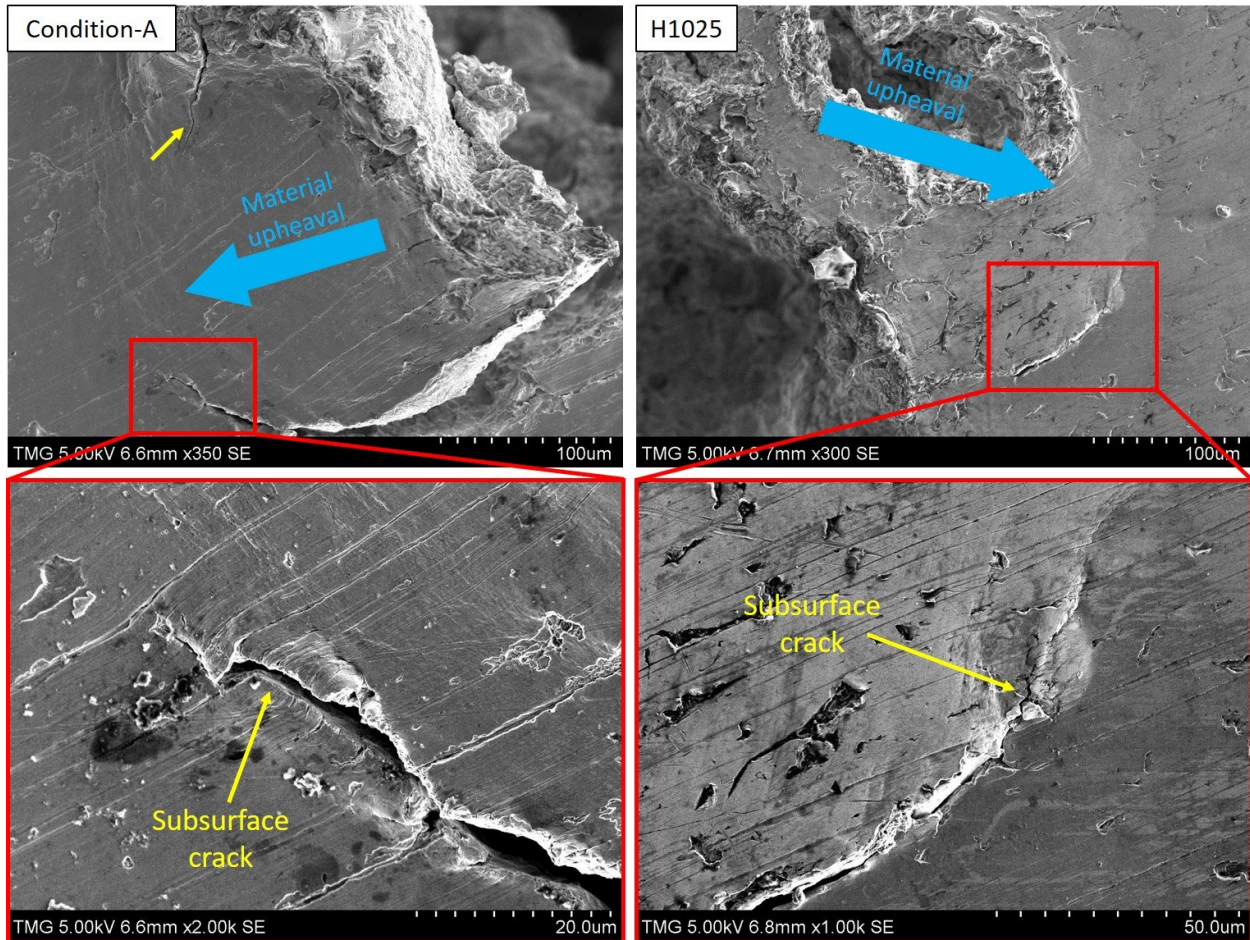


Figure 4.43 Material upheaval and subsurface cracks during crater expansion from erosion.

In the advanced stages of erosion, the surface created by erosion makes the stress wave propagation and impact pressure generation even more complex due to multiple contact points on each droplet and various relief mechanisms at droplet impact [54], [106]. When droplets impact over an erosion crater, the liquid enters cavities with great pressure as it tries to expand and results in tunneling due to hydraulic penetration [51], [53]. With subsequent droplet strikes, the network of pre-existing tunneling cracks grows, and chunk of material is knocked off when they coalesce. The deep pockets in an erosion crater, often beyond the reach of direct droplet

impacts, are created by removal of material majorly through hydraulic penetration. The fractured surface of these pockets was plastically deformed and filled with cracks due to subsequent impacts. This mechanism of material removal and deformation was observed in each condition, as shown in Figure 4.44, signifying no observable change in erosion mechanism. One of the deep pockets was pictured in a sectioned DR sample shown in Figure 4.45. Such deep pockets, formed despite being shielded from direct droplet impacts by overhanging material, are a proof of the extent of damage that hydraulic penetration can cause. The overhanging material is however weakened by internal cracks as shown by the magnified micrograph. These cracks lead to fracture and removal of chunks of overhanging material with subsequent impacts.

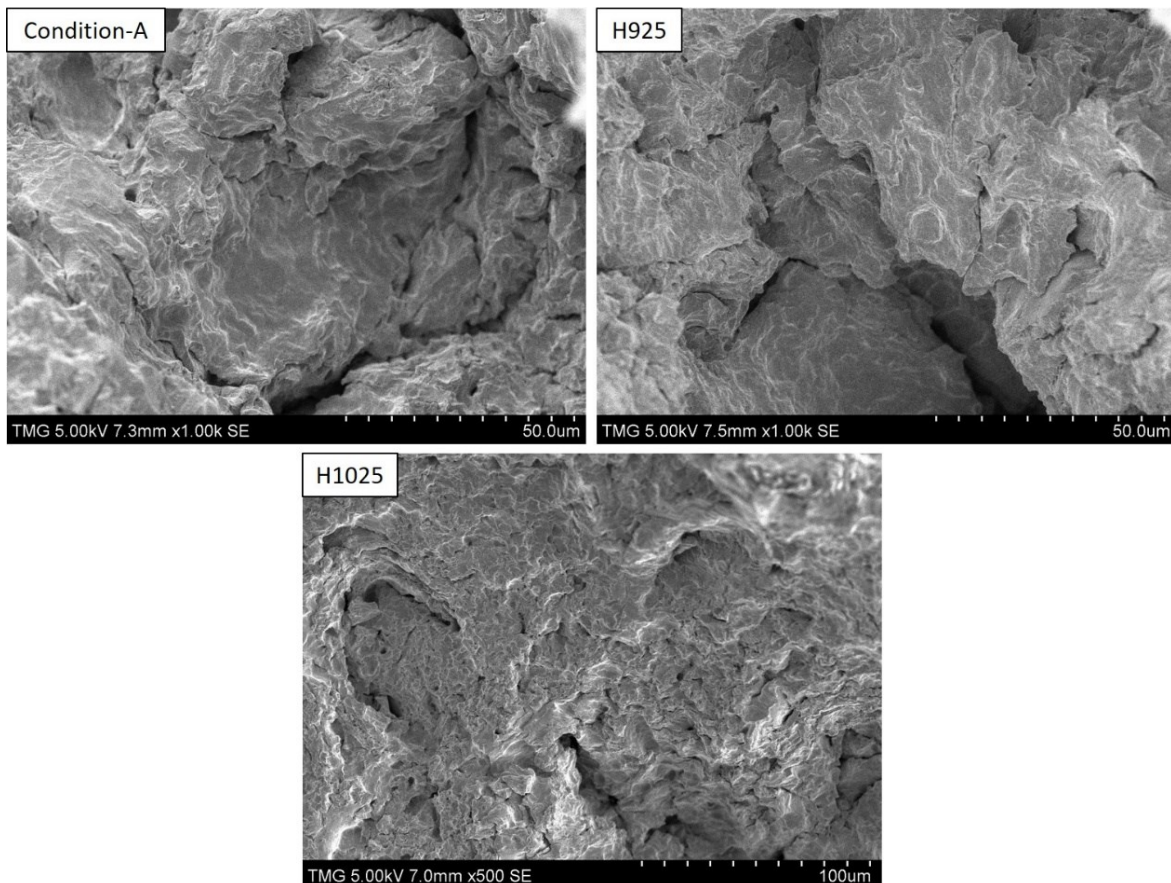


Figure 4.44 Deformed surface in the deep pockets with grain boundary cracks.

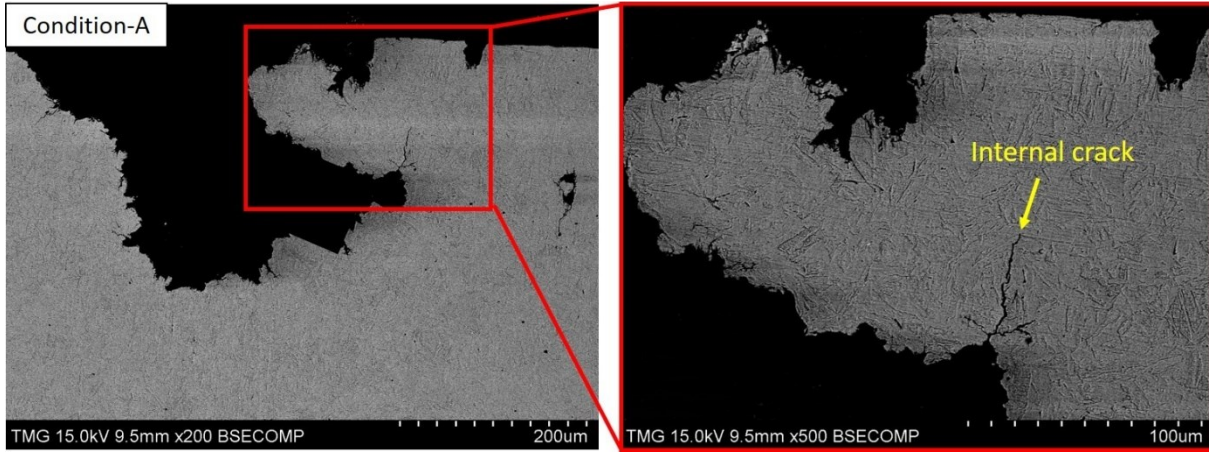


Figure 4.45 Section showing internal crack in the overhanging material above deep pocket.

The sections of the DR samples in each condition are examined to check if there are any differences in crater behavior. As observed earlier, the expansion is dominated by hydraulic penetration. Lateral subsurface expansion of the crater through tunneling is captured in Figure 4.46. In each condition, a vast network of tunnels is found around the subsurface crater which explains how the erosion crater grows in the lateral direction. The presence of a large number of tunnels before failure shows that there is perhaps some resistance to the tunnel growth due to some microstructural features. Robinson et al. [52] concluded that the martensite lath microstructure constrained the tunneling by hydraulic penetration in Ti-6Al-4V during WDE. The similar lath martensitic matrix, as observed in section 4.1, ensures such resistance is experienced in each condition. As the erosion continues, the crater growth is limited to a specific depth and the sample mass loss starts to decelerate. Perelman [106] attributed the deceleration in mass loss to the loss of impact energy due to the relief mechanism. The relief is provided in the form of dissipated impact energy from the jagged surface of the erosion crater [106]. As there is no observable difference in the erosion surface appearance and the crater dynamics among all conditions, it can be inferred that the influence of relief mechanism is

similar among all the conditions. It can be concluded that the general erosion mechanisms are the same for the conditions studied in this work.

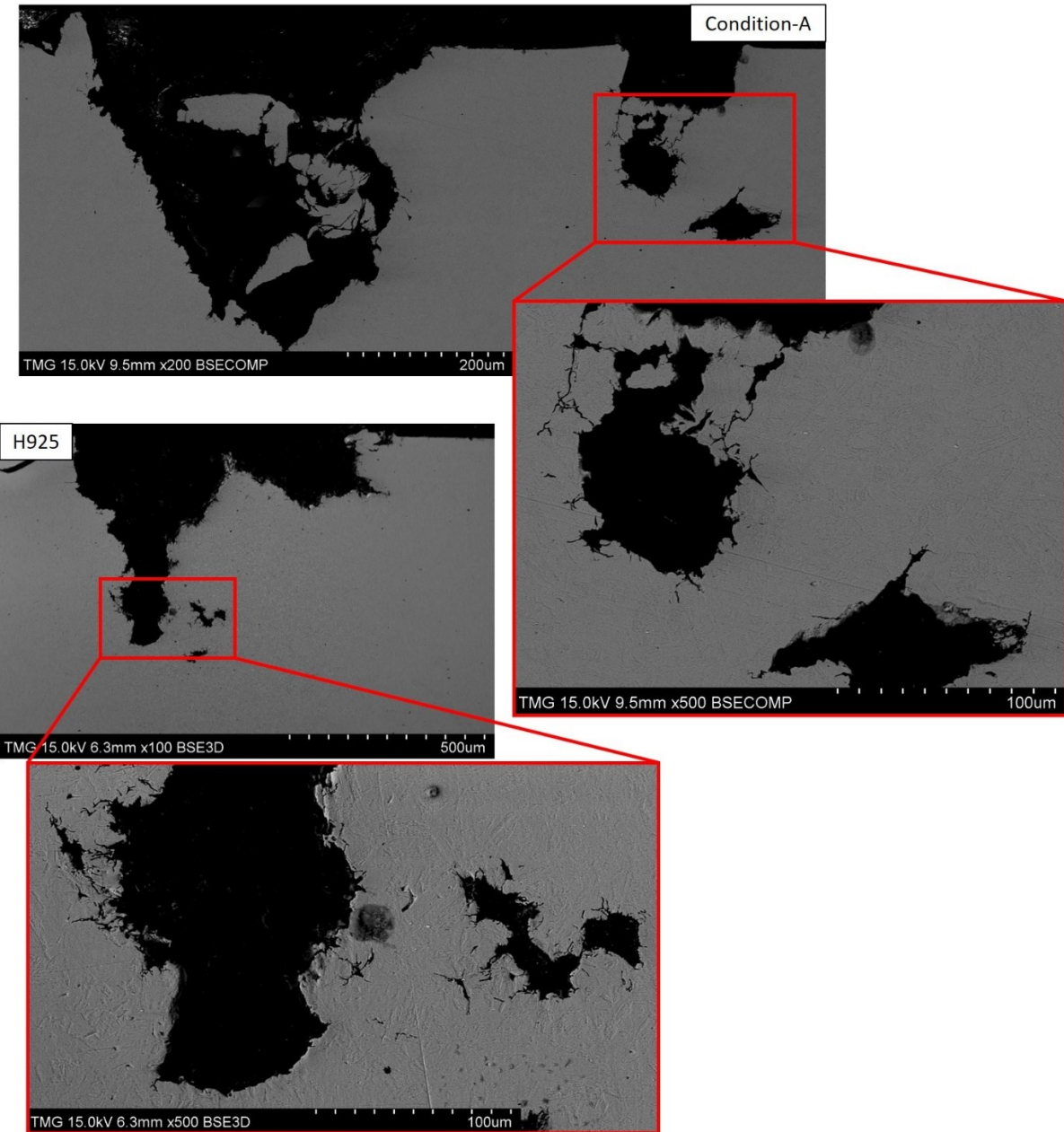


Figure 4.46 Section showing subsurface expansion of erosion crater by tunneling.

In the light of similarities in erosion mechanisms observed among all conditions, it can be concluded that the WDE behavior observed through erosion curves is a result of mechanical properties of each condition.

4.5.3. Stress relieving results

The effects of strain hardening in the material due to the droplet impacts and the DR treatment on the overall erosion behavior are discussed in the previous section. It was observed that the accumulated strain brings the material closer to fracture. The induced strain accumulated from droplet impacts in erosion has not been extensively studied in the WDE literature. For this reason, the effects of removing the accumulated strain on erosion performance during the initial stages of WDE is investigated to better understand the strain hardening results.

The tests were therefore designed to intermittently relieve the accumulated impact strain at selected intervals. As mentioned in section 3.1, X22CrMoV12-1 stainless steel was used to conduct the stress relieving experiments. The terms stress relieving and strain relieving are used interchangeably in this work as they are the same in effect. A standard 460 μm droplet size and impact speed of 300m/s was used in these experiments. The uniformity in surface finish is ensured by grinding the test surface of each sample with 1200grit SiC paper. The uniformity in the starting condition of each sample is maintained by stress relieving both samples once before the start of a WDE test. Each test is conducted to evaluate the erosion behavior of a test sample, which is intermittently relieved of accumulated strain, versus the reference sample. The effects of relieving are studied by varying the WDE test interval after which the test samples are relieved (i.e. the cycle time). The test samples in the SR-1 test were relieved after 2 minutes of erosion and the ones in the SR-2 test were relieved after 30sec of erosion. The WDE test is interrupted to measure the weight of the samples and to relieve the strain in the test sample by heating them to 680°C for 75 minutes (stress relieving temperature and time, respectively). The test sample is air cooled before continuing the test. This procedure constitutes a single cycle in

an erosion test, which is represented as a data point in the erosion curve for each sample. For each test, there are two erosion curves, one for each sample. Having a reference sample allows a comparison when evaluating the performance of a relieved test sample from the same test. On the other hand, the curves from different tests can only be qualitatively compared to evaluate the change due to mainly changing the frequency of the stress relieving process.

The erosion curve of the SR-1 test is shown in Figure 4.47. The incubation time for the SR-1 samples is about 8 and 10 minutes respectively for the relieved test sample and the reference sample. The difference, although shown as 2 minutes from the curves, could have actually been smaller and has not been captured due to the larger cycle time of 2 minutes.

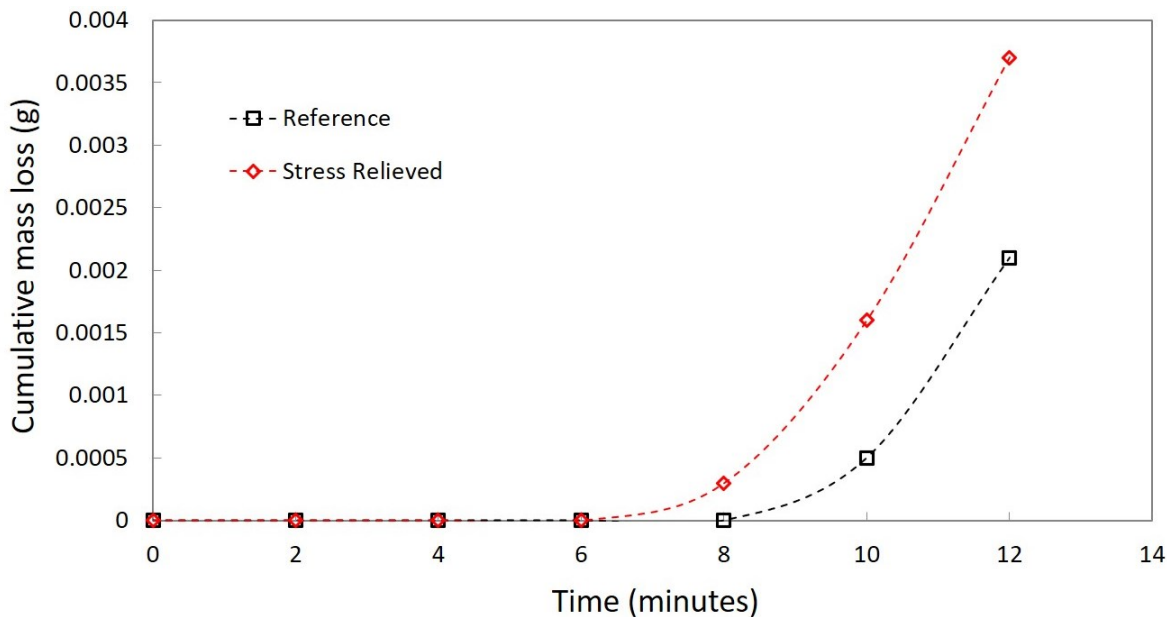


Figure 4.47 Erosion curves of SR-1 test at impact speed of 300 m/s.

However, the slope of the curve during their maximum erosion rate is the same for the SR-1 test. In the SR-2 test, the relieved test sample also eroded earlier than the reference sample, but the rate of erosion is clearly slower in the relieved test sample compared to the reference sample as shown in Figure 4.48. The early start of erosion in the relieved test samples

could be due to a reduction in their strength due to repeated stress relieving; On the other hand, the strain hardening in the reference sample resists the creation of further strain as discussed in section 4.5.2.1.

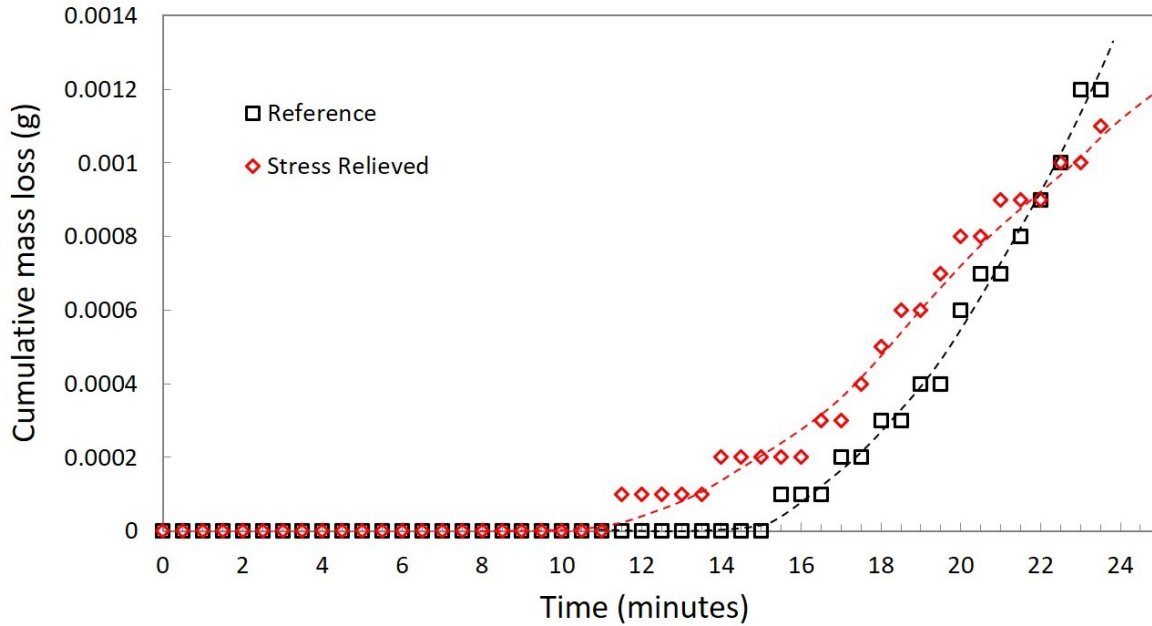


Figure 4.48 Erosion curve of SR-2 test at impact speed of 300 m/s.

The reduction in strength of the relieved samples can be concluded from the reduction in micro-hardness by the end of the stress relieving experiments, as discussed in section 4.3. The evolution of pits in the samples of the SR-2 test is shown in Figure 4.49. It can be observed that the relieved test sample starts to erode at about 10 minutes from the top edge of the sample. It is worth noting that the edge effect could have played a role in the early start of erosion in the test sample. The edge effect can be described as when the pitting initiates too close to the edge in one of the samples, as there is not enough material to resist from one side, the material at the edge caves outward and erodes quicker than in the interior. It causes an early mass loss in the sample with an edge effect and hence the possibility of a false start. The cumulative mass loss is about 0.0006 and 0.0004g in the test and relieved samples, respectively, at 19minutes. The

difference in pit growth is also observed later, especially after 19 minutes. The pit size and the number of pits in the reference sample can clearly be seen growing rapidly in comparison to the relieved test samples. This explains the different slopes of erosion curves in the samples after the start of erosion. Even though the pits were formed in the relieved test sample earlier than in the reference sample, the growth rate of pits in the reference is much greater than in the test sample. At about 22 minutes, the cumulative mass loss is 0.0009g in each sample and the curves cross each other; the erosion mass loss in the reference sample is greater than in the test sample beyond this point.

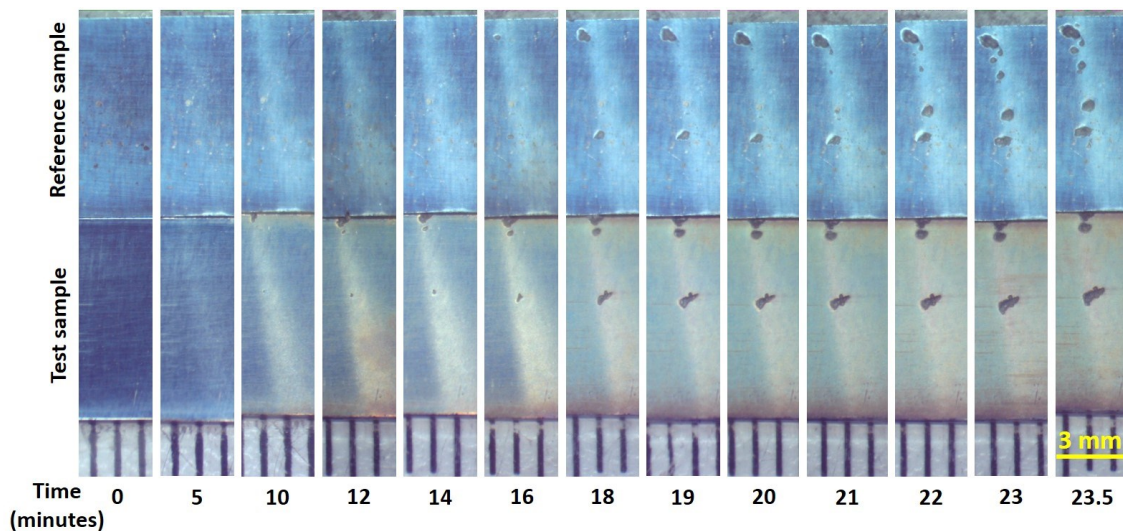


Figure 4.49 Macrographs showing pit progression in SR-2 test samples.

The accumulated strain from droplet impacts is more frequently relieved in the SR-2 test. There is more accumulated strain in the reference sample than in the relieved test sample. Also, the strength of the relieved test sample is slightly lower than the reference sample as observed in section 4.3. After the start of erosion, the erosion curves of the SR-2 test intersect. As the erosion rate is smaller in the relieved test sample, even with the lowered strength, it can be said that the accumulated strain in the reference sample contributes to the acceleration of erosion.

Rieger [43] performed a WDE test similar to the SR-1 test on pure aluminum to study the erosion damage mechanisms. The purpose of this study is to see if the removal of the accumulated strain can delay the erosion process. It was however observed that the relieved aluminum samples eroded significantly earlier than the untreated reference sample [43]. The tempering temperature of 510°C was used on pure aluminum samples, which is well above the recrystallizing temperature [109]. This must have changed the grain size and strength in addition to the implied reduction in dislocation density in the test sample. Hence, a large difference was observed in the erosion incubation time of the relieved and the test samples [43].

The role of strain developed from droplet impacts on the WDE behavior is further investigated by observing the SEM micrographs of the pits as they evolved in the reference and stress relieved test samples of the SR-2 test. Only the SR-2 test is chosen for further investigation as it is more likely to show differences due to its greater frequency of stress relieving than the SR-1 test.

4.5.3.1. Damage mechanism in the SR-2 samples

The pit size growth is found to be greater in the reference sample compared to the test sample. While the difference in number of pits is seen in the macrographs (Figure 4.49), the difference in the growth of pit size in the SR-2 test can be clearly seen in Figure 4.50. From 16 to 23 minutes, the pit in the interior of the relieved sample barely grew in size as the pit in the reference sample grew by a few times its size. The pit formed due to the edge effect in the relieved test sample did not grow in size. The growth of this pit is slower due to the lower impact energy it takes compared to the pits in the interiors. As the pit is open on one side, it does not allow the impacting droplets to fully impart the energy as some of it is dissipated out.

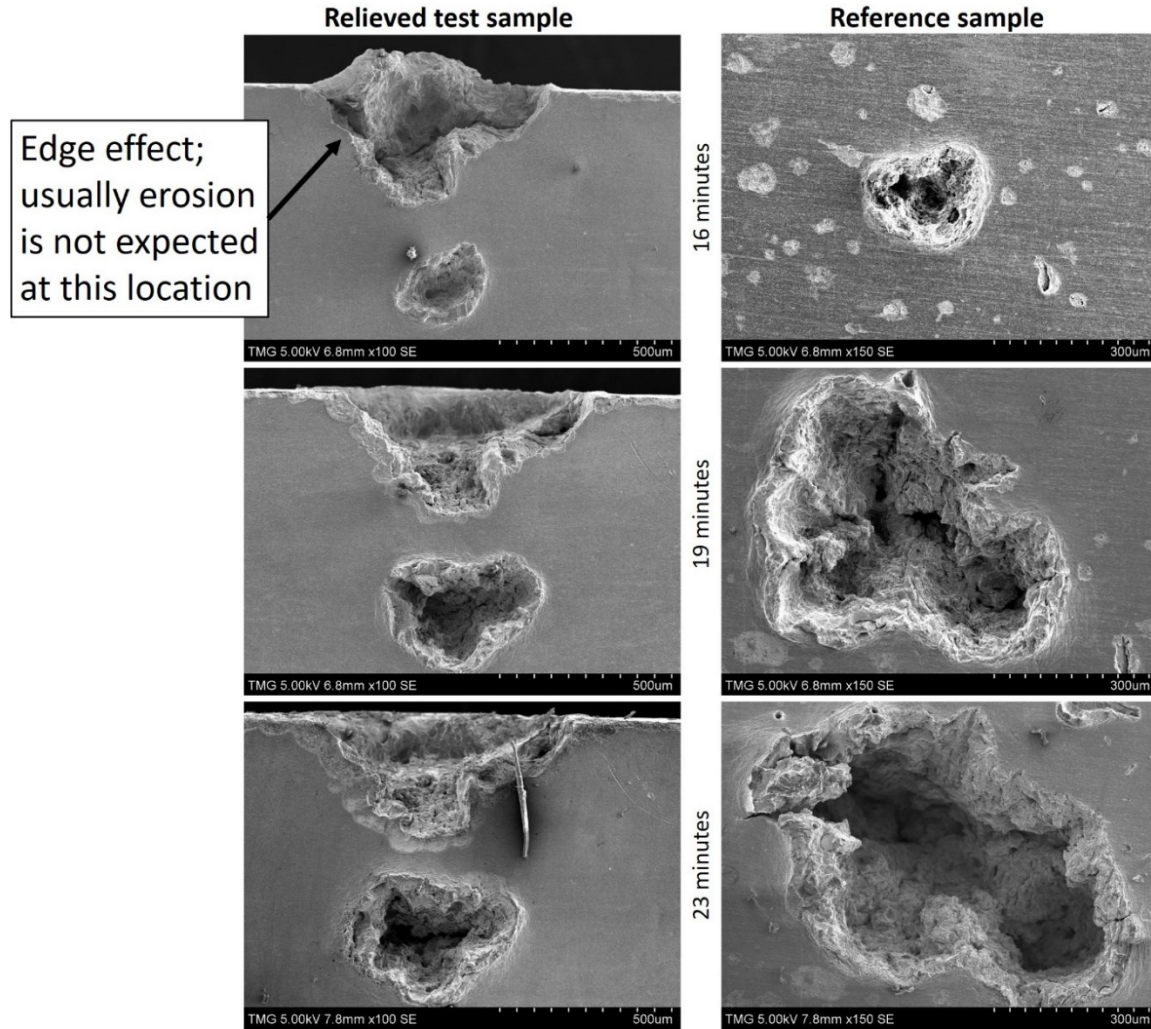


Figure 4.50 Pit growth comparison during SR-2 test.

A major difference observed is that the pits in the reference sample grow by means of breaking away of relatively large chunks as seen in Figure 4.51. This type of growth was not observed in the relieved samples. The chunks are formed when the existing pit grows by means of intergranular fracture associated with hydraulic penetration [41], [51]. When the area around a chunk is eroded away, the subsequent droplet impacts, deform and strain the base of the chunk. This ultimately removes the chunk by means of fracture when it is sufficiently weak. The accumulated strain in the reference sample aids the formation of cracks and facilitates such failure. As most of the accumulated strain is constantly being removed in the relieved test

sample, the probability of formation of chunks and their fracture is greatly reduced and the material deforms instead.

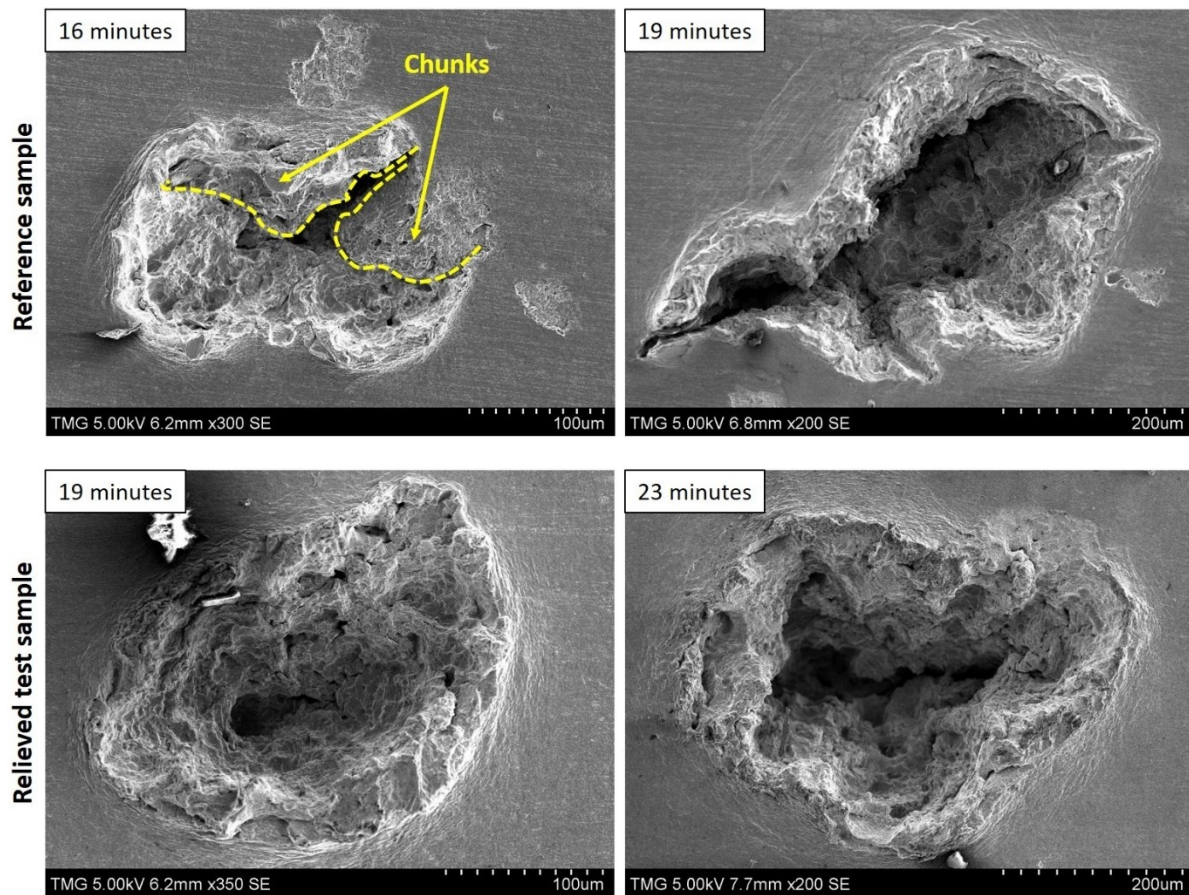


Figure 4.51 Difference in growth mechanism in samples of SR-2 test.

Some instances of severe plastic deformation were observed over the fractured surface in the interiors of pits of the relieved test sample of the SR-2 test, as shown in Figure 4.52. Such severe deformation was unique to the relieved test sample and was not found in the reference sample. The absence of accumulated strain and the lowered strength of the relieved test sample cause the material to deform instead of breaking away as chunks by large fractures. The test sample can absorb more impact energy as some of the strain is removed by stress relieving and a part of impact energy is expended on strain hardening. The material is more susceptible to deformation in the absence of accumulated strain and hence the signs of

severe deformation were only observed in the relieved test sample. The impact energy expended on plastic deformation is more in the relieved test sample than in the reference. On the other hand, the impact energy is expended on further strain hardening and fracturing in the reference sample. The strain being accumulated in the reference sample resists further addition of strain while also aiding in the faster removal of material by forming cracks. Therefore, the relieved test sample erodes at a slower rate than the reference as observed in the erosion curves of SR-2 (Figure 4.48).

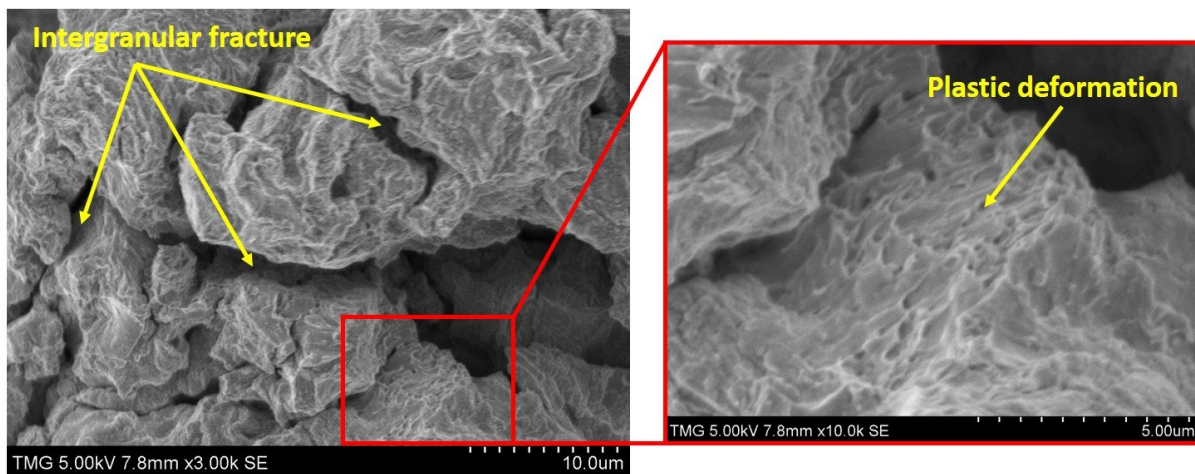


Figure 4.52 Severe plastic deformation on fractured surface in the relieved test sample of SR-2 test.

The mechanism of deceleration in the erosion of the relieved test sample can be summarized through a schematic in Figure 4.53. As the material is exposed to droplet impacts, the strain is developed within the material in the form of dislocations and a few permanent defects such as microcracks or micro-voids (a). As the exposure is stopped and the material is subjected to a strain relieving treatment, most of the strain is relieved but some of the dislocations and microcracks remain (b). When the stress relieved sample is exposed to erosion again, additional dislocations and permanent defects are created (c). With the continuation of erosion and stress relieving cycles, the residual strain and microcracks keep growing until

fracture (d, e, f). With the increase in frequency of relieving during a WDE test, more strain can be removed before it creates permanent defects or fracture. Assuming the material requires a minimum number of defects to fail under such WDE environment, it can therefore take additional droplet impacts before failure. This demonstrates that the strain in the metal is a contributor of acceleration in erosion and its removal can help decelerate WDE.

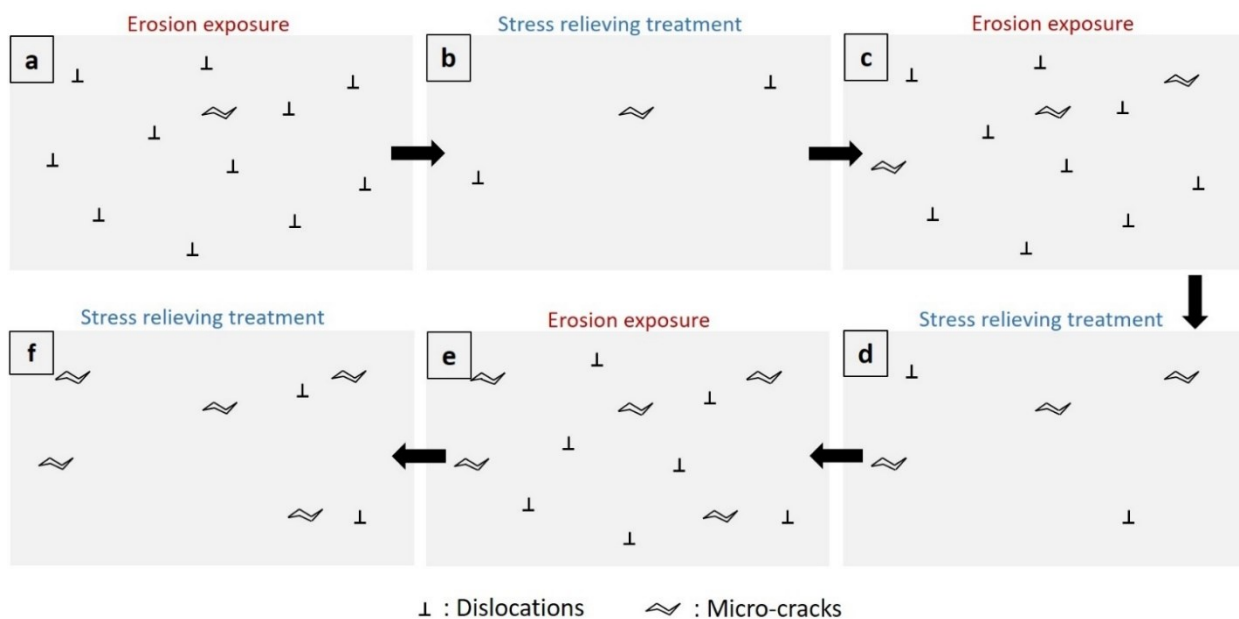


Figure 4.53 Schematic of intermittent stress relieving in the relieved test sample during erosion test.

It can be concluded that the repeated stress relieving process lowered the erosion incubation time by virtue of lowered strength. The early start of erosion in the relieved sample of the SR-2 test is due to a combination of the edge effect and the loss of additional strength expected from strain hardening through stress relieving. As the erosion starts, the lower frequency of stress relieving failed to influence the erosion rate. Larger frequency of stress relieving decelerates the erosion and hence the accumulated strain is believed to be contributing to the acceleration of erosion.

5. Conclusions, contributions and suggestions for future work

5.1. Conclusions

The purpose of this study is to investigate the role of strain hardening on WDE resistance. 17-4 PH stainless steel, which can have various strain hardening exponents and tensile properties by means of aging, is used to obtain three conditions with three set of properties. Each condition is WDE tested with and without the deep rolling (DR) surface treatment and the synergy of strain hardening exponent, yield strength and elastic resilience in resisting erosion is analyzed. Also, the strain accumulated from droplet impacts is relieved intermittently and its role in WDE is analyzed using X22CrMoV12-1 stainless steel. The conclusions made from this research are as follows:

1. Condition-A, H925 and H1025 had relatively low, high and moderate strength but their incubation times were not proportional to their strengths. At 250 and 300m/s impact speeds, Condition-A and H1025 had a relatively low incubation time and the H925 had a relatively high incubation time. Greater strength, elastic resilience and n-value contribute to the elongation of the incubation period. Condition-A and H1025 have similar incubation times. This was due to the combined effect of Condition-A having a lower yield strength and a greater n-value compared to H1025 having a greater yield strength but lower n-value. With a relatively greater strength and moderate n-value, H925 has a superior incubation time among the three.
2. With the addition of beneficial compressive residual stresses (CRS) and the initial strain from the DR surface treatment, the erosion incubation behavior remained similar to that seen in the samples without the surface treatment. The initial strain added from DR and

the beneficial CRS help resist the erosion depending on their strength, elastic resilience and n-value. Condition-A and H1025 have similar incubation times. Again, this was due to the combined effect of Condition-A having a lower yield strength and a greater n-value compared to H1025 having a greater yield strength but lower n-value.

3. The DR surface treatment slightly increased the incubation time and slightly increased the maximum erosion rate in each condition. This makes the overall erosion performance in samples with DR treatment similar to that without DR treatment in each condition.
4. The accumulated strain removal at lower frequency (SR-1 test) saw a reduction in incubation time but no change in the erosion rate was observed. With the higher frequency (SR-2 test) of strain removal, both the incubation time and the erosion rate were reduced. The lowered incubation time with strain relieving is attributed to lowered strength and loss of resistance from strain hardening. The strain relieving decelerates erosion by allowing deformation of the material and by creating room for additional impacts to build up the lost strain.

5.2. Contributions

This work contributes to the understanding of role of strain hardening in WDE. Strain hardening in addition to yield strength and elastic resilience are found to be contributing to the erosion resistance during the incubation stage. It was observed that the material with lower yield strength and greater strain hardening exponent can yield similar erosion incubation as the material with greater yield strength and lower strain hardening exponent. The combination of greater both yield strength and strain hardening exponent is found to be the most qualified for resisting erosion. The role of yield strength and strain hardening exponent in resisting erosion is the same even with the DR treatment which is known to induce strain and beneficial

Compressive Residual Stresses (CRS). The erosion mechanism is found to be the same even as the mechanical properties were varied from aging heat treatments.

It was found that the frequency of intermittent stress relieving has an effect on erosion behavior. Frequent stress relieving during the erosion test improves the erosion resistance during maximum erosion stage but decreases the incubation time owing to the reduction in strength.

5.3. Suggestions for future work

1. Materials or their heat-treated conditions which have similar yield strength and elastic modulus but different strain hardening exponents have to be tested for WDE. This can help in the clearer understanding of the influence of strain hardening on erosion incubation.
2. Testing of materials with high strain hardening exponent for stress relieving is suggested as this allows for reduction in frequency of relieving, which minimizes the reduction in strength. This will help in better understanding the role of accumulated strain with minimum effect of reduced strength.
3. To avoid the edge effect on the WDE behavior, a chamfer should be machined at the edges of the coupon in the future tests.
4. Combination of ultra-smooth surface finish and stress relief is suggested. This is expected to delay pits formation and reveal the effect of stress relief more clearly.

6. References

- [1] Y. S. H. Najjar, “Enhancement of performance of gas turbine engines by inlet air cooling and cogeneration system,” *Appl. Therm. Eng.*, vol. 16, no. 2, pp. 163–173, 1996.
- [2] A. M. Al-Ibrahim and A. Varnham, “A review of inlet air-cooling technologies for enhancing the performance of combustion turbines in Saudi Arabia,” *Appl. Therm. Eng.*, vol. 30, no. 14–15, pp. 1879–1888, 2010.
- [3] “<https://www.power-technology.com/contractors/powerplantequip/meeindustries/>.” as on 22nd March 2021.
- [4] F. J. Heymann, “Liquid Impingement Erosion,” in *ASM Handbook Volume-18. Friction, lubrication and wear technology*, ASM International, 1992, pp. 408–429.
- [5] M. Ahmad, “Experimental assessment of droplet impact erosion of low pressure steam turbine blades,” University of Stuttgart, Stuttgart, 2009.
- [6] J. R. Khan, “Fog cooling, wet compression and droplet dynamics in gas turbine compressors,” University of New Orleans, 2009.
- [7] A. Fyall, “Practical aspects of rain erosion of aircraft and missiles,” *Philos. Trans. R. Soc. London . Ser. A , Math. Phys. Sci.*, vol. 260, no. 1110, pp. 161–167, 1966.
- [8] O. Gohardani, “Impact of erosion testing aspects on current and future flight conditions,” *Prog. Aerosp. Sci.*, vol. 47, no. 4, pp. 280–303, 2011.
- [9] M. Ahmad, M. Casey, and N. Sürken, “Experimental assessment of droplet impact erosion resistance of steam turbine blade materials,” *Wear*, vol. 267, no. 9–10, pp. 1605–1618, 2009.

- [10] F. J. Heymann, “Survey of clues to the relationship between erosion rate and Impact conditions,” in *Proceedings of the second Meersburg conference on rain erosion and allied phenomena*, 1967, pp. 683–760.
- [11] H. S. Kirols, D. Kevorkov, A. Uihlein, and M. Medraj, “Water droplet erosion of stainless steel steam turbine blades,” *Mater. Res. Express*, vol. 4, no. 8, 2017.
- [12] W. D. Pouchat *et al.*, “Basic Investigation of turbine erosion phenomena. NASA CR-1830,” 1971.
- [13] B. E. Lee, K. J. Riu, S. H. Shin, and S. B. Kwon, “Development of a water droplet erosion model for large steam turbine blades,” *KSME Int. J.*, vol. 17, no. 1, pp. 114–121, 2003.
- [14] F. P. Bowden and J. H. Brunton, “The deformation of solids by liquid impact at supersonic speeds,” *Proc. R. Soc. London. A Math. Phys. Sci.*, vol. 263, no. 1315, pp. 433–450, 1961.
- [15] G. F. Schmitt, “Liquid and Solid Particle Erosion. Technical Report AFML- TR-79-4122,” 1979.
- [16] A. A. Fyall, R. B. King, and R. N. C. Strain, “Rain Erosion Aspects of Aircraft and Guided Missiles,” *Aeronaut. J.*, vol. 66, no. 619, pp. 447–453, 1962.
- [17] N. Dalili, A. Edrisy, and R. Carriveau, “A review of surface engineering issues critical to wind turbine performance,” *Renew. Sustain. Energy Rev.*, vol. 13, no. 2, pp. 428–438, 2009.
- [18] M. H. Keegan, D. H. Nash, and M. M. Stack, “On erosion issues associated with the leading edge of wind turbine blades,” *J. Phys. D. Appl. Phys.*, vol. 46, no. 38, 2013.
- [19] R. Herring, K. Dyer, F. Martin, and C. Ward, “The increasing importance of leading edge

erosion and a review of existing protection solutions," *Renew. Sustain. Energy Rev.*, vol. 115, no. September, 2019.

- [20] A. Sareem, C. A. Sapre, and M. S. Selig, "Effects of leading edge erosion on wind turbine blade performance," *Wind Energy*, vol. 17, no. 10, pp. 1531–1542, 2014.
- [21] J. F. Ripken, "Comparative Studies of Drop Impingement Erosion and Cavitation Erosion," 1969.
- [22] S. Hattori and M. Takinami, "Comparison of cavitation erosion rate with liquid impingement erosion rate," *Wear*, vol. 269, no. 3–4, pp. 310–316, 2010.
- [23] B. S. Mann, V. Arya, and B. K. Pant, "Cavitation erosion behavior of HPDL-treated TWAS-coated Ti6Al4V alloy and its similarity with water droplet erosion," *J. Mater. Eng. Perform.*, vol. 21, no. 6, pp. 849–853, 2012.
- [24] *ASTM G40-15: Standard terminology relating to erosion and wear*, 2015th ed. West Conshohocken, PA, USA: ASTM International.
- [25] *ASTM G73-04: Standard Practice for Liquid Impingement Erosion Testing*. West Conshohocken, PA, USA: ASTM International, 2004.
- [26] F. J. Heymann, "High-Speed liquid impact between a liquid drop and solid surface," *J. Appl. Phys.*, vol. 40, no. 13, pp. 5113–5122, 1969.
- [27] M. B. Lesser, "Analytic Solutions of Liquid-Drop Impact Problems," *Proc. R. Soc. A Math. Phys. Eng. Sci.*, vol. 377, no. 1770, pp. 289–308, 1981.
- [28] N. L. Hancox and J. H. Brunton, "The erosion of solids by the repeated impact of liquid drops," *Philos. Trans. R. Soc. London. Ser. A, Math. Phys. Sci.*, vol. 260, no. 1110, pp. 121–139, 1966.

- [29] F. P. Bowden and J. E. Field, “The Brittle Fracture of Solids by Liquid Impact, by Solid Impact, and by Shock,” *Proc. R. Soc. London . Ser. A , Math. Phys. Sci.*, vol. 282, no. 1390, pp. 331–352, 1964.
- [30] J. E. Field, M. B. Lesser, and J. P. Dear, “Studies of Two-Dimensional Liquid-Wedge Impact and Their Relevance to Liquid-Drop,” *Proc. R. Soc. A Math. Phys. Eng. Sci.*, vol. 401, no. 1821, pp. 225–249, 1985.
- [31] S. C. Cook, “Erosion by Water-Hammer,” *Proc. R. Soc. London. Ser. A, Contain. Pap. a Math. Phys. Character*, vol. 119, no. 783, pp. 481–488, 1928.
- [32] O. G. Engel, “Waterdrop collisions with solid surfaces,” *J. Res. Natl. Bur. Stand. (1934)*., vol. 54, no. 5, pp. 281–298, 1955.
- [33] M. Rosenblatt, Y. M. Ito, and G. E. Eggum, “Analysis of brittle target fracture from a subsonic water drop impact,” in *Erosion: prevention and useful applications. ASTM STP-664*, W. F. Adler, Ed. Vail, CO, USA: ASTM, 1979, pp. 227–254.
- [34] W. F. Adler, “Mechanics of liquid impact,” in *Treatise on materials science and technology, Volume-16*, C. M. Preece, Ed. New: Academic Press, Inc., 1979, pp. 127–183.
- [35] J. H. Brunton and M. C. Rochester, “Erosion of solid surfaces by the impact of liquid drops,” in *Treatise on materials science and technology, Volume-16*, C. M. Preece, Ed. New York: Academic Press, Inc., 1979, pp. 185–248.
- [36] J. E. Field, “ELSI conference: invited lecture. Liquid impact: theory, experiment, applications,” *Wear*, vol. 233–235, pp. 1–12, 1999.
- [37] D. C. Jenkins and J. D. Booker, “The impingement of water drops on a surface moving at high speed,” in *Aerodynamic Capture of Particles. Proceedings of a Conference Held at*

British Coal Utilization Research Association, Leatherhead, U.K., 1960, pp. 97–103.

- [38] A. A. Fyall, “Single impact studies with liquid and solids,” in *Proceedings of the Second Meersburg Conference on Rain Erosion and Allied Phenomena*, 1967, pp. 563–592.
- [39] G. P. Thomas and J. H. Brunton, “Drop Impingement erosion of metals,” *Proc. R. Soc. London . Ser. A, Math. Phys. Sci.*, vol. 314, no. 1519, pp. 549–565, 1970.
- [40] A. K. Gujba, “Influence of Mechanical Surface Treatments on the Water Droplet Erosion Performance of Ti-6Al-4V,” Concordia University, Montreal, 2016.
- [41] D. Ma, A. Mostafa, D. Kevorkov, P. Jedrzejowski, M. Pugh, and M. Medraj, “Water Impingement Erosion of Deep-Rolled Ti64,” *Metals (Basel).*, vol. 5, no. 4, pp. 1462–1486, 2015.
- [42] N. Kamkar, “Water droplet erosion mechanisms of Ti-6Al-4V,” École de Technologie Supérieure (ÉTS), Montreal, Canada, 2014.
- [43] H. Rieger, “The damage to metal on high speed impact with water drops,” in *Proceedings of the rain erosion conference*, 1965, pp. 107–113.
- [44] F. G. Hammitt and F. J. Heymann, “Liquid erosion failures,” in *ASM Handbook, Volume-11*, 1986, pp. 163–171.
- [45] F. J. Heymann, “Erosion by liquids,” *Mach. Des.*, vol. 10, pp. 118–124, 1970.
- [46] H. S. Kirols, D. Kevorkov, A. Uihlein, and M. Medraj, “The effect of initial surface roughness on water droplet erosion behaviour,” *Wear*, vol. 342–343, pp. 198–209, 2015.
- [47] K. Range and F. Feuillebois, “Influence of surface roughness on liquid drop impact,” *J. Colloid Interface Sci.*, vol. 203, no. 1, pp. 16–30, 1998.

- [48] M. S. Mahdipoor, D. Kevorkov, P. Jedrzejowski, and M. Medraj, “Water droplet erosion behaviour of gas nitrided Ti6Al4V,” *Surf. Coatings Technol.*, vol. 292, pp. 78–89, 2016.
- [49] M. S. Mahdipoor, D. Kevorkov, P. Jedrzejowski, and M. Medraj, “Water droplet erosion mechanism of nearly fully-lamellar gamma TiAl alloy,” *Mater. Des.*, vol. 89, pp. 1095–1106, 2016.
- [50] A. K. Gujba, L. Hackel, D. Kevorkov, and M. Medraj, “Water droplet erosion behaviour of Ti-6Al-4V and mechanisms of material damage at the early and advanced stages,” *Wear*, vol. 358–359, pp. 109–122, 2016.
- [51] D. Ma, T. J. Harvey, R. G. Wellman, and R. J. Wood, “Characterisation of rain erosion at ex-service turbofan blade leading edges,” *Wear*, vol. 426–427, no. December 2018, pp. 539–551, 2019.
- [52] J. M. Robinson and R. C. Reed, “Water droplet erosion of laser surface treated Ti6A14V,” *Wear*, vol. 186–187, no. PART 2, pp. 360–367, 1995.
- [53] N. Kamkar, F. Bridier, P. Bocher, and P. Jedrzejowski, “Water droplet erosion mechanisms in rolled Ti-6Al-4V,” *Wear*, vol. 301, no. 1–2, pp. 442–448, 2013.
- [54] N. Fujisawa, S. Takano, K. Fujisawa, and T. Yamagata, “Experiments on liquid droplet impingement erosion on a rough surface,” *Wear*, vol. 398–399, no. 2, pp. 158–164, 2018.
- [55] A. K. Gujba, Z. Ren, Y. Dong, C. Ye, and M. Medraj, “Effect of ultrasonic nanocrystalline surface modification on the water droplet erosion performance of Ti-6Al-4V,” *Surf. Coatings Technol.*, vol. 307, pp. 157–170, 2016.
- [56] A. K. Gujba, L. Hackel, and M. Medraj, “Water Droplet Erosion Performance of Laser Shock Peened Ti-6Al-4V,” *Metals (Basel)*., vol. 6, no. 11, p. 262, 2016.

- [57] G. Hoff, G. Langbein, and H. Rieger, “Material destruction due to liquid impact,” in *Erosion by cavitation and impingement. ASTM STP-408*, Atlantic City, NJ, USA: ASTM, 1967, pp. 42–69.
- [58] M. S. Mahdipoor, H. S. Kirols, D. Kevorkov, P. Jedrzejowski, and M. Medraj, “Influence of impact speed on water droplet erosion of TiAl compared with Ti6Al4V,” *Sci. Rep.*, vol. 5, pp. 1–17, 2015.
- [59] L. I. Seleznev, V. A. Ryzhenkov, and A. F. Mednikov, “Phenomenology of erosion wear of constructional steels and alloys by liquid particles,” *Therm. Eng.*, vol. 57, no. 9, pp. 741–745, 2010.
- [60] S. Van Der Zwaag and J. E. Field, “Rain erosion damage in brittle materials,” *Eng. Fract. Mech.*, vol. 17, no. 4, pp. 367–379, 1983.
- [61] F. J. Heymann, “On the shock wave velocity and impact pressure in high-speed liquid-solid impact,” *J. Basic Eng.*, vol. 90, no. 3, pp. 400–402, 1968.
- [62] J. E. Field, “The physics of liquid impact, shock wave interactions with cavities, and the implications to shock wave lithotripsy,” *Phys. Med. Biol.*, vol. 36, no. 11, pp. 1475–1484, 1991.
- [63] H. S. Kirols, M. S. Mahdipoor, D. Kevorkov, A. Uihlein, and M. Medraj, “Energy based approach for understanding water droplet erosion,” *Mater. Des.*, vol. 104, pp. 76–86, 2016.
- [64] M. Ahmad, M. Schatz, and M. V. Casey, “Experimental investigation of droplet size influence on low pressure steam turbine blade erosion,” *Wear*, vol. 303, no. 1–2, pp. 83–86, 2013.

- [65] M. B. Lesser and J. E. Field, “The Impact of Compressible Liquids,” *Annu. Rev. Fluid Mech.*, vol. 15, no. 1, pp. 97–122, 1983.
- [66] A. O’Carroll, M. Hardiman, E. F. Tobin, and T. M. Young, “Correlation of the rain erosion performance of polymers to mechanical and surface properties measured using nanoindentation,” *Wear*, vol. 412–413, no. July, pp. 38–48, 2018.
- [67] D. W. C. Baker, K. H. Jolliffe, and D. Pearson, “The Resistance of Materials to Impact Erosion DamageSource,” *Philos. Trans. R. Soc. London*, vol. 260, no. 1110, pp. 193–203, 1966.
- [68] N. Fujisawa *et al.*, “The influence of material hardness on liquid droplet impingement erosion,” *Nucl. Eng. Des.*, vol. 288, pp. 27–34, 2015.
- [69] B. Luiset, F. Sanchette, A. Billard, and D. Schuster, “Mechanisms of stainless steels erosion by water droplets,” *Wear*, vol. 303, no. 1–2, pp. 459–464, 2013.
- [70] F. J. Heymann, “Towards quantitative prediction of liquid impact erosion,” in *Characterization and determination of erosion resistance. ASTM STP-474.*, Atlantic City, NJ, USA: ASTM, 1970, pp. 212–248.
- [71] M. Ahmad, M. Schatz, and M. V. Casey, “An empirical approach to predict droplet impact erosion in low-pressure stages of steam turbines,” *Wear*, vol. 402–403, pp. 57–63, 2018.
- [72] W. Herbert, “Influence of heat treatment upon rain erosion of steels,” in *Proceedings of the rain erosion conference*, 1965, pp. 114–119.
- [73] “<https://www.ecoroll.de/en/processes/deep-rolling.html>.”
- [74] P. S. Prevéy and J. Cammett, “Low cost corrosion damage mitigation and improved

fatigue performance of low plasticity burnished 7075-T6,” *J. Mater. Eng. Perform.*, vol. 10, no. 5, pp. 548–555, 2001.

- [75] N. Lyubenova *et al.*, “Impact of the Process Parameters, the Measurement Conditions and the Pre-Machining on the Residual Stress State of Deep Rolled Specimens,” *J. Manuf. Mater. Process.*, vol. 3, no. 3, p. 56, 2019.
- [76] I. Altenberger, “Deep rolling - The past, the present and the future,” in *Proceedings of the 9th International Conference on Shot Peening*, 2005, no. April, pp. 144–155.
- [77] I. Nikitin and B. Scholtes, “Deep rolling of austenitic steel AISI 304 at different temperatures – near surface microstructures and fatigue,” *HTM J. Heat Treat. Mater.*, vol. 67, no. 3, pp. 188–194, 2012.
- [78] I. Nikitin, B. Scholtes, H. J. Maier, and I. Altenberger, “High temperature fatigue behavior and residual stress stability of laser-shock peened and deep rolled austenitic steel AISI 304,” *Scr. Mater.*, vol. 50, no. 10, pp. 1345–1350, 2004.
- [79] I. Altenberger, E. A. Stach, G. Liu, R. K. Nalla, and R. O. Ritchie, “An in situ transmission electron microscope study of the thermal stability of near-surface microstructures induced by deep rolling and laser-shock peening,” *Scr. Mater.*, vol. 48, no. 12, pp. 1593–1598, 2003.
- [80] P. Delgado, I. I. Cuesta, J. M. Alegre, and A. Díaz, “State of the art of Deep Rolling,” *Precis. Eng.*, vol. 46, pp. 1–10, 2016.
- [81] D. Ma, “Liquid Impingement Erosion Performance of Deep Rolled Ti6Al4V,” pp. 1–125, 2014.
- [82] T. Zhang, “The effects of ball burnishing for aerospace blade material 17-4 PH steel,”

University of Toledo, 2013.

- [83] A. M. Abrão, B. Denkena, J. Köhler, B. Breidenstein, and T. Mörke, “The influence of deep rolling on the surface integrity of AISI 1060 high carbon steel,” *Procedia CIRP*, vol. 13, pp. 31–36, 2014.
- [84] P. Prabhu, S. Kulkarni, and S. Sharma, “Influence of deep cold rolling and low plasticity burnishing on surface hardness and surface roughness of AISI 4140 steel,” *Int. J. Mech. Mechatronics Eng.*, vol. 4, no. 12, pp. 1420–1425, 2010.
- [85] J. Datsko, *Material properties and manufacturing processes*. John Wiley & Sons Inc., 1966.
- [86] J. Datsko, *Materials selection for design and manufacturing: Theory and Practice*. Marcel Dekker Inc., 1997.
- [87] D. K. Benson and J. R. Hancock, “Effect of Strain Rate on the Cyclic Response of Metals.,” *Metall. Trans.*, vol. 5, no. 8, pp. 1711–1715, 1974.
- [88] H. J. Rack and D. Kalish, “Strength, Fracture Toughness, and Low Cycle Fatigue Behavior of 17-4 Ph Stainless Steel.,” *Metall. Trans.*, vol. 5, no. 7, pp. 1595–1605, 1974.
- [89] BrushWellman, “BrushWellman Connector engineering design guide.”
- [90] M. Gedeon, “Issue 51 - Strain Hardening and Formability,” 2013.
- [91] W. F. Hosford and R. M. Caddell, *Metal forming mechanics and metallurgy*. Cambridge University Press, 2007.
- [92] J. R. Davis, Ed., *ASM specialty handbook: heat-resistant materials*. ASM International, 1997.

- [93] F. K. Bloom, “Stress Corrosion Cracking of hardenable stainless steels,” *Corrosion*, vol. 11, no. 8, pp. 39–49, 1955.
- [94] H. Mirzadeh, A. Najafizadeh, and M. Moazeny, “Flow curve analysis of 17-4 PH stainless steel under hot compression test,” *Metall. Mater. Trans. A Phys. Metall. Mater. Sci.*, vol. 40, no. 12, pp. 2950–2958, 2009.
- [95] *ASTM A693-06: Standard Specification for Precipitation-Hardening Stainless and Heat-Resisting Steel Plate, Sheet, and Strip*, 2006th ed. West Conshohocken, PA, USA: ASTM International, 2006.
- [96] C. N. Hsiao, C. S. Chiou, and J. R. Yang, “Aging reactions in a 17-4 PH stainless steel,” *Mater. Chem. Phys.*, vol. 74, no. 2, pp. 134–142, 2002.
- [97] G. Yeli, M. A. Auger, K. Wilford, G. D. W. Smith, P. A. J. Bagot, and M. P. Moody, “Sequential nucleation of phases in a 17-4PH steel : Microstructural characterisation and mechanical properties,” *Acta Mater.*, vol. 125, pp. 38–49, 2017.
- [98] U. K. Viswanathan, S. Banerjee, and R. Krishnan, “Effects of aging on the microstructure of 17-4 PH stainless steel,” *Mater. Sci. Eng.*, vol. 104, no. C, pp. 181–189, 1988.
- [99] U. K. Viswanathan, P. K. K. Nayar, and R. Krishnan, “Kinetics of precipitation in 17–4 PH stainless steel,” *Mater. Sci. Technol.*, vol. 5, no. 4, pp. 346–349, 1989.
- [100] M. Murayama, Y. Katayama, and K. Hono, “Microstructural evolution in a 17-4 PH stainless steel after aging at 400 °C,” *Metall. Mater. Trans. A Phys. Metall. Mater. Sci.*, vol. 30, no. 2, pp. 345–353, 1999.
- [101] H. Mirzadeh and A. Najafizadeh, “Aging kinetics of 17-4 PH stainless steel,” *Mater. Chem. Phys.*, vol. 116, no. 1, pp. 119–124, 2009.

- [102] F. W. Comeli, S. Rocha, C. Augusto, S. De Oliveira, G. Lemos, and R. D. M. Castro, “Effects of Tempering Temperature on the Microstructure and Creep Resistance of X22CrMoV12-1 Steel Used on Steam Turbine Blades,” *Am. J. Mater. Sci.*, vol. 8, no. 4, pp. 65–72, 2018.
- [103] R. Manojkumar, S. Mahadevan, C. K. Mukhopadhyay, and B. P. C. Rao, “Aging behavior of 17-4 PH stainless steel studied using XRDLPA for separating the influence of precipitation and dislocations on microstrain,” *J. Mater. Res.*, vol. 32, no. 22, pp. 4263–4271, 2017.
- [104] *European standard DIN 10269: Steels and nickel alloys for fasteners with specified elevated and/or low temperature properties*, 1999th ed. Berlin: Deutsches Institut für Normung, 1999.
- [105] *ASTM E8/E8M: Standard test methods for tension testing of metallic materials*, 2013th ed. West Conshohocken, PA, USA: ASTM International, 2013.
- [106] R. G. Perel'man and N. A. Freishist, “Study of stress during exposure to high-speed droplet impact,” in *Problemy Prochnosti*, 1979, no. 5, pp. 50–55.
- [107] P. Prevéy, N. Jayaraman, and J. Cammett, “Overview of Low Plasticity Burnishing for Mitigation of Fatigue Damage Mechanisms,” *Fatigue Fract. Steels*, vol. 9, no. 513, pp. 1–6, 2005.
- [108] W. F. Adler and S. V. Hooker, “Rain erosion mechanisms in brittle materials,” *Wear*, vol. 50, pp. 11–38, 1978.
- [109] B. Bay and N. Hansen, “Initial stages of recrystallization in aluminum of commercial purity,” *Metall. Trans. A*, vol. 10, no. 3, pp. 279–288, 1979.

Appendix A

During the micrographic examination of erosion craters, an interesting phenomenon has been observed in the vicinity of expanding erosion craters. Circular holes have sometimes been observed in the uneroded surface very close to a crater or pit as seen in Figure A.1 and Figure A.2. These ‘spouting holes’ are formed often right beside the deeper and laterally expanding section of the crater as seen in the picture.

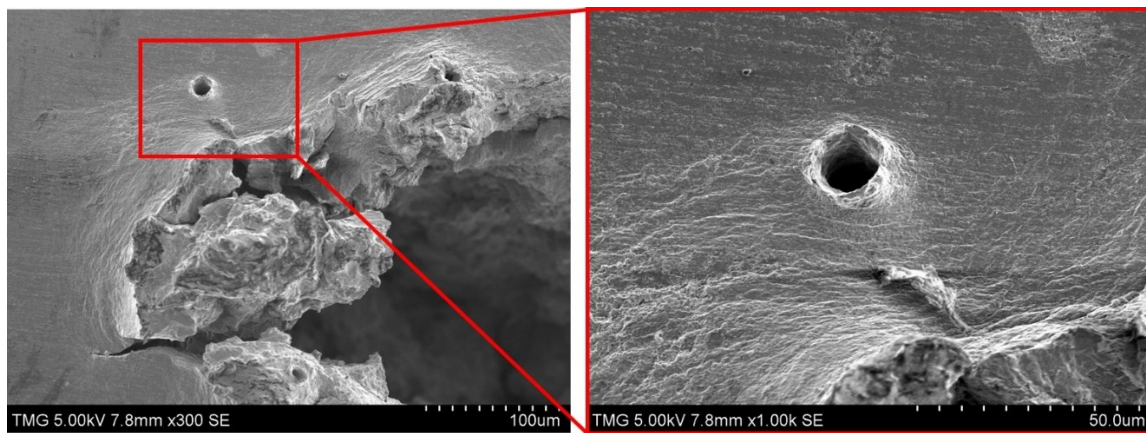


Figure A.1 Spouting hole in polished X22CrMoV12-1 stainless steel sample.

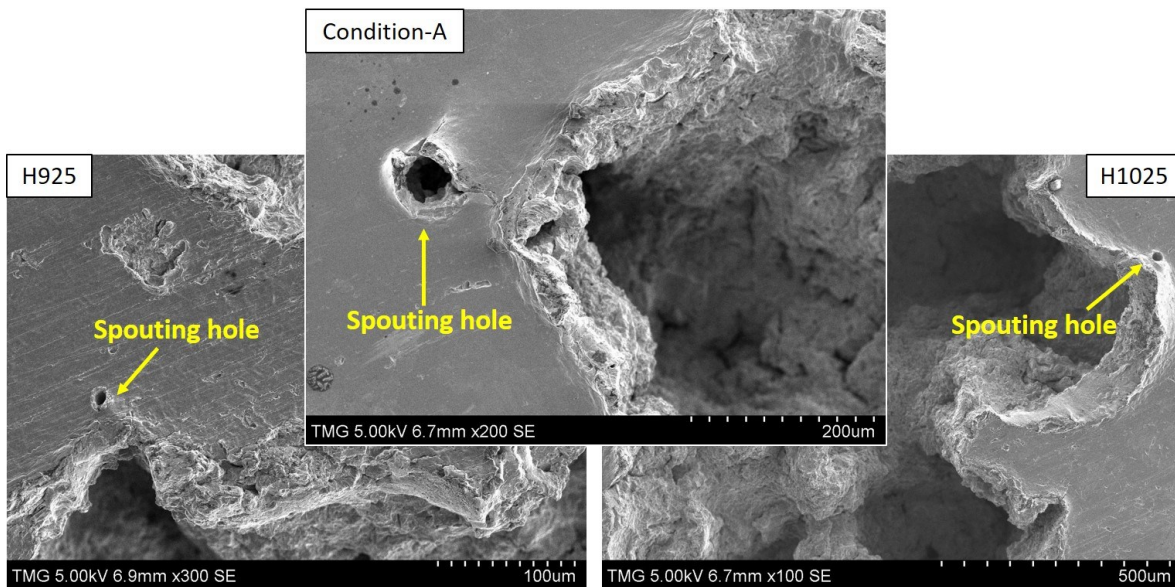


Figure A.2 Spouting holes in deep rolled 17-4 PH stainless steel samples.

The periphery of these ‘spouting holes’ are deformed and resembles the opening of a volcano. The hollowed part beneath the surface through crater expansion and their appearance indicate that these holes are formed by liquid gushing out with great force. The different sizes of these ‘spouting holes’ suggests that they could have expanded under similar conditions created during subsequent droplet strikes. Figure A.3 shows a schematic of the formation of a spouting hole beside an existing erosion crater. The laterally expanding crater beneath the surface creates pockets (a) which expand by tunneling from hydraulic penetration (b) and (c). The close proximity of these pockets to the surface makes it possible for the expanding liquid from a nearby droplet impacts to eject out when the tunneling is very close to the surface (d). A ‘spouting hole’ is hence created and grows with subsequent impacts until it is absorbed into the growing crater. This phenomenon was observed in both the DR treated and polished samples, suggesting it was independent of the surface preparation.

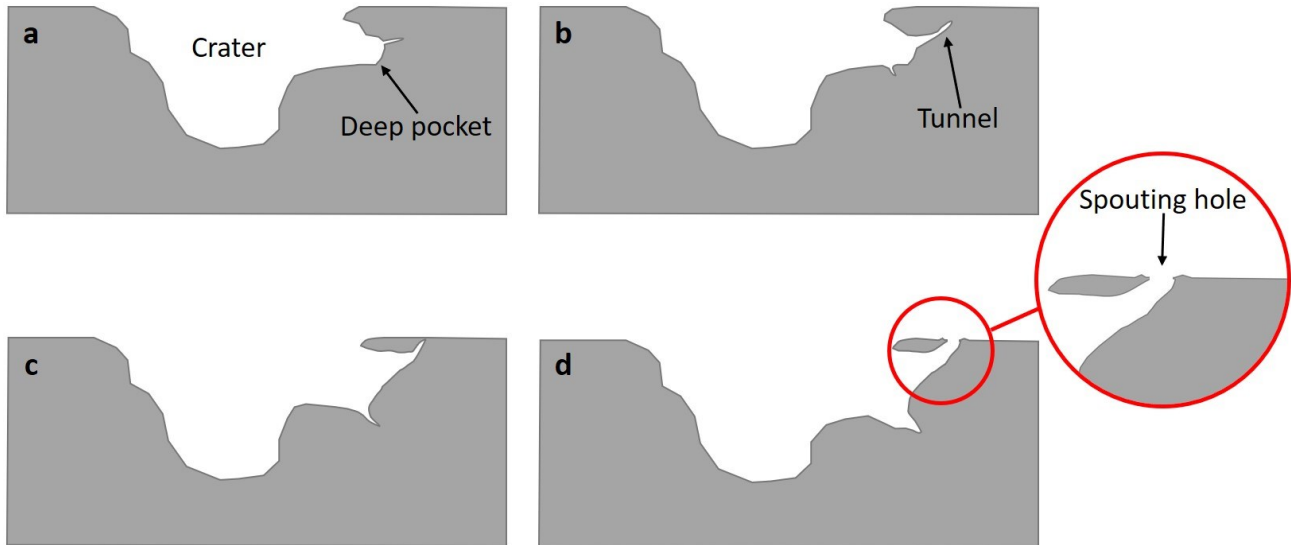


Figure A.3 Schematic showing the formation of a spouting hole by an erosion crater.